

学位論文

Classical Ocean General Circulation Theory

Revisited Using Layer Models

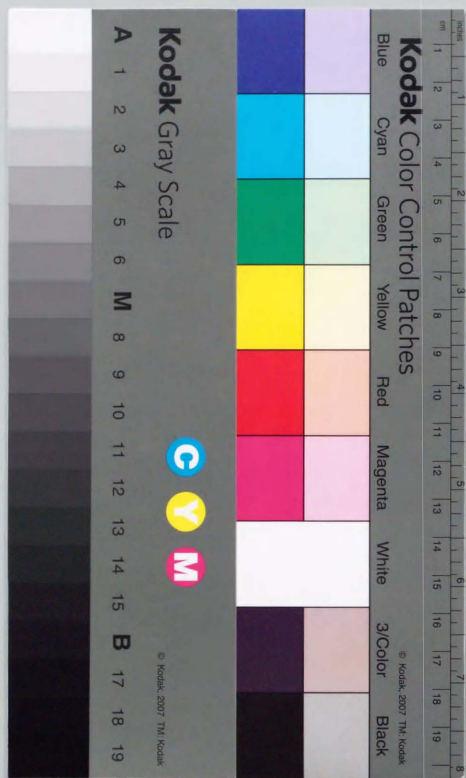
古典海洋大循環論の層モデルを用いた再考察

平成10年12月第士(理学)卒業

東京大学大学院理学系研究科

地球惑星物理学専攻

阪本 敬 浩



①

学位論文

Classical Ocean General Circulation Theory  
Revisited Using Layer Models

古典海洋大循環論の層モデルを用いた再考察

平成 10 年 12 月博士 (理学) 申請

東京大学大学院理学系研究科  
地球惑星物理学専攻

阪本 敏浩

## Contents

### Summary

v

### PART I DISCONTINUOUS SOLUTIONS OF TWO-LAYER PLANETARY GEOSTROPHIC EQUATIONS

<b>1</b>	<b>Discontinuities in the Sverdrup interior</b>	<b>3</b>
1.1	Introduction	3
1.2	The two-layer model	6
1.2.1	The integral conservation law of momentum and associated jump conditions	6
1.2.2	An alternative expression for the system of the two-layer equations	8
1.3	The reduced gravity model	9
1.3.1	Hyperbolic perspective of Parsons' model	9
1.3.2	Effect of small friction	13
1.3.3	Effect of density mixing	13
1.4	Illustrative examples	15
1.4.1	Finite-depth effect on Parsons' model	15
1.4.2	Closed geostrophic contour associated with the Rhines-Young pool	18
1.4.3	Coexistence of three dynamical regions	20
1.4.4	Intersecting fronts	23
1.5	Conclusions	24
	References	25
<b>2</b>	<b>The two-layer Stommel problem with outcropping: A numerical approach</b>	<b>29</b>
2.1	Introduction	29
2.2	Model equations	31
2.3	Numerical method	34
2.4	Results	35
2.4.1	Deep-ocean regime	37



2.4.2 Intermediate regime . . . . .	39
2.4.3 Shallow-ocean regime . . . . .	42
2.5 Discussion . . . . .	44
2.5.1 Geostrophic contours . . . . .	44
2.5.2 Effect of adiabatic constraint on outcropping . . . . .	46
2.5.3 Matching of ventilated and unventilated regions . . . . .	46
2.6 Application to the observational evidence . . . . .	54
2.7 Conclusions . . . . .	56
References . . . . .	57
<b>Appendix to Chapter 2 Numerical solution to Parsons' Model using TVD schemes</b> . . . . .	<b>61</b>
A.1 Introduction . . . . .	61
A.2 Model equations . . . . .	62
A.3 Numerical Method . . . . .	63
A.4 Wave propagation . . . . .	66
A.4.1 Propagation of a planetary eddy . . . . .	66
A.4.2 Spin-up of an equatorial ocean . . . . .	70
A.5 Subtropical gyre . . . . .	72
A.6 Conclusions . . . . .	77
References . . . . .	78

## PART II OTHER PROBLEMS

<b>3 Potential vorticity homogenization in a two-layer wind-driven gyre</b> . . . . .	<b>83</b>
3.1 Introduction . . . . .	83
3.2 Model equations and numerical method . . . . .	85
3.3 Numerical results . . . . .	87
3.4 The Sverdrup interior . . . . .	95
3.4.1 Homogenization mechanism . . . . .	95
3.4.2 Thermal analogy . . . . .	99
3.5 The western boundary layer . . . . .	99
3.6 Observation and realistic dynamical regime . . . . .	103
3.6.1 Levitus'94 maps . . . . .	103
3.6.2 Solution of planetary geostrophic equations . . . . .	103
3.7 Conclusions . . . . .	107
References . . . . .	108

<b>4 Gyres induced by curl-free winds in the tropics</b> . . . . .	<b>111</b>
4.1 Introduction . . . . .	111
4.2 Basic mechanism of rotational flows . . . . .	113
4.3 Numerical results . . . . .	115
4.4 Discussion . . . . .	119
4.4.1 Comparison with the OGCM results . . . . .	119
4.4.2 Relation to the atmospheric phenomenon . . . . .	120
4.5 Conclusions . . . . .	121
References . . . . .	122
<b>5 The concept of JEBAR: Evolution of baroclinic planetary eddies over localized bottom topography</b> . . . . .	<b>125</b>
5.1 Introduction . . . . .	125
5.2 Formulation . . . . .	127
5.2.1 The planetary geostrophic equations . . . . .	129
5.2.2 The quasigeostrophic equations . . . . .	130
5.3 The model . . . . .	131
5.4 JEBAR on the planetary geostrophic motion . . . . .	132
5.4.1 Overview . . . . .	132
5.4.2 JEBAR forcing and barotropic flow field . . . . .	133
5.4.3 Westward motion of the baroclinic field . . . . .	133
5.4.4 Energy conversion . . . . .	141
5.5 JEBAR on the quasigeostrophic motion . . . . .	142
5.6 Conclusions . . . . .	146
References . . . . .	147



## Summary

In Chapter 1, Sverdrup dynamics is reformulated based on a hyperbolic system of two-layer planetary geostrophic equations in place of the standard approach using the vorticity equation. The integral conservation laws of momentum are introduced to investigate solutions which may include jump discontinuities subject to the eastern boundary condition. An oceanic front such as a surfacing line and a closed geostrophic contour is interpreted as a "shock" across which the following jump conditions derived from these integral constraints are satisfied:

$$\begin{bmatrix} p \end{bmatrix} = \begin{bmatrix} h_1 - \frac{h_1^2}{2H} \end{bmatrix}, \quad f \begin{bmatrix} \psi_1 \end{bmatrix} = \begin{bmatrix} \frac{h_1^2}{2} - \frac{h_1^3}{3H} \end{bmatrix},$$

where  $p$  is the (nondimensional) depth-independent pressure,  $h_1$  is the upper-layer thickness,  $H$  is the total depth,  $f$  is the Coriolis parameter and  $\psi_1$  is the upper-layer streamfunction. These may be used to determine suitable positions of fronts separating different dynamical regions if the interface structure for each subdomain is specified. Several examples demonstrate the applicability of this approach: Of particular interest is the finite-depth version of Parsons' model, in which case we can obtain the exact solution for the surfacing line in contrast to the asymptotic solution derived by Kamenkovich and Reznik (1972). It is also found that a surfacing line for Parsons' model, which is the limit as  $H \rightarrow \infty$ , can be determined in advance provided that the wind forcing and the boundary values are prescribed. The present inviscid/hyperbolic perspective eliminates the need for the semigeostrophic condition used in similar studies by Parsons (1969), Veronis (1973) and Huang and Flierl (1987).

In Chapter 2, a two-layer planetary geostrophic model with interfacial and bottom frictions is examined numerically. We have found a class of solutions which are characterized by a viscous interior layer associated with outcropping. When the lower layer is very thick, Parsons-type solutions are reproduced. The numerical solutions are in gross qualitative agreement with the analytical solutions of Kamenkovich and Reznik (1972), although compensation seems to be imperfect near the western boundary even when the total depth is ten times the upper-layer thickness. When the lower layer is moderate, namely, as thick as the whole thermocline, the solutions are characterized by the ventilated circulation contained in the unventilated pool. When the lower layer is thin, the ventilated and unventilated circulations are separated between which the

submerged layer is perfectly compensated. It is shown that the interface displacement between the outcrop and the pool increases as the bottom friction coefficient decreases, implying a jump discontinuity in an inviscid limit. With sufficiently strong winds, a part of the ventilated circulation cannot enter the western boundary layer to close on itself in the eastern part of the interior. These types of solutions (the moderate and thin cases) cannot be covered by the so-called ventilated thermocline theory developed in the 1980s. This is primarily because the latter "modern" theory assumes the tight thermal interaction between the ocean and the atmosphere implicitly; the gyre cannot be closed near the western coast. It is also suggested that the inviscid models for the ventilated thermocline may be developed further by taking into account jump discontinuities.

In Appendix to Chapter 2, various TVD schemes are applied to a 1.5-layer planetary geostrophic model and are successful in representing the outcropping lower layer numerically. Two preliminary experiments concerning the evolution of a conceptual planetary eddy and the spin-up of an equatorial ocean confirm that Yee's (both symmetric and upwind) schemes capture the propagation of a baroclinic long Rossby wave reasonably well. It is also verified that the symmetric scheme is slightly more diffusive than the upwind scheme. These TVD schemes can reproduce a subtropical gyre with interior jets; the numerical solutions are in good qualitative agreement with Parsons' analytical solution. However, the upwind scheme creates a spurious overshooting of the western boundary current when a coarse grid is used, as has been met by the previous workers using the FCT algorithm. The numerical solutions with sufficiently fine grids show that the western boundary layer separates at a higher latitude compared with the analytical solution. This disagreement suggests that the simple composite expansion using the western boundary layer and the interior layer, as performed by Parsons (1969), does not seem to provide the correct behavior of boundary layer separation.

In Chapter 3, a wind-driven subtropical gyre with a frictional western boundary current is investigated using a two-layer quasigeostrophic model without the advection of relative vorticity. It is shown that homogenization of the lower-layer potential vorticity  $q_2$  occurs when the zonal advective motion is so retarded by the baroclinic long Rossby wave that information on  $q_2$  cannot propagate eastward from the western boundary layer. The southward Sverdrup flow simply advects  $q_2$ -contours to leave a gap which should be filled with uniform potential vorticity if the direct vorticity input by the source term remains small. These requirements may be satisfied provided that

$$F_2 < \frac{2}{\pi}, \quad F_2 \delta_2 \ll \frac{1}{\pi^2},$$

where  $F_2 = F/\alpha$ ,  $\delta_2 = \delta/\alpha$  ( $F$ : the baroclinic rotational Froude number,  $\delta$ : the bottom friction coefficient,  $\alpha$ : the ratio of the mean lower- to upper-layer thickness). It is confirmed that this prediction agrees well with the numerical results. It is also found

that this condition is consistent with the structure of the viscous western boundary layer: When  $F_2 \gg 1$ , the boundary layer for  $q_2$  is closely related to the heat equation and has the width  $O(F_2^{-1/2}\delta)$ . Since it is narrower than the boundary current of width  $O(\delta)$ , the interior distribution of  $q_2$  is strongly affected by the boundary current. When  $F_2$  satisfies the above inequalities, however, the  $q_2$ -layer becomes wider than the boundary current, so that the uniform distribution of  $q_2$  in the interior may be matched with the boundary values.

In Chapter 4, a 2.5-layer model is examined to provide a mechanism which can generate steady equatorial gyres without nonlinearity even if zonal winds have no curl. Divergent flows directly driven by the winds are maintained with the aid of diapycnal density mixing to produce vortex stretching, which acts as an external forcing in a vorticity equation, so that rotational barotropic flows are induced in each layer. This process always leads to rotational stacked gyres however small the mixing coefficients may be. This mechanism may be applied to possible barotropic circulations in the tropics. For easterly winds, a 2.5-layer model is a reasonable approximation for the equatorial ocean because of the equatorial upwelling. In this case, the vertically integrated transport may be cyclonic if the density mixing in the middle layer is so strong that the undercurrent overwhelms the surface jet. For westerly winds, on the other hand, the Ekman downwelling allows to use a 1.5-layer model as a better simplification for the equatorial ocean, and hence the cyclonic gyres are naturally obtained. In this way, we expect a pair of cyclonic barotropic gyres straddling the equator regardless of the zonal wind direction. This surprising property is actually observed in the several OGCM results (e.g., Semtner and Holland, 1980; Philander and Pacanowski, 1980; Liu et al., 1994). We suggest, therefore, that diapycnal density mixing is one way to extract cyclonic vorticity from the rotating solid earth which establishes a suitable density stratification in accordance with the direction of zonal winds.

In Chapter 5, the concept of JEBAR and its advantage are demonstrated in terms of a time-dependent problem concerning more idealistic situations, because JEBAR still causes a lot of misleading understandings. Numerical experiments have been conducted to investigate the evolution of pure baroclinic eddies using two-layer planetary geostrophic equations in the presence of localized bottom topography. It is shown that the emission of barotropic flows (or waves), westward acceleration and energy conversion occur when an eddy interacts with bottom topography. A meridional ridge acts as a repeller for a cold eddy and an attractor for a warm eddy due to JEBAR-induced barotropic flows (or waves), which is consistent with the vorticity argument. This mechanism may provide a possible explanation not only for the global distribution of the phase speed of baroclinic Rossby waves observed in the Pacific by the TOPEX/POSEIDON satellite altimeter but also for the abrupt change in the trajectories of the westward propagating baroclinic eddies observed in the North Atlantic.



## PART I

DISCONTINUOUS SOLUTIONS OF TWO-LAYER  
PLANETARY GEOSTROPHIC EQUATIONS



## Chapter 1

### Discontinuities in the Sverdrup interior

#### 1.1 Introduction

A class of geostrophic motions whose horizontal scale is much larger than the baroclinic deformation radius is regularly observed in the broad spectrum of oceanic and atmospheric motions. Historically, Burger (1958) first noticed the special geostrophic regime suitable for these extremely large-scale motions in the atmosphere by carefully implementing the scale analysis and showed that such motions do not obey the traditional quasigeostrophic equations used in weather forecastings. This is because these so-called planetary geostrophic motions are characterized by  $O(1)$  geostrophic divergence. Phillips (1963) revisited Burger's analysis with a particular attention to the variations of potential vorticity and extended the ideas to oceanic motions, although oceanographers had already utilized a simplified set of equations, so-called planetary geostrophic equations, in order to describe the steady, wind-driven ocean circulation (Sverdrup, 1947). The importance of vortex stretching of finite amplitude was demonstrated systematically by Yamagata (1982) together with some interesting applications to "intermediate-scale" motions [see also the review of Charney and Flierl (1981)]. Later, various geostrophic regimes are categorized in detail with respect to some representative dimensionless parameters (Williams and Yamagata, 1984; Cushman-Roisin et al., 1992). The nonlinear evolution of baroclinic nondispersive Rossby waves is a significant manifestation of planetary geostrophy, which has been studied rather extensively (e.g., Anderson and Killworth, 1979; Johnson and Willmott, 1981; Willmott, 1985; Dewar, 1987).

Since Robinson and Stommel (1959) and Welander (1959), theoretical models for the oceanic thermocline and associated baroclinic motions have been developed based mainly on the planetary geostrophic equations due to  $O(1)$  vertical variations of isopycnal surfaces. As for layer models, Luyten et al. (1983) established a general procedure for dealing with the steady wind-driven circulation with outcropping layers under the Sverdrup constraint. In their conservative theory, a surfacing line is prescribed either directly (e.g., Luyten et al., 1983; Luyten and Stommel, 1986) or indirectly (Schopp

and Arhan, 1986) on which the boundary values must be imposed in order to solve the problem by the method of characteristics in the submerged parts of the ventilated layers. The problem is, thus, essentially overdetermined, but it does not matter in the original theory of Luyten et al. (1983), because the easternmost characteristic emanating from the surfacing line deflects westward leaving a shadow zone to the east. Schopp and Arhan (1986), on the other hand, treated the opposite cases when a characteristic deflects eastward and even plunges into the eastern boundary; the resulting slope of the interface along the eastern boundary may be removed by implicitly taking into account an eastern boundary layer.

Parsons (1969) tackled with a similar problem of the wind-driven subtropical gyre using a 1.5-layer model quite differently in the sense that the boundary values are given only on the eastern boundary so that the surfacing line is part of a solution [see also Huang (1991)]. Since the present approach is essentially similar to Parsons' approach, it is fair to review the basic reduced gravity model critically for later convenience. Consider a square basin on a  $\beta$ -plane ranging  $0 \leq x \leq 1$  and  $-0.5 \leq y \leq 0.5$  in nondimensional unit (see Appendix 1 for the scalings). The governing equations for a steady, planetary geostrophic flow in the oceanic interior can be written in dimensionless form as

$$-f\psi_x = -h h_x + \lambda \tau^x, \quad (1.1)$$

$$-f\psi_y = -h h_y, \quad (1.2)$$

where  $h$  is the layer thickness,  $\psi$  is the transport streamfunction,  $f = 1 + \beta y$  is the Coriolis parameter,  $\tau^x = \sin \pi y$  is the zonal wind forcing, and  $\beta$  and  $\lambda$  are nondimensional parameters. The boundary condition is assumed to be

$$\psi = 0, \quad h = h_e = \text{const.} \quad \text{at } x = 1, \quad (1.3)$$

i.e., there is no normal geostrophic flow on the eastern boundary. The standard procedure for solving this problem is to make the vorticity equation (the Sverdrup relation) using (1.1)–(1.2) and to integrate it afterwards with respect to  $x$  subject to (1.3). The result is

$$\psi = \psi_s \equiv \frac{\lambda}{\beta} (1-x) \tau_y^x, \quad (1.4)$$

$$h^2 = h_s^2 \equiv h_e^2 + \frac{2f^2}{\beta} (1-x) \left( \frac{\tau^x}{f} \right)_y \quad (1.5)$$

(e.g., Welander, 1966). No difficulty is involved in the above derivation.

Parsons (1969) and later Veronis (1973) and Huang and Flierl (1987) extended the above basic model to the case when layer outcropping occurs. Friction plays a crucial

role in their models because they shed light on the separation of the western boundary current, so that the governing equations are

$$-f\psi_x = -h h_x + \epsilon \psi_y / h + \lambda \tau^x, \quad (1.6)$$

$$-f\psi_y = -h h_y - \epsilon \psi_x / h, \quad (1.7)$$

where  $\epsilon (\ll 1)$  is the dimensionless friction coefficient. They determined the position of the surfacing line by matching the Sverdrup interior (1.4)–(1.5) with the frictional interior layer which is assumed to be created in relation to outcropping. Instead of the explicit form of the solution for the interior layer, they introduced a simple relation, so-called the *(semi)geostrophic condition*, which represents the leading-order balance (i.e., cross-stream geostrophy) in the interior layer. This is the reason why the expression for the surfacing line is independent of the friction coefficient. It seems paradoxical, however, that the assumption of the existence of the interior layer, however thin it may be, is responsible to the derivation leading to the geostrophic condition. Obviously, the same procedure no longer works for the inviscid equations (1.1)–(1.2). Is the surfacing line found by Parsons an intrinsic property of the latter equations? The potential difficulty arising from Parsons' approach may stem from the use of the differential equations (1.6)–(1.7) to treat an outcrop which may give rise to jump discontinuities in the dependent variables. However, such discontinuous solutions are possible as "weak solutions" of the hyperbolic system (1.1)–(1.2) provided that a basic integral conservation law is properly employed.

In this chapter, we focus on a first integral of motion in order to outline Sverdrup dynamics when discontinuities are permitted. Of particular interest is another physical interpretation of oceanic fronts from the standpoint of the inviscid/hyperbolic problem. It should be noted that integral conservation laws have not been discussed extensively in large-scale ocean dynamics. In fact, the major theories on the wind-driven circulation are based on the vorticity equation. This is probably because one usually assumes the Sverdrup interior to be continuous. A clear exception is Dewar (1991) who established a procedure for the planetary geostrophic thermocline allowing jump discontinuities which are smoothed out by density mixing. Salmon (1992) also took full advantage of hyperbolic characters of two-layer planetary geostrophic equations to construct flows with jump discontinuities over a continental slope. However, many of the previous workers commonly used the barotropic and baroclinic equations as the characteristic equations.

Since the reduced gravity equations are a special case of corresponding two-layer planetary geostrophic equations, we start with the latter equations in Section 1.2. The problem searching for a surfacing line in Parsons' model is treated in Section 1.3. Some illustrative examples of the two-layer model using the suggested approach are provided



in Section 1.4.<sup>1</sup>

## 1.2 The two-layer model

We consider the steady wind-driven ocean circulation governed by the following two-layer planetary geostrophic equations (1.1)–(1.2):

$$h_1 p_x - f \psi_{1x} = \lambda \tau^x, \quad (1.8)$$

$$h_1 p_y - f \psi_{1y} = 0, \quad (1.9)$$

$$h_2(p - h_1)_x - f \psi_{2x} = 0, \quad (1.10)$$

$$h_2(p - h_1)_y - f \psi_{2y} = 0 \quad (1.11)$$

where  $p$  is the pressure and an obvious notation is used for the quantities for each layer. The boundary condition is

$$\psi_1 = \psi_2 = 0, \quad p = p_e = \text{const.}, \quad h_1 = h_e = \text{const.} \quad \text{at } x = 1. \quad (1.12)$$

With the moving lower layer, the Sverdrup function (1.4) means the barotropic transport, i.e.,

$$\psi_1 + \psi_2 = \psi_s, \quad (1.13)$$

so that the smoothness of the Ekman pumping is guaranteed.

### 1.2.1 The integral conservation law of momentum and associated jump conditions

Adding the upper-layer equations (1.8), (1.9) to the lower-layer equations (1.10), (1.11) gives

$$H(p - h_1)_x + h_1 h_{1x} - f \psi_{sx} = \lambda \tau^x, \quad (1.14)$$

$$H(p - h_1)_y + h_1 h_{1y} - f \psi_{sy} = 0, \quad (1.15)$$

respectively, where  $H$  is the total depth. These equations constitute a hyperbolic system and are already in characteristic form with the characteristics  $y = \text{const.}$  and  $x = \text{const.}$ , respectively, viz.,

$$\frac{d}{dx} \left[ H(p - h_1) + \frac{h_1^2}{2} - f \psi_s \right] = \lambda \tau^x \quad \text{on } y = \text{const.}, \quad (1.16)$$

$$\frac{d}{dy} \left[ H(p - h_1) + \frac{h_1^2}{2} - f \psi_s \right] = -\beta \psi_s \quad \text{on } x = \text{const.} \quad (1.17)$$

<sup>1</sup>In the earlier version of this chapter (Sakamoto, 1998), the analysis of the two-layer equations is postponed after the analysis of the 1.5-layer equations, because the original manuscript focuses on Parsons' model.

In particular, (1.16) can be integrated with respect to  $x$  from the eastern boundary to give

$$H(p - h_1) + \frac{h_1^2}{2} - f \psi_s = H(p_e - h_e) + \frac{h_e^2}{2} - \lambda(1 - x)\tau^x. \quad (1.18)$$

This is a first integral of motion, the integral of momentum in the  $x$ -direction, for the present two-layer problem. If (1.16) is integrated from  $x = x_1$  to  $x_2$  ( $0 < x_1 \leq x_2 \leq 1$  for definiteness), we have

$$[P_2]_{x=x_1}^{x=x_2} = \frac{\lambda}{H}(x_2 - x_1) \left( \tau^x - \frac{f}{\beta} \tau_y^x \right), \quad (1.19)$$

where

$$P_2 \equiv p - h_1 + \frac{h_1^2}{2H}. \quad (1.20)$$

This relation may be regarded as the integral conservation law of momentum in the  $x$ -direction. Similarly, integrating (1.17) from  $y = y_1$  to  $y_2$  yields the meridional counterpart:

$$[P_2]_{y=y_1}^{y=y_2} = -\frac{\lambda}{H}(1 - x) \left[ \tau^x - \frac{f}{\beta} \tau_y^x \right]_{y=y_1}^{y=y_2}. \quad (1.21)$$

In the non-outcrop region,  $p_x$  and  $p_y$  may be eliminated from (1.8) and (1.9) using (1.14) and (1.15), respectively. Integrating the resulting equations, we have

$$[G_2]_{x=x_1}^{x=x_2} = \int_{x_1}^{x_2} \left( \frac{h_2}{H} \lambda \tau^x - \frac{h_1}{H} f \psi_{sx} \right) dx, \quad (1.22)$$

$$[G_2]_{y=y_1}^{y=y_2} = \int_{y_1}^{y_2} \left( -\beta \psi_{1x} - \frac{h_1}{H} f \psi_{sy} \right) dy, \quad (1.23)$$

where

$$G_2 \equiv \frac{h_1^2}{2} - \frac{h_1^3}{3H} - f \psi_{1x}. \quad (1.24)$$

We call  $G_2$  tentatively the *geostrophic function* for the two-layer equations. Eq. (1.22) can be represented in the alternative form

$$\left[ \frac{h_1^2}{2} - \frac{h_1^3}{3H} - f \psi_{1x} \right]_{x=x_1}^{x=x_2} + \frac{\lambda}{H} \left( \tau^x - \frac{f}{\beta} \tau_y^x \right) \int_{x_1}^{x_2} h_1 dx = \lambda(x_2 - x_1)\tau^x. \quad (1.25)$$

We assume that these integral conservation laws remain valid even when discontinuities occur in the interior. Since the boundary condition is imposed on the eastern boundary,

<sup>2</sup>The equations (1.14) and (1.15) can also be rewritten using a single scalar function  $B$  as  $\nabla B = 0$ , where

$$B \equiv H(p - h_1) + \frac{h_1^2}{2} - f \psi_s + \lambda(1 - x)\tau^x.$$

This function may be regarded as the Bernoulli function for the two-layer system. The flux function  $P_2$  is obtained by subtracting the given (and hence continuous) terms from  $B$ .



(1.19) or (1.22) may be used to decide the relation between  $p$  and  $h_1$  or between  $\psi_1$  and  $h_1$  at any point in the interior.

If it is also assumed that  $h_1$  and  $\psi_1$  are at most as singular as the step function, the above integral constraints yield the following jump conditions:

$$[P_2] = 0, \text{ i.e., } [p] = \left[ h_1 - \frac{h_1^2}{2H} \right], \quad (1.26)$$

$$[G_2] = 0, \text{ i.e., } f[\psi_1] = \left[ \frac{h_1^2}{2} - \frac{h_1^3}{3H} \right]. \quad (1.27)$$

An outcrop may be included in the present two-layer system by defining a surfacing line as a front across which (1.27) is satisfied. We note that a surfacing line is accompanied with a jump discontinuity in  $\psi_1$  and  $p$  unless the corresponding outcrop is *spontaneous*, i.e., the interface is exposed to the surface as it should be.<sup>3</sup>

### 1.2.2 An alternative expression for the system of the two-layer equations

From the definition (1.24) with (1.22), we have the conservation law of  $G_2$ :

$$\frac{dG_2}{dy} = 0 \quad \text{on } x = X(y), \quad (1.28)$$

where  $X(y)$  satisfies

$$\frac{\lambda}{H} \left( \tau^x - \frac{f}{\beta} \tau^y \right) \int_1^{X(y)} h_1 dx + \lambda [1 - X(y)] \tau^x = g_c \equiv \text{const.} \quad (1.29)$$

Eq. (1.28) is also in characteristic form in the sense that the characteristic  $x = X(y)$  carries information from a latitude circle on which boundary values must be prescribed.<sup>4</sup> It is found that characteristic curves cannot always be determined in advance because (1.29) depends on the solution  $h_1$ . The characteristic equation (1.29) suggests an important hyperbolic property of the Sverdrup interior: Discontinuous derivatives of  $G_2$  and hence discontinuities in  $h_1$  and  $\psi_1$  are possible on the characteristic  $x = X(y)$  [e.g., Chapter 5 of Whitham (1974)]. This means that when discontinuities occur at a point  $x = X_1(y_i)$  along a particular "initial" latitude circle  $y = y_i$ , information on these discontinuities can propagate along the corresponding characteristic curve  $x = X_1(y)$ .

Using (1.22) and (1.23), the total derivative on the left-hand side of (1.28) reads

$$\frac{dG_2}{dy} = -\beta \psi_1 - \frac{h_1}{H} f \psi_{sy} + X'(y) \left( \frac{h_2}{H} \lambda \tau^x - \frac{h_1}{H} f \psi_{sx} \right), \quad (1.30)$$

<sup>3</sup>An exception may occur in the vicinity of the equator where  $f \approx 0$ . It is found from the jump condition (1.47) that an outcrop at the equator must be spontaneous (cf. Appendix to Chapter 2).

<sup>4</sup>This equation may be obtained by a rotation of the axes so that the new coefficient matrix is nonsingular, which will be clearer in the case of the 1.5-layer model.

hence  $\psi_1$  is formally represented as

$$\psi_1 = \frac{h_2 \lambda}{H \beta} X'(y) \tau^x - \frac{h_1}{H \beta} \frac{f}{dy} \quad \text{on } x = X(y) \quad (1.31)$$

in the non-outcrop region. We note that all the expressions, (1.27)–(1.31), are reduced to the corresponding formulas for the reduced gravity model as  $H \rightarrow \infty$ .

Consequently, we have gained the alternative system in terms of  $h_1$  and  $\psi_1$  which may describe discontinuous planetary geostrophic motions in the immiscible two-layer fluid. The new system contains the Sverdrup constraint (1.13), the integral conservation law of momentum (1.25) or its differential form (1.31), and the jump condition (1.27). However, a unique solution cannot be obtained from these inviscid equations, because we do not assume so far any mechanism which drives motions in the lower layer. In fact, taking the curl of (1.10) and (1.11) yields the lower-layer vorticity equation

$$J(\psi_2, q_2) = 0, \quad (1.32)$$

where  $q_2 = f/h_2$ . This implies the functional relationship between  $\psi_2$  and  $q_2$ :

$$\psi_2 = \Phi(q_2), \quad (1.33)$$

where  $\Phi$  is arbitrary. One way to proceed is of course to specify  $\Phi$  in (1.33), i.e., we assume implicitly the role of the western boundary layer in the interior, or even thermohaline effects. But the present approach is rather different: Once the thermocline structure in each subdomain is given, adequate positions of fronts between these subdomains may be determined from the jump condition (1.27). Then, the corresponding flow fields are calculated using (1.25) subject only to the eastern boundary condition. This procedure is demonstrated with some typical examples in Section 1.4.

## 1.3 The reduced gravity model

### 1.3.1 Hyperbolic perspective of Parsons' model

We return to the reduced gravity equations (1.1)–(1.2) with the eastern boundary condition (1.3). Although the result which will be presented below may be immediately obtained from the result for the two-layer model by taking the limit as  $H \rightarrow \infty$ , the argument is repeated here to emphasize the hyperbolic perspective of the reduced gravity model. Because of this particular limit, however, the reduced gravity equations cannot have any front other than surfacing lines under the condition of the smooth Ekman pumping. Furthermore, the lower-layer motion should be implicit in the outcrop region due to the Sverdrup constraint.

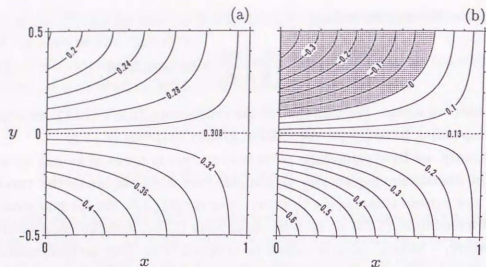


**Figure 1.1.** Contours of  $G$  for (a)  $\lambda = 0.13$ ,  $h_c = 0.7855$ , and (b)  $\lambda = 0.53$ ,  $h_c = 0.51$  ( $\beta = 0.55$  in common). Also shown is the asymptote  $y = 0$  denoted by the dotted line. Contour intervals are (a) 0.02, (b) 0.05, respectively. The region of negative values is shaded.

From (1.1) with (1.3), the integral of momentum in the  $x$ -direction is found to be

$$\frac{h^2}{2} - f\psi + \lambda(1-x)\tau^x = \frac{h_c^2}{2}, \quad (1.34)$$

and the integral conservation law of momentum is given by

$$\left[ \frac{h^2}{2} - f\psi \right]_{x=x_1}^{x=x_2} = \lambda(x_2 - x_1)\tau^x. \quad (1.35)$$

By the analogy of the two-layer case, we define the geostrophic function for the 1.5-layer equations,  $G$ , by the momentum flux on the left-hand side of (1.35):

$$G \equiv \frac{h^2}{2} - f\psi. \quad (1.36)$$

From the integral (1.34),  $G$  can also be written as

$$G = \frac{h_c^2}{2} - \lambda(1-x)\tau^x, \quad (1.37)$$

so that  $G$  is decisive provided the wind forcing and the eastern boundary condition are prescribed, in contrast to  $G_2$ . Figure 1.1 shows the distribution of  $G$  for two pairs of  $(\lambda, h_c)$ . It is found that negative values are seen when  $h_c^2/\lambda$  becomes small, for which a special treatment is needed as will be discussed later. If we set  $G = g_c \equiv \text{const.}$ , the isolines of  $G_{1.5}$  are represented in parametric form as

$$x = X(y) = 1 - \left( \frac{h_c^2}{2} - g_c \right) \frac{1}{\lambda\tau^x}. \quad (1.38)$$

We note that  $y = 0$  is also an isoline of  $G$  as confirmed from (1.34) although (1.38) is invalid there. Actually, the two straight lines,  $x = 1$  and  $y = 0$ , are asymptotes of (1.38) on which  $G = h_c^2/2$  (see Fig. 1.1).

In the continuously differentiable part of the basin, the familiar Sverdrup interior can be reproduced from the integral (1.34) straightforwardly. Differentiating (1.34) with respect to  $y$  leads to

$$hh_y - f\psi_y - \beta\psi = -\lambda(1-x)\tau_y^x. \quad (1.39)$$

Comparing this with (1.2), we have

$$\psi = \frac{\lambda}{\beta}(1-x)\tau_y^x, \quad (1.40)$$

which is indeed the Sverdrup function  $\psi_s$  given in (1.4). The corresponding expression for  $h$  is immediately obtained again from (1.34) using (1.40) as

$$h^2 = h_c^2 - 2\lambda(1-x)\tau^x + \frac{2f\lambda}{\beta}(1-x)\tau_y^x, \quad (1.41)$$

and hence proves to be the same as  $h_s$  in (1.5).

The definition (1.36) with (1.38) leads to a conservation law of  $G$ :

$$\frac{dG}{dy} = 0 \quad \text{on } x = X(y), \quad (1.42)$$

or equivalently,

$$h[h_y + X'(y)h_x] - f[\psi_y + X'(y)\psi_x] - \beta\psi = 0, \quad (1.43)$$

where

$$X'(y) = \left( \frac{h_c^2}{2} - g_c \right) \frac{\tau_y^x}{\lambda(\tau^x)^2} \quad (1.44)$$

corresponds to the characteristic speed. Using (1.44) and (1.38), the Sverdrup function (1.40) may be represented as

$$\psi = \frac{\lambda}{\beta}X'(y)\tau^x. \quad (1.45)$$

Substitution of (1.45) into (1.43) yields

$$X'(y)(hh_x - f\psi_x - \lambda\tau^x) + (hh_y - f\psi_y) = 0, \quad (1.46)$$

which is the linear combination of the original equations (1.1)–(1.2); the multiplier  $(X', 1)$  is obviously the direction vector for the trajectory  $x = X(y)$ . It turns out, therefore, that the conservation equation (1.42) with (1.38) is consistent with the original system (1.1)–(1.2) under the Sverdrup constraint (1.40).



The characteristic equation (1.42) suggests that discontinuous derivatives in  $G$  and hence a surfacing line is possible on the characteristic  $x = X(y)$ . The jump condition deduced from the integral conservation law (1.35) is found to be

$$[G]_{x=X-}^{x=X+} = 0. \quad (1.47)$$

Since over the outcrop  $h = \psi = 0$  indicating that  $g_c = 0$  in (1.38), the surfacing line must be the zero contour of  $G$  (see Fig. 1.1):

$$x = X_0(y) \equiv 1 - \frac{h_c^2}{2\lambda\tau^x}. \quad (1.48)$$

Similarly, a surfacing line for a zonal wind of the general form  $\tau^x(x, y)$  is represented implicitly by

$$\int_{X_0(y)}^1 \tau^x(x, y) dx = \frac{h_c^2}{2\lambda}. \quad (1.49)$$

From this expression, we can confirm some well-known qualitative features of an outcrop; i.e., it becomes large as  $h_c^2/\lambda$  decreases and does not exist for  $\tau^x \leq 0$ . We note again that the expression for the surfacing line may be derived from the zonal momentum equation (1.1) only.

Since there exists only one surfacing line over the basin (Fig. 1.1b) and since  $h \neq 0$  at the eastern boundary, the outcrop region lies west of the surfacing line. Therefore, we have the following useful rule for determining the location of an outcrop geometrically: *For the hyperbolic system (1.1)–(1.2), outcropping may occur where  $G \leq 0$ .* In the domain  $G < 0$ , the values of  $h$ ,  $\psi$  and  $G$  must be replaced by 0. Accordingly, the double-valued parts of the solutions for  $h$  and  $\psi$  are replaced by corresponding jump discontinuities. These discontinuities are acceptable in view of the hyperbolic properties of the reduced gravity equations. In this way, we may avoid the breakdown of the original equations (1.1)–(1.2) over the outcrop. In fact, using (1.40), (1.41) and (1.48), we can verify that

$$\left(\frac{h_c^2}{2} - f\psi_s\right) - \left(\frac{0^2}{2} - f \cdot 0\right) = 0 \quad \text{on } x = X_0(y), \quad (1.50)$$

or concisely

$$[G]_{x=X_0-}^{x=X_0+} = 0. \quad (1.51)$$

That is, the jump condition (1.47) is satisfied across the surfacing line. Now, the formal correspondence between the present approach and the matching procedure developed by Parsons (1969) becomes clear.

Finally, to get a physically consistent solution, the constant  $h_c$  may be determined from the prescribed total volume (Parsons, 1969). In Fig. 1.1, the values of  $h_c$  have been chosen so that the total volume is unity.

Consequently, we are successful in reproducing the surfacing line in Parsons' model using the inviscid equations (1.1)–(1.2) subject to (1.3) without further approximations. The integral conservation law of momentum (1.35) is employed in order to take into account discontinuities in the solution. We have shown that the surfacing line must lie on one of the  $G$ -contours and appears as a "shock front" across which the jump condition (1.51) is satisfied.

### 1.3.2 Effect of small friction

The most significant effect of the friction terms in (1.6)–(1.7) on the flow constructed in the preceding sections is to produce return currents in thin boundary layers to assure mass continuity. The discontinuities in  $h$  and  $\psi$  on the surfacing line may be smoothed out and replaced by a sharp interior layer, while the discontinuities on the western boundary may be replaced by a familiar western boundary layer. The problem governed by (1.6)–(1.7) now becomes elliptic, so that a characteristic form no longer exists. However, from the singular perturbation point of view, the first integral of motion (1.34), the integral conservation law of momentum (1.35) and the notion of the geostrophic function (1.38) may still be applicable to the outer solutions of the problem. Thus, the present argument may be followed by Parsons' analysis of the frictional layers to accomplish the whole story.

### 1.3.3 Effect of density mixing

Another physical process which may invalidate hyperbolicity of the system is diapycnal density mixing  $w_m$  introduced in the continuity equation as follows:

$$(uh)_x + (vh)_y = w_m, \quad (1.52)$$

where  $(u, v)$  is the velocity. Thus, the velocity may be the sum of the rotational part  $\mathbf{v}_R$  and the divergent part  $\mathbf{v}_D$  such that

$$\mathbf{v}_D = \nabla\phi, \quad \mathbf{v}_R = \mathbf{k} \times \nabla\psi, \quad (1.53)$$

where  $\phi$  is the velocity potential (cf. Chapter 4). Eq. (1.52) then yields a Poisson equation for  $\phi$ ,

$$\nabla^2\phi = w_m, \quad (1.54)$$

while the momentum equations (1.1)–(1.2) are modified as

$$hh_x - f\psi_x = \lambda\tau^x + fv_D, \quad (1.55)$$

$$hh_y - f\psi_y = -fu_D. \quad (1.56)$$



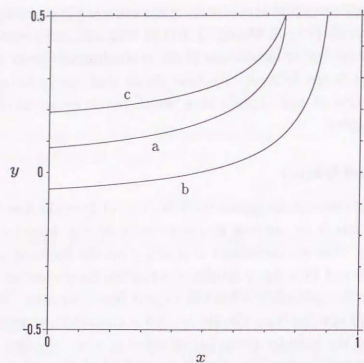


**Figure 1.2.** Surfacing lines when divergent meridional flow of the form  $v_D = \gamma(y \pm 0.5)$ ,  $\gamma > 0$  is applied to the adiabatic case (a) which is the same as in Fig. 1.1b. (b) Cooling case [ $v_D = \gamma(y + 0.5)$ ]. (c) Heating case [ $v_D = \gamma(y - 0.5)$ ].

Since  $w_m$  may depend on solution, the system (1.55)–(1.56) is not generally hyperbolic. Suppose, however, that  $w_m$  is a prescribed function as in some of the previous studies on mixed wind-driven and thermohaline circulations (e.g., Luyten and Stommel, 1986). Then, (1.54) can be solved by itself in principle, so that the divergent flow on the right-hand sides of (1.55)–(1.56) can be regarded as external forcing. Thus, the argument on the construction of a surfacing line developed previously can be applied to the system (1.55)–(1.56), and the surfacing line is found to be represented by

$$x = \frac{h_c^2}{2} \frac{1}{\lambda \tau^x + f v_D}. \quad (1.57)$$

But the basic Sverdrup function (1.4) must be replaced by

$$\psi_s = -\frac{1}{\beta} \int_1^x [\lambda \tau_y^x + \nabla \cdot (f v_D)] dx, \quad (1.58)$$

i.e., the total transport may be induced by the planetary divergence (see also Chapter 4).

As a simple example, we give the divergent flow as follows:

$$u_D = 0, \quad v_D = \gamma(y \pm 0.5) \quad \gamma > 0, \quad (1.59)$$

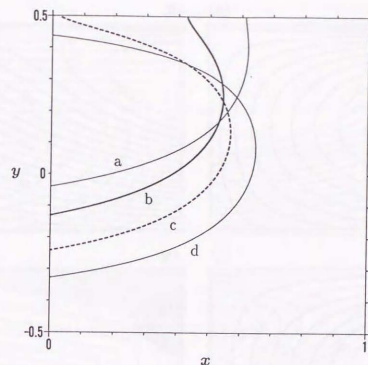


**Figure 1.3.** Surfacing lines in the two-layer model for different values of  $H$  when the lower layer is perfectly compensated. (a)  $H = 20$ . (b)  $H = 10$ . (c)  $H = 5$ . (d)  $H = 3$ .

where the plus (minus) sign roughly corresponds to the global cooling (warming) of the upper layer. Figure 1.2 shows the change in the position of the surfacing line from that for the basic adiabatic case. It is confirmed that the cooling (warming) tends to expand (shrink) the outcrop as expected. This result is consistent with Pedlosky (1987) and Nurser and Williams (1990), who investigated the effect of local heating/cooling on the separating boundary current in Parsons' model.

## 1.4 Illustrative examples

### 1.4.1 Finite-depth effect on Parsons' model

The first example concerns the case when the lower layer is assumed to be in motion unless otherwise it outcrops. That is, the solution is given by

$$\psi_1 = \psi_s \equiv \frac{\lambda}{\beta} (1-x) \tau^x, \quad (1.60)$$

$$h_1^2 = h_s^2 \equiv h_c^2 - 2\lambda \left( \tau^x - \frac{f}{\beta} \tau_y^x \right) (1-x) \quad (1.61)$$

in the compensated region [cf. (1.4) and (1.5)] and

$$\psi_1 = 0, \quad h_1 = 0 \quad (1.62)$$

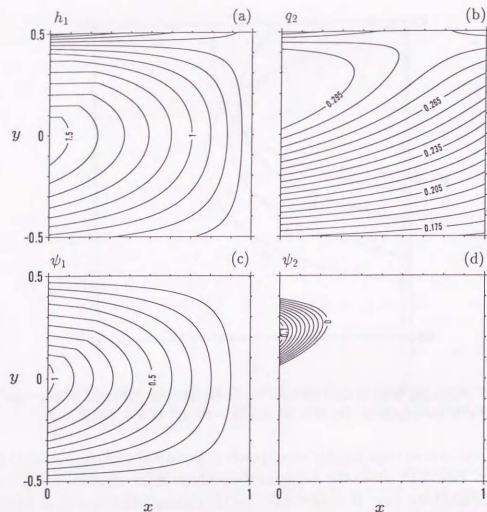


Figure 1.4. Solutions for (a)  $h_1$ , (b)  $q_2$ , (c)  $\psi_1$ , (d)  $\psi_2$  when the compensated region and the pool of uniform potential vorticity whose value is  $Q_0 = 1.2$  are separated by the "outermost closed geostrophic contour." The total depth is  $H = 5$ . Contour intervals are (a) 0.1, (b) 0.0075, (c) 0.1, (d) 0.01, respectively.

in the outcrop. We must replace the double-valued part of this solution by a suitable front, i.e., a surfacing line  $x = X_0(y)$ . Applying (1.60)–(1.62) to the jump condition (1.27), we have

$$\frac{h_s^2}{2} - \frac{h_s^3}{3H} - f\psi_s = 0 \quad \text{on } x = X_0(y), \quad (1.63)$$

hence the surfacing line is represented by

$$\frac{h_c^2}{2} - \lambda(1-x)\tau^x - \frac{1}{3H} \left[ h_c^2 - 2\lambda \left( \tau^x - \frac{f}{\beta} \tau_y^x \right) (1-x) \right]^{3/2} = 0. \quad (1.64)$$

Figure 1.3 illustrates some surfacing lines for different values of  $H$  calculated numerically using (1.64). The value of  $h_c$  for each case is chosen so that the total volume of the upper layer is unity under the assumption that the outcrop lies west of the surfacing

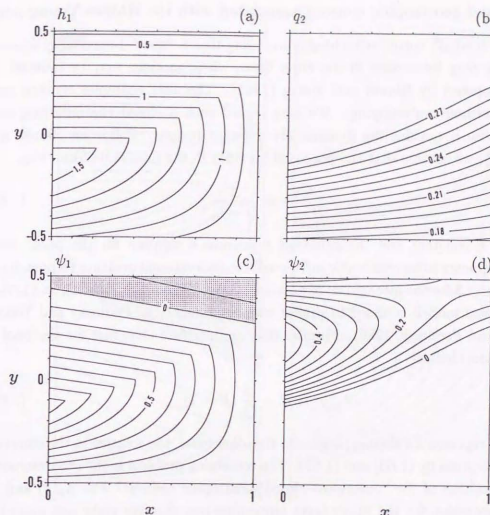


Figure 1.5. As in Fig. 1.4 but for  $Q_0 = 1.1$ . In (c) the region of negative values is shaded. Contour intervals are (a) 0.1, (b) 0.0075, (c) 0.1, (d) 0.05, respectively.

line. For  $H = 20$ , the configuration of the surfacing line is in good qualitative agreement with that for the reduced gravity model as expected. As  $H$  decreases, the outcrop shifts southward and even be detached from the northern boundary. Kamenkovich and Reznik (1972) carried out perturbation analysis of two-layer planetary geostrophic equations similar to (1.6)–(1.7) in order to obtain asymptotic solutions in powers of  $1/H$ . They correctly predicted the northwestward deflection of the surfacing line near the northern boundary. We note that (1.64) is *exact* for any  $H$  provided that the submerged portion of the lower layer is completely compensated, although compensation may be imperfect in reality when  $H$  is small.



#### 1.4.2 Closed geostrophic contour associated with the Rhines-Young pool

When  $H$  is small, vortex stretching is so strong that a "pool" bounded by a closed characteristic may be created in the lower layer, where motions may be induced, as originally proposed by Rhines and Young (1982). The next examples concern such a situation without outcropping. We may regard such a closed characteristic as a "front" because it divides the dynamically different regions. Following Rhines and Young (1982), we assume that the potential vorticity in the pool is uniform, viz.,

$$q_p \equiv \frac{Q_0}{H-1} = \frac{f}{H-h_p}, \quad (1.65)$$

where  $Q_0$  is a constant and the subscript  $p$  denotes a solution for the pool. This assumption appears to be reasonable in view of the observational evidence (Appendix 2; see also Chapter 3 for the mechanism of potential vorticity homogenization), and in fact some theoretical models resorted to similar simplifications (e.g., Pedlosky and Young, 1983; Cessi and Pedlosky, 1986). From (1.65), the interface structure for the pool is immediately decided as

$$h_1 = h_p(y) \equiv H - \frac{f}{Q_0}(H-1), \quad (1.66)$$

which simply represents a sloping plane. On the other hand, the solution in the compensated region is given by (1.60) and (1.61). The remaining problem is then to determine the correct position of the "outermost closed geostrophic contour"  $x = X_p(y)$  and to derive the expression for the upper-layer streamfunction  $\psi_p$ . We make one more assumption, which may be acceptable, that  $\psi_2 = 0$  along the front. Because of these assumptions, we need not specify the functional relationship between  $\psi_2$  and  $q_2$  as in (1.33), so that the jump condition (1.27) is simplified to

$$\frac{h_p^2}{2} - \frac{h_p^3}{3H} = \frac{h_s^2}{2} - \frac{h_s^3}{3H} \quad \text{on } x = X_p(y). \quad (1.67)$$

On substituting (1.66) and (1.61) into (1.67), the location of the front can be determined numerically. Provided  $X_p(y)$  is known,  $\psi_p$  can be calculated from (1.22) as

$$f\psi_p = \frac{h_p^2}{2} - \frac{h_p^3}{3H} - \left( \frac{h_s^2}{2} - \frac{h_s^3}{3H} - f\psi_s \right)_{x=X_p} + \frac{\lambda}{H} \left( \tau^x - \frac{f}{\beta} \tau^y \right) (x - X_p) h_p - \lambda (x - X_p) \tau^x, \quad (1.68)$$

and  $\psi_2 = \psi_s - \psi_p$  in the pool.

Figure 1.4 shows the solutions for  $H = 5$  and  $Q_0 = 1.2$ . The magnitude of the wind is one-third of that used for the previous examples. The pool is confined to a small region near the western boundary whose position and shape appear to be consistent with our knowledge from the unventilated thermocline theory. The volume

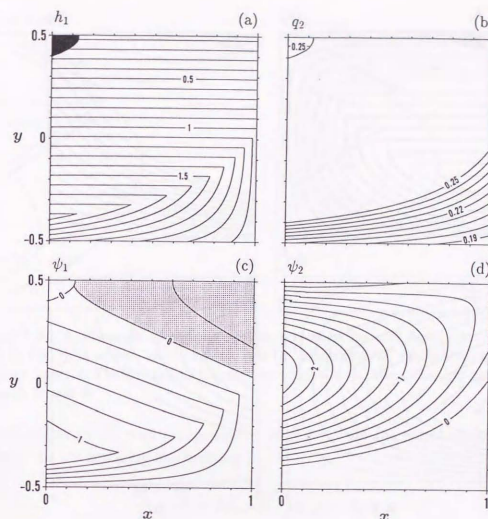


Figure 1.6. Solutions for  $H = 5$  and  $Q_0 = 1.03$  when the three different dynamical regions are separated by fronts. In (a) the black region denotes the outcrop. In (c) the region of negative values is shaded. Contour intervals are (a) 0.1, (b) 0.0075, (c) 0.2, (d) 0.2, respectively.

transport in the lower layer is found to be much smaller than that in the upper layer. To confirm the sensitivity of the solution to  $Q_0$ , the case for  $Q_0 = 1.1$  is shown in Fig. 1.5. The pool region enlarges and even reaches the eastern boundary in  $y > 0.275$ , where  $\psi_p$  has been calculated from (1.68) taking  $X_p = 1$ . This is against the eastern boundary condition because the fluid can flow across the eastern boundary in  $y > 0.275$ ; an eastern boundary layer should be implicit to compensate for the discrepancy (cf. Schopp and Arhan, 1986). It is also found that the volume transport in the pool greatly increases. Intuitively, this is because  $h_p$  decreases as  $Q_0$  decreases so that the pool can be matched with  $h_s$  further to the east where  $h_s$  is small. This may be a gross qualitative explanation of the real oceanic phenomena, i.e., that the horizontal scale of the region of uniform potential vorticity observed in the North Pacific and in the North



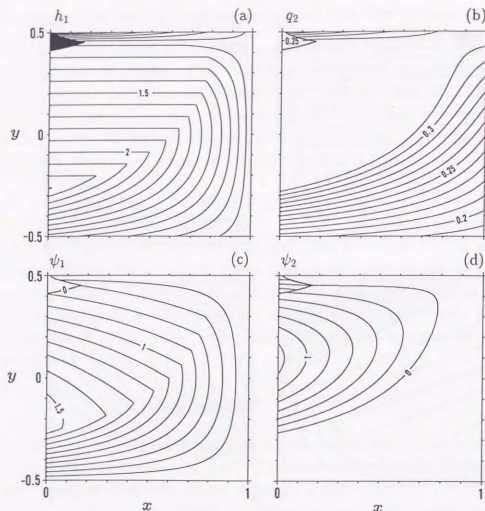


Figure 1.7. As in Fig. 1.6 but for  $Q_0 = 1.27$ . In (a) the black region denotes the outcrop. Contour intervals are (a) 0.1, (b) 0.01, (c) 0.2, (d) 0.2, respectively.

Atlantic may be comparable to the basin width. We expect, therefore, that if there is any mechanism such as the heat loss which reduces potential vorticity, the lateral scale of the pool increases substantially and a good portion of the volume transport is assigned in the pool.

#### 1.4.3 Coexistence of three dynamical regions

When the wind forcing strengthens in the situations described in the preceding examples, the northwestern part of the pool may outcrop. The following examples deal with the case when there are three dynamical regions, i.e., the compensated region, pool and outcrop. We assume again that the pool is filled with the uniform potential vorticity  $Q_0$  and that  $\psi_p = 0$  along the perimeter of the pool,  $x = X_p(y)$ . This front  $X_p$  can be determined by the jump condition (1.67) with (1.61) and (1.66), and the

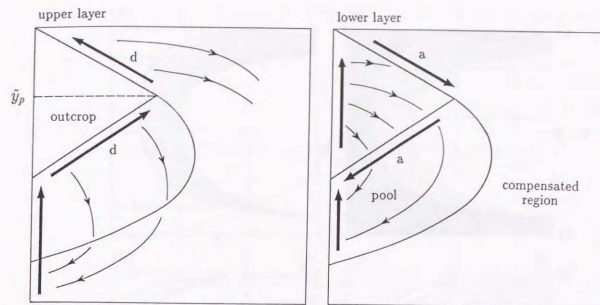


Figure 1.8. A schematic illustration of flow directions for each layer corresponding to Fig. 1.7. The thick arrows denote inferred jets (a: accelerated; d: decelerated) and western boundary currents. The thin arrows denote flows which enter or leave these jets corresponding to Figs. 1.7c and d.

streamfunction in the pool is represented by (1.68). On the other hand, the jump condition for the surfacing line becomes

$$\frac{h_p^2}{2} - \frac{h_p^3}{3H} - f\psi_p = 0 \quad \text{on } x = X_0(y), \quad (1.69)$$

into which (1.66) and (1.68) are to be substituted. Figure 1.6 shows the result for  $H = 5$ ,  $\lambda = 0.53$  and  $Q_0 = 1.03$ . Comparing this with Fig. 1.5, the pool expands meridionally and contains a considerable amount of transport. The upper gyre moves southward remarkably, so that even the signature of a cyclonic circulation can be seen in the northeastern part of the basin. The pool joins the eastern boundary, indicating the existence of an eastern boundary layer as in Fig. 1.5.

When  $Q_0$  increases to 1.27, the solution is changed as shown in Fig. 1.7. As confirmed in Figs. 1.4 and 1.5, the pool shrinks and is detached from the northern boundary, so that the outcrop comes into direct contact with the compensated region north of the pool. We note that the total volume is chosen to be 1.5 for this case only in order to highlight such features. Since the surfacing line satisfies (1.64), instead of (1.69), in  $y > \tilde{y}_p$  where  $\tilde{y}_p \equiv X_p^{-1}(x=0) = 0.45$ , the composite outcrop is wedged. Figure 1.8 shows schematic jets in each layer inferred from Fig. 1.7. In the upper layer, the northeastward interior jet smooths out the discontinuities between the outcrop and the pool in  $y < \tilde{y}_p$ , followed by the northwestward interior jet between the outcrop and the compensated region in  $y > \tilde{y}_p$ . These jets always supply fluids to the east and hence

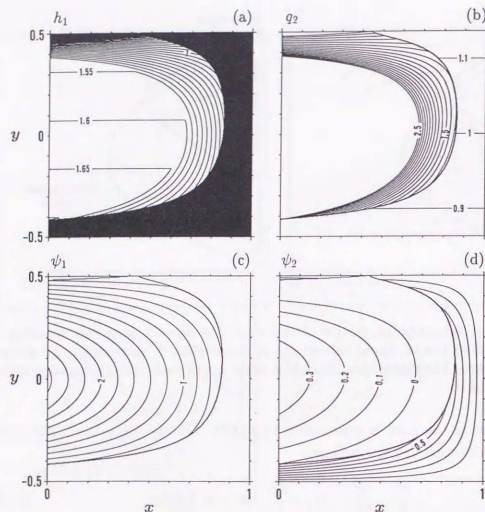


Figure 1.9. As in Fig. 1.6 but for  $H = 2$  and  $Q_0 = 2.6$ . In (a) the black region denotes the outcrop. Contour intervals are (a) 0.05, (b) 0.1, (c) 0.2, (d) 0.1, respectively.

should be decelerated. The jet system for the lower layer is easily predicted using the Sverdrup constraint. The southeastward interior jet turns southwestward at  $y = y_p$ , combines with the western boundary current carrying the pool water, and continues to flow northward along the western boundary in the outcrop carrying the full Sverdrup transport.

In the first examples (Section 1.3.1), we have considered that the outcrop lies west of the surfacing line, but this choice is arbitrary. Suppose otherwise that the outcrop entirely surrounds the compensated region which further contains the unventilated pool of uniform potential vorticity. The surfacing line can be determined in the same way as in Section 1.3.1, and the result is just (1.64). The eastern boundary condition (1.12) is relevant to the compensated region west of the outcrop. On the other hand, the inner front is determined by the jump condition (1.67). Figure 1.9 shows the result for  $H = 2$ ,  $\lambda = 0.53$  and  $Q_0 = 2.6$ . It is found that the "ventilated" circulation, though

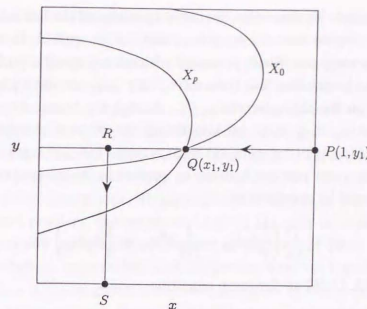


Figure 1.10. Construction of solutions when two fronts intersect.

highly exaggerated, encircles the basin and plunges into the western boundary and that the northwestern part of the outcrop is spontaneous. Since the compensated region separates the outcrop and the pool, the  $\psi_2$ -field is splitted into the outer ventilated and inner unventilated circulations. The overall configuration of the flow fields are in qualitative agreement with that obtained from the previous ventilated thermocline theories (Luyten et al, 1983; Pedlosky and Young, 1983) regardless of the different approaches. However, our solution differs fundamentally from the latter theoretical models in that the jump discontinuities are incorporated as intrinsic properties of the planetary geostrophic equations. The surfacing line is again indicative of jets in both layers, but these jets might be weaker than those in Fig. 1.8 because of the flow directions.

We note that when  $H$  is small and  $Q_0$  is large as in the case of Fig. 1.9, the jump condition (1.67) may be satisfied by two fronts, but we can conclude that only the outer front of these is the relevant one because  $h_s$  exceeds the total depth near the inner front. This provides another interpretation of why the lower layer cannot be compensated in the western part of the basin when  $H$  is small.

#### 1.4.4 Intersecting fronts

There is no trouble when the inner front is contained in the outer front as shown in Fig. 1.9. For more general cases, however, the possibility may arise that two fronts,  $x = X_0(y)$  and  $x = X_p(y)$ , intersect at point  $Q(x_1, y_1)$  as shown schematically in Fig. 1.10. In  $y > y_1$  solutions can be determined as previously, but the two fronts should be merged into a single front, say,  $x = X_1(y)$  in  $y < y_1$  which deviates the



outcrop and the pool. To determine the correct position of the latter front,  $\psi_p$  must be constructed in  $y < y_1$  so that the jump condition can be applied. Here, the basic idea and procedure to carry out this is presented without any specific worked solutions.

Suppose that the problem has been solved in  $y \geq y_1$  so that  $\psi_p$  has already been known as (1.68) on the characteristic  $y = y_1$  through the intersection point  $Q$ . Thus, we may calculate  $\psi_p$  in  $y < y_1$  by integrating the relevant characteristic equation southward from  $R(x_2, y_1)$  ( $0 \leq x_2 < x_1$ ) to  $S(x_2, y)$  ( $-1/2 \leq y < y_1$ ). However, (1.23) is useless for the present purpose because  $\psi_1$  appears in the integral on the right-hand side, hence it should be rewritten as

$$\psi_p = \int_{y_1}^y \left( \frac{1}{f} h_p h_{py} - \frac{1}{fH} h_p^2 h_{py} + \frac{1}{H} h_p \psi_{sy} \right) dy. \quad (1.70)$$

Applying this with (1.66) to the jump condition

$$\frac{h_p^2}{2} - \frac{h_p^3}{3H} - f \psi_p = 0, \quad (1.71)$$

we may determine the location of  $x = X_1(y)$ .

## 1.5 Conclusions

A formulation of Sverdrup dynamics is presented based on an inviscid/hyperbolic system of two-layer planetary geostrophic equations in place of the standard approach using the vorticity equation. The integral conservation laws of momentum, (1.19)–(1.21) and (1.25)–(1.23) are introduced to investigate solutions which may include jump discontinuities subject to the eastern boundary condition. An oceanic front such as a surfacing line and an outermost closed geostrophic contour is interpreted as a “shock” across which the jump conditions (1.27) and (1.26) derived from these integral constraints are satisfied. Furthermore, taking into account the Sverdrup constraint, the momentum equations are reformulated into a single conservation equation (1.28), although characteristics cannot generally be decided in advance because they may depend on the solution. These jump conditions may be used to determine suitable positions of fronts separating different dynamical regions if the interface structure for each subdomain is specified. Some examples in terms of the outcrop, the pool of uniform potential vorticity and the compensated region demonstrate the applicability of this approach. Of particular interest is the finite-depth version of Parsons’ model, in which case the exact solutions for the surfacing line are obtained in contrast to the asymptotic solutions derived by Kamenkovich and Reznik (1972).

When the total depth tends to infinity, all the key relations just obtained are reduced to the corresponding expressions for Parsons’ model. In this special case, a surfacing line is the only possible front and the lower-layer motion should be implicit in the

outcrop. It is found that a surfacing line in this special case can totally be determined provided that the external forcing and the boundary values are prescribed. The present inviscid/hyperbolic perspective eliminates the need for the semigeostrophic condition used in a similar study by Parsons (1969), Veronis (1973) and Huang and Flierl (1987).

In this chapter, the primary emphasis is directed toward jump discontinuities which have been ruled out in the major previous thermocline theories. A serious shortcoming of the present two-layer model, which is also in common with most of the previous theories, is that the streamlines are open in the west, so that the problem cannot be solved without further assumptions. To accomplish the closure as the two-layer extension of the Stommel problem, the equations (1.8)–(1.11) with interfacial and bottom frictions must be solved numerically. We intend to unravel the latter problem in the next chapter. We believe nevertheless that the present analysis together with the associated examples is a useful guide in the interpretation of the numerical solutions, because front-like structures on a discrete grid are more or less smeared by viscosities.

## References

- Anderson, D. L. T. and P. D. Killworth. 1979. Non-linear propagation of long Rossby waves. *Deep-Sea Res.* **26**, 1033–1050.
- Burger, A. P. 1958. Scale consideration of planetary motions of the atmosphere. *Tellus* **10**, 195–205.
- Cessi, P. and J. Pedlosky. 1986. On the role of topography in the ocean circulation. *J. Mar. Res.* **44**, 445–471.
- Charney, J. G. and G. R. Flierl. 1981. Oceanic analogues of large-scale atmospheric motions. In: *Evolution of Physical Oceanography* (B. A. Warren and C. Wunsch, eds.), pp. 504–548. The MIT Press, Cambridge and London.
- Cushman-Roisin, B., G. G. Sutyrin, and B. Taq. 1992. Two-layer geostrophic dynamics. Part I: Governing equations. *J. Phys. Oceanogr.* **22**, 117–127.
- Dewar, W. K. 1987. Planetary shock waves. *J. Phys. Oceanogr.* **17**, 470–482.
- Dewar, W. K. 1991. Arrested fronts. *J. Mar. Res.* **49**, 21–55.
- Huang, R. X. 1991. The three-dimensional structure of wind-driven gyres: Ventilation and subduction. *Rev. Geophys. (Suppl.)*, 590–609.
- Huang, R. X. and G. R. Flierl. 1987. Two-layer models for the thermocline and current structure in subtropical/subpolar gyres. *J. Phys. Oceanogr.* **17**, 872–884.

- Johnsson, J. A. and A. J. Willmott. 1981. An unsteady wind-driven ocean circulation model. *Dyn. Atmos. Oceans* **6**, 1-27.
- Kamenkovich, V. M. and G. M. Reznik. 1972. A contribution to the theory of stationary wind-driven currents in a two-layer liquid. *Izv. Acad. Sci. USSR Atmos. Oceanic Phys.* (English translation) **8**, 238-245.
- Luyten, J. R. and H. Stommel. 1986. Gyres driven by combined wind and buoyancy flux. *J. Phys. Oceanogr.* **16**, 1551-1560.
- Luyten, J. R., J. Pedlosky, and H. Stommel. 1983. The ventilated thermocline. *J. Phys. Oceanogr.* **13**, 292-309.
- Nursler, A. J. G. and R. G. Williams. 1990. Cooling Parsons' model of the separated Gulf Stream. *J. Phys. Oceanogr.* **20**, 1974-1979.
- Parsons, A. T. 1969. A two-layer model of Gulf Stream separation. *J. Fluid Mech.* **39**, 511-528.
- Pedlosky, J. 1987. On Parsons' model of the ocean circulation. *J. Phys. Oceanogr.* **17**, 1571-1582.
- Pedlosky, J. and W. R. Young. 1983. Ventilation, potential-vorticity homogenization and the structure of the ocean circulation. *J. Phys. Oceanogr.* **13**, 2020-2037.
- Phillips, N. A. 1963. Geostrophic motion. *Rev. Geophys.* **1**, 123-176.
- Rhines, P. B. and W. R. Young. 1982. A theory of the wind-driven circulation I. Mid-ocean gyres. *J. Mar. Res.* **40** (Suppl.), 559-596.
- Robinson, A. and H. Stommel. 1959. The oceanic thermocline and the associated thermohaline circulation. *Tellus* **11**, 295-308.
- Sakamoto, T. 1998. On discontinuities in the Sverdrup interior. *J. Phys. Oceanogr.* accepted.
- Salmon, R. 1992. A two-layer Gulf Stream over a continental slope. *J. Mar. Res.* **50**, 341-365.
- Schopp, R. and M. Arhan. 1986. A ventilated middepth circulation model for the eastern North Atlantic. *J. Phys. Oceanogr.* **16**, 344-357.
- Sverdrup, H. U. 1947. Wind-driven currents in baroclinic ocean: With applications to the equatorial currents of the eastern Pacific. *Proc. Nat. Acad. Sci.* **33**, 318-326.
- Veronis, G. 1973. Model of world ocean circulation: I. Wind-driven, two-layer. *J. Mar. Res.* **31**, 228-288.
- Welander, P. 1959. An advective model of the ocean thermocline. *Tellus* **11**, 309-318.
- Welander, P. 1966. A two-layer frictional model of wind-driven motion in a rectangular oceanic basin. *Tellus* **18**, 54-62.

- Williams, G. P. and T. Yamagata. 1984. Geostrophic regimes, intermediate solitary vortices and Jovian eddies. *J. Atmos. Sci.* **41**, 453-478.
- Willmott, A. J. 1985. A note on the steepening of long Rossby waves. *Deep-Sea Res.* **32**, 613-617.
- Whitham, G. B. 1974. *Linear and Nonlinear Waves*, Wiley, New York.
- Yamagata, T. 1982. On nonlinear planetary waves: A class of solutions missed by the traditional quasi-geostrophic approximation. *J. Oceanogr. Soc. Japan* **38**, 236-244.



## Chapter 2

### The two-layer Stommel problem with outcropping: A numerical approach

#### 2.1 Introduction

A rectangular basin containing two immiscible layers with a material interface has been used as the simplest baroclinic model for the large-scale ocean circulation. However, steady, wind-driven, planetary geostrophic motions in such a model are still unknown even qualitatively, except for several extreme cases including reduced gravity models. Historically, since Stommel (1948), ocean circulation models have been developed either by adding the inertial or topographic effect (Veronis, 1966; Holland, 1967), or by greatly increasing vertical resolution (Bryan, 1969). This is surprising from the conceptual point of view. In this chapter, we solve simple two-layer planetary geostrophic equations numerically for the subtropical gyre including an outcrop. The primary purpose is to contribute to geophysical fluid dynamics, that is, to fill a gap in a classical view of conventional layer models originated in Stommel (1948), rather than to apply immediately to real oceanic phenomena, except for some restricted cases. Since the present problem is well-posed, numerical results can nevertheless be used to confirm some of the previous analytical models for the wind-driven ocean circulation and to associate them with each other within the framework of the present basic model. We summarize below some fruitful analytical results concerning layer models, which have been developed in the past 30 years. We also point out the well-known limitations of these theoretical models which in fact strongly stimulate the present study.

The Stommel problem can be solved in closed form as a combination of a Sverdrup interior and a frictional western boundary layer. However, finding a general solution of two-layer equations is a difficult matter, even under the quasigeostrophic approximation (cf. Ierley and Young, 1983; see also Chapter 3). The problem becomes complicated further when considering  $O(1)$  interface displacement which is represented suitably by planetary geostrophic dynamics. For instance, Parsons (1969) assumed a completely compensated lower layer and succeeded in obtaining an interior layer associated with an outcrop in addition to the familiar western boundary layer. However, the Sverdrup

relation does not entirely hold over the basin because of the 1.5-layer representation. Welander (1966) treated the case when the lower layer is not compensated near the western boundary. He simplified the two-layer equations by assuming that the lower layer is very deep and, on the other hand, that bottom friction is much larger than interfacial friction (see also Section 2.2). Then, the total vorticity balance is assured in the entire domain, and, at the same time, the interaction terms become negligible in the western boundary layer. This simplification leads to a recirculating boundary current in the lower layer. Kamenkovich and Reznik (1972) combined both Parsons' and Welander's approaches under the Sverdrup constraint, but their analytical solutions have not still been verified numerically.

There are at present two more classes of theoretical models for the wind-driven ocean circulation which are quite different from the Parsons-type models. In the ventilated thermocline theory (Luyten et al., 1983), a water particle is driven directly by winds at the outcrop and is submerged afterwards on the isopycnal surface to conserve its potential vorticity. The other theory, which is sometimes called unventilated thermocline theory, considers strong vortex stretching that may form a closed characteristic in an underlying layer within which a particle can recirculate freely without outcropping (Rhines and Young, 1982). Both inviscid theories succeeded in circumventing the difficulties involved in the classical similarity approach such as Welander (1971). However, to determine motions uniquely, a surfacing line must be prescribed in the ventilated thermocline model while a global condition is required in the unventilated thermocline model; the frictional western boundary current must be excluded. This is the reason why it is not easy to apply these modern theories to the real ocean (see Pedlosky, 1990).

Therefore, we need to include a thin lower layer, outcropping and viscosity simultaneously for further development of the thermocline theory; the two-layer version of the Stommel model satisfies these requirements. We thus construct such a model based on the two-layer planetary geostrophic equations in which the viscous effects are parameterized by interfacial and bottom frictions. Outcropping is allowed so that the lower layer may be driven directly by winds. Our model is also regarded as the planetary-geostrophic version of Ierley and Young (1983). In this sense, the present model should be the starting point for investigating the stratified, large-scale ocean circulation before including any other physical processes such as the inertial and thermohaline effects.

A numerical approach is adopted to say a great deal about the overall structure of solutions of the two-layer equations. Numerical calculations are conducted for a wide range of the mean lower-layer thickness; we expect that the results widely cover the above-mentioned theoretical models but with the frictions. Extensive analysis of each solution is beyond the scope of the present work. Technically, the Total Variation Diminishing (TVD) method is used to overcome the numerical difficulties arising from

layer outcropping. Our numerical calculations may be compared with those using the older FCT and related algorithms applied routinely to the *reduced gravity* models (Huang, 1986; Huang, 1987; Bogue et al., 1986; Sun et al., 1993; Chassignet and Block, 1993; Cloke and Cullen, 1994; Chassignet et al., 1995). It should be emphasized, however, that an attempt is made for the first time to apply the high-resolution scheme to the *purely two-layer* model. From the present calculations, some new physical aspects which have not been found in the previous numerical studies just cited will be proposed; it will be shown qualitatively, for example, how the ventilated circulation matches with the unventilated recirculating gyre in the present adiabatic single-gyre model. The effects of the western boundary layer to the ventilated circulation will also be shown.

## 2.2 Model equations

The model ocean is a two-layer fluid contained in a square basin,  $0 \leq x \leq L$ ,  $-L/2 \leq y \leq L/2$ , where  $(x, y)$  are the (eastward, northward) coordinates. Each layer has the mean thickness  $D_n$  ( $n = 1, 2$ ) and the total depth is constant. We assume a  $\beta$ -plane on which the central latitude is taken as a reference latitude. Since we are concerned with a large-scale ocean circulation described by planetary geostrophic dynamics, we introduce hydrostatic, Boussinesq and rigid-lid approximations as usual. Then, the governing equations are

$$-fv_1 = -\frac{1}{\rho_0}p_x + \frac{\tau^x}{\rho_0 h_1} - \frac{R}{h_1}(u_1 - u_2), \quad (2.1)$$

$$fu_1 = -\frac{1}{\rho_0}p_y + \frac{\tau^y}{\rho_0 h_1} - \frac{R}{h_1}(v_1 - v_2), \quad (2.2)$$

$$h_{1t} + (u_1 h_1)_x + (v_1 h_1)_y = 0, \quad (2.3)$$

for the upper layer and

$$-fv_2 = -\frac{1}{\rho_0}p_x + g'h_{1x} + \frac{R}{h_2}(u_1 - u_2) - \frac{K}{h_2}u_2, \quad (2.4)$$

$$fu_2 = -\frac{1}{\rho_0}p_y + g'h_{1y} + \frac{R}{h_2}(v_1 - v_2) - \frac{K}{h_2}v_2, \quad (2.5)$$

$$h_{2t} + (u_2 h_2)_x + (v_2 h_2)_y = 0, \quad (2.6)$$

for the lower layer, respectively. Here,  $(u_n, v_n)$  is the velocity of the  $n$ th layer,  $h_n$  is the  $n$ th-layer thickness,  $p$  is the depth-independent pressure,  $f = f_0 + \beta_0 y$  is the Coriolis parameter with its constant latitudinal gradient  $\beta_0$ ,  $(\tau^x, \tau^y)$  is the (zonal, meridional) wind stress introduced as a body force,  $\rho_0$  is the reference density, and  $g'$  is the reduced gravity. Vertical transfer of momentum is introduced as interfacial and bottom frictions which are parameterized in the form of a simple drag with dimensional coefficients  $R$



and  $K$ , respectively. The boundary condition is that there is no normal velocity on the solid walls, i.e.,

$$\begin{aligned} u_n &= 0 \quad \text{on the meridional boundaries,} \\ v_n &= 0 \quad \text{on the zonal boundaries.} \end{aligned} \quad (2.7)$$

We nondimensionalize the above equations by scaling as follows:  $(x, y)$  by  $L, h_n$  by  $D_1, f$  by  $f_0, (u_n, v_n)$  by  $u_0 \equiv g'D_1/f_0L, t$  by  $T \equiv L/u_0$  and  $(\tau^x, \tau^y)$  by  $\tau_0$ . Then, we have dimensionless equations corresponding to (2.1)–(2.6):

$$-fv_1 = -p_x + \lambda \frac{\tau^x}{h_1} - \frac{\nu}{h_1}(u_1 - u_2), \quad (2.8)$$

$$fu_1 = -p_y + \lambda \frac{\tau^y}{h_1} - \frac{\nu}{h_1}(v_1 - v_2), \quad (2.9)$$

$$h_{11} + (u_1 h_1)_x + (v_1 h_1)_y = 0, \quad (2.10)$$

$$-fv_2 = -(p_x - h_{1x}) + \frac{\nu}{h_2}(u_1 - u_2) - \delta \frac{u_2}{h_2}, \quad (2.11)$$

$$fu_2 = -(p_y - h_{1y}) + \frac{\nu}{h_2}(v_1 - v_2) - \delta \frac{v_2}{h_2}, \quad (2.12)$$

$$h_{21} + (u_2 h_2)_x + (v_2 h_2)_y = 0. \quad (2.13)$$

These equations are solved numerically in the domain  $0 \leq x \leq 1, -0.5 \leq y \leq 0.5$  subject to the boundary condition (2.7). The nondimensional parameters are defined as  $\beta = \beta_0 L/f_0, \nu = R/(f_0 D_1), \delta = K/(f_0 D_1)$  and  $\lambda = \tau_0 g' D_1^2/(\rho_0 g' D_1^2)$ . The wind forcing is assumed to be zonal and stationary and to model winds of the subtropics:

$$\tau^x = \sin \pi y, \quad \tau^y = 0. \quad (2.14)$$

The total transport streamfunction  $\Psi$  can be defined at any time from the sum of the continuity equations, (2.10) and (2.13), as

$$U_1 + U_2 = -\Psi_y, \quad V_1 + V_2 = \Psi_x, \quad (2.15)$$

where  $(U_n, V_n) = (u_n h_n, v_n h_n)$  is the volume transport. On the other hand, the streamfunction for each layer,  $\psi_n$ , can be defined only in a steady state. As introduced in Parsons' model, integration of (2.10) or (2.13) over the whole domain yields an important constraint

$$\iint h_n dx dy = \text{const.}, \quad (2.16)$$

that is, the total volume of each layer should be prescribed.

The momentum equations (2.8), (2.9), (2.11) and (2.12) can be solved for each velocity component as follows:

$$\gamma U_1 = A_1 \tilde{G}_1^x + A_2 \tilde{G}_1^y + A_3 \tilde{G}_2^x + A_4 \tilde{G}_2^y, \quad (2.17)$$

$$\gamma V_1 = -A_1 \tilde{G}_1^x + A_2 \tilde{G}_1^y + A_3 \tilde{G}_2^x - A_4 \tilde{G}_2^y, \quad (2.18)$$

$$\gamma U_2 = A_5 \tilde{G}_2^x + A_6 \tilde{G}_2^y + A_7 \tilde{G}_3^x + A_8 \tilde{G}_3^y, \quad (2.19)$$

$$\gamma V_2 = -A_5 \tilde{G}_2^x + A_6 \tilde{G}_2^y + A_7 \tilde{G}_3^x - A_8 \tilde{G}_3^y, \quad (2.20)$$

where the variables with a tilde mean that

$$(\tilde{\phantom{x}}) = \frac{(\phantom{x})}{f}. \quad (2.21)$$

Each  $G$  denotes the right-hand side of the momentum equation without the friction terms:

$$\begin{pmatrix} G_1^x \\ G_1^y \\ G_2^x \\ G_2^y \end{pmatrix} = \begin{pmatrix} -h_1 p_x + \lambda \tau^x \\ -h_1 p_y + \lambda \tau^y \\ -h_2 p_x + h_2 h_{1x} \\ -h_2 p_y + h_2 h_{1y} \end{pmatrix}. \quad (2.22)$$

The coefficients in (2.17)–(2.20) are defined as

$$\gamma = \frac{h_1^2 h_2^2}{H^2} + \tilde{\nu}^2 + \frac{h_1^2}{H^2} (2\tilde{\nu} \tilde{\delta} + \tilde{\delta}^2) + \frac{1}{H^2} \tilde{\nu}^2 \tilde{\delta}^2, \quad (2.23)$$

$$A_1 = \frac{h_1^2 h_2^2}{H^2} + \frac{h_1 h_2}{H^2} \tilde{\nu}^2 + \frac{h_1^2}{H^2} (\tilde{\nu} + \tilde{\delta})^2, \quad (2.24)$$

$$A_2 = \frac{h_1 h_2^2}{H^2} \tilde{\nu} + \frac{h_1}{H^2} \tilde{\nu} \tilde{\delta} (\tilde{\nu} + \tilde{\delta}), \quad (2.25)$$

$$A_3 = -\frac{h_1^2 h_2}{H^2} \tilde{\nu} + \frac{h_1}{H^2} \tilde{\nu}^2 \tilde{\delta}, \quad (2.26)$$

$$A_4 = \frac{h_1}{H} \tilde{\nu}^2 + \frac{h_1^2}{H^2} \tilde{\nu} \tilde{\delta}, \quad (2.27)$$

$$A_5 = \frac{h_1^2 h_2^2}{H^2} + \frac{h_2}{H} \tilde{\nu}^2, \quad (2.28)$$

$$A_6 = -\frac{h_1 h_2^2}{H^2} \tilde{\nu} + \frac{h_2}{H^2} \tilde{\nu}^2 \tilde{\delta}, \quad (2.29)$$

$$A_7 = \frac{h_1^2 h_2}{H^2} (\tilde{\nu} + \tilde{\delta}) + \frac{h_2}{H^2} \tilde{\nu}^2 \tilde{\delta}, \quad (2.30)$$

$$A_8 = \frac{h_2}{H} \tilde{\nu}^2 + \frac{h_1 h_2}{H^2} \tilde{\nu} \tilde{\delta}, \quad (2.31)$$

where  $H = h_1 + h_2$  is the total depth. Of course, when  $h_1 = 0$ , (2.17)–(2.20) are reduced to the equations for the single-layer model. A slightly modified version of (2.17)–(2.31) will be used in the later numerical calculations.

We note here a further approximation to the above expressions for the steady problem. Neglecting the terms higher than  $O(\tilde{\nu})$  and  $O(\tilde{\delta})$  in (2.23)–(2.31) leads to

$$-f \psi_{1x} = -h_1 p_x + \lambda \tau^x + \frac{\nu}{f} h_{1y}, \quad (2.32)$$

$$-f \psi_{1y} = -h_1 p_y - \frac{\nu}{f} \left( h_{1x} - \frac{\lambda \tau^x}{h_1} \right), \quad (2.33)$$

$$-f \psi_{2x} = -h_2 (p_x - h_{1x}) - \frac{\nu}{f} h_{1y} + \frac{\delta}{f} (p_y - h_{1y}), \quad (2.34)$$

$$-f \psi_{2y} = -h_2 (p_y - h_{1y}) + \frac{\nu}{f} \left( h_{1x} - \frac{\lambda \tau^x}{h_1} \right) - \frac{\delta}{f} (p_x - h_{1x}). \quad (2.35)$$

Welander (1966), Kamenkovich and Reznik (1972) and Jarvis and Veronis (1994) used essentially the same equations as (2.32)–(2.35). Physically, the above simplification corresponds to the geostrophic approximation to the friction terms. Welander (1966) considered the case when  $h_1 = O(1)$ ,  $(\nu, \delta) \rightarrow 0$ ,  $\alpha \rightarrow \infty$  and  $\alpha\nu/\delta = O(1)$ . Kamenkovich and Reznik (1972) further treated the case when  $h_1 = O(\epsilon)$  (assuming  $\nu \sim \delta \equiv \epsilon$ ) adjacent to an outcrop. From the careful ordering estimation, the latter authors found an  $O(\epsilon^2)$  viscous interior layer and constructed the first-term approximation for it. However, it is found from (2.23)–(2.31) that several terms which is quadratic in  $\bar{\nu}$  cannot be neglected if  $h_1 = O(\epsilon)$ . In particular, if  $h_1 = 0$ , the main balance is totally different from (2.32)–(2.35). The present numerical experiment may deal with any transition region which is not described correctly by (2.32)–(2.35).

### 2.3 Numerical method

Numerical calculations are carried out on a regularly spaced, staggered B-grid (see Fig. A.1 in Appendix to Chapter 2). Each grid cell is centered on a  $h$  point and the points of  $(u, v)$  are arranged at cell corners. The Coriolis and wind-forcing terms are located at the  $(u, v)$  points. All coastal boundaries coincide with cell boundaries so that the no-normal-flow condition (2.7) can be imposed explicitly. The streamfunction  $\Psi$  is placed both at the  $h$  point and on the coastal boundaries to impose the boundary condition [see (2.38) ff.].

We are concerned with solving the initial value problem (2.10) with (2.17) to (2.20). The initial condition is the state at rest, so that the constant of (2.16) for the upper layer is set to be 1. The explicit symmetric TVD scheme (Yee, 1987) is applied to the numerical fluxes for the continuity equation (2.10) to suppress numerical oscillations associated with large gradients of  $h_1$  (cf. Appendix to Chapter 2). The finite difference form of the spatial derivative of (2.10) is presented in Appendix to Chapter 2.<sup>1</sup> For time integration, the two-stage Runge-Kutta method is adopted to preserve the second-order time accuracy; time stepping is continued until a steady state is reached.

We follow Holland and Lin (1975) to determine the pressure gradient  $\nabla p$  in (2.22). The diagnostic equation for  $\Psi$  is obtained as follows. Summing up the upper- and lower-layer equations gives

$$-f\Psi_x = -Hp_x + h_2h_{1x} + \lambda\tau^x - \frac{\delta}{h_2}U_2, \quad (2.36)$$

$$-f\Psi_y = -Hp_y + h_2h_{1y} + \lambda\tau^y - \frac{\delta}{h_2}V_2. \quad (2.37)$$

<sup>1</sup>In Appendix to Chapter 2, we also demonstrate various flux and slope limiter schemes using a 1.5-layer planetary geostrophic model.

Table 2.1. Eleven cases of the present numerical experiment

Regime	Case	H	$\lambda$	$\nu$	$\delta$
Deep	1	20	0.53	0.01	0.06
	2	10	0.53	0.01	0.03
Moderate	3	5	0.53	0.01	0.013
	4	4	0.53	0.01	0.01
Shallow	5	3	0.53	0.01	0.008
	6	2	0.53	0.01	0.005
	7	2	0.7	0.005	0.005
	8	2	0.35	0.005	0.005
	9	2	0.53	0.005	0.005
	10	2	0.53	0.005	0.01
	11	2	0.53	0.005	0.015

To get an elliptic equation with respect to  $\Psi$ , we eliminate  $U_2$  and  $V_2$  from the above equations using (2.15). Then, taking the curl of the resulting equations yields the following barotropic vorticity equation:

$$\nabla \cdot \left( \frac{\delta}{h_2} \nabla \Psi \right) + J(\Psi, f) = \lambda(\tau_x^y - \tau_y^x) + \delta \left[ \left( \frac{V_1}{h_2} \right)_x - \left( \frac{U_1}{h_2} \right)_y \right]. \quad (2.38)$$

Eq. (2.38) is solved using the SOR method with the boundary condition  $\Psi = 0$ . We note that the coefficient of the highest-order term is a function of  $x$ ,  $y$  and  $t$  and hence must be calculated at every time step, in contrast to a similar model but with Rayleigh damping (cf. Sakamoto and Yamagata, 1996).

Provided the updated values of  $h_1$  and  $\nabla p$  are known, the velocity components are immediately obtained from (2.17)–(2.31). Of course, (2.17)–(2.31) must be changed in accordance with the above derivation (not shown).

### 2.4 Results

The reference parameters are chosen to be  $L = 2000$  km,  $f_0 = 7.3 \times 10^{-5} \text{ s}^{-1}$  (i.e., the central latitude is  $30^\circ\text{N}$ ),  $\beta_0 = 2.0 \times 10^{-11} \text{ m}^{-1}\text{s}^{-1}$ ,  $D_1 = 200$  m,  $g' = 0.01 \text{ m s}^{-2}$ ,  $\rho_0 = 1000 \text{ kg m}^{-3}$  and  $\tau_0 = 0.106 \text{ Nm}^{-2}$ . Then, the velocity scale  $u_0$  is  $1.37 \times 10^{-2} \text{ m s}^{-1}$ , giving the characteristic time scale  $T = 4.6$  years. The values of the nondimensional parameters are  $\beta = 0.55$  and  $\tau = 0.53$ . The main controlling parameter is the total depth  $H$  or, equivalently, the mean thickness ratio  $\alpha = D_2/D_1$  with  $D_1$  fixed. For



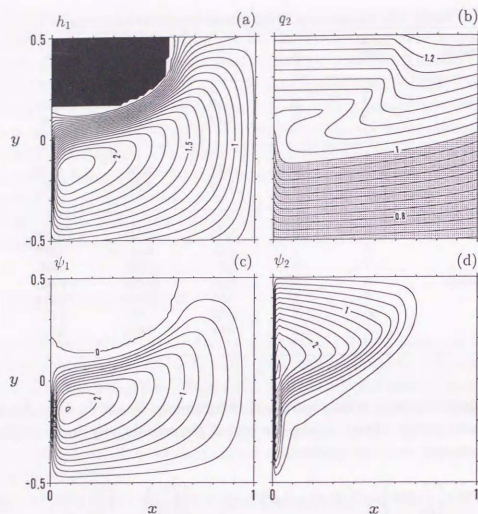


Figure 2.1. Steady-state solutions for Case 1. (a)  $h_1$ , (b)  $q_2$ , (c)  $\psi_1$ , (d)  $\psi_2$ . Contour intervals are (a) 0.1, (b) 0.025, (c) 0.2, (d) 0.2, respectively. The black region of  $h_1$  indicates the outcrop. The values of  $q_2$  less than 1 are shaded.

convenience, we classify the calculations in the present numerical experiment roughly into three regimes (Table 2.1). The *deep-ocean regime* corresponds to the cases when  $H \gg 1$  (or  $D_2/D_1 \gg 1$ ). The *shallow-ocean regime* corresponds to the cases when  $H \sim 1$  ( $D_2/D_1 \sim 1$ ). The *moderate or intermediate regime* includes the cases between these extreme regimes. For Cases 1 to 6, the interfacial friction coefficient  $\nu$  is fixed at 0.01, but the bottom friction coefficient  $\delta$  is varied so that the values of  $\delta/H$ , which measures the width of the western boundary layer, do not differ very much (Table 1). The shallow-ocean cases are examined further, because this particular regime has not been treated by the previous workers and hence is the most interesting theoretically. The grid resolution is  $64 \times 64$  for the first six cases and  $100 \times 100$  for the succeeding five cases, respectively.

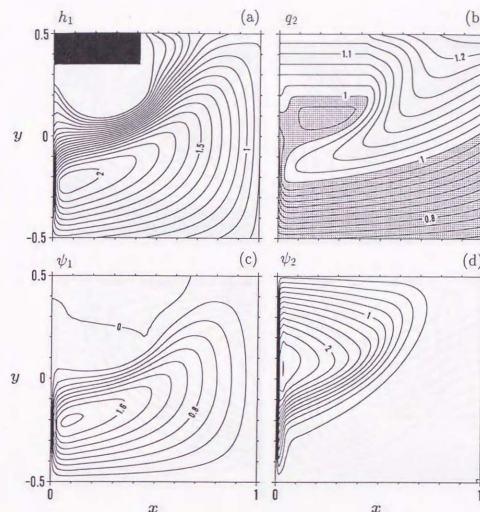


Figure 2.2. As in Fig. 2.1 but for Case 2. Contour intervals are (a) 0.1, (b) 0.025, (c) 0.2, (d) 0.2, respectively.

#### 2.4.1 Deep-ocean regime

Figure 2.1 shows the steady-state solutions for  $H = 20$ . The total depth of this case is comparable to the full depth of the ocean. We can see a sharp front along the perimeter of the northwest outcrop in the  $h_1$ -field (Fig. 2.1a) and its associated northeastward jet in the upper layer (Fig. 2.1c). The overall features are in good qualitative agreement with those of Parsons' solutions. On the other hand,  $\psi_2$  (Fig. 2.1d) consists of three dynamical components away from the western boundary: the Sverdrup flow, narrow southwestward countercurrent corresponding to the overlying jet and stagnant region. These regions can also be distinguished in the distribution of the lower-layer potential vorticity  $q_2 = f/h_2^2$ , where  $h_2^2 = (D_1/D_2)h_2$  (Fig. 2.1b). The total streamfunction  $\Psi$  (not shown) is consistent with the Sverdrup relation but slightly distorted along the interior jets. This distortion is probably due to the strong internal jet in which the

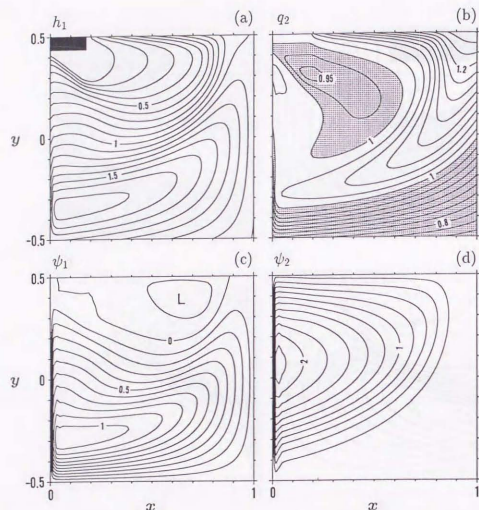


Figure 2.3. As in Fig. 2.1 but for Case 3. Contour intervals are (a) 0.1, (b) 0.025, (c) 0.1, (d) 0.2, respectively.

effect of bottom friction might not completely be neglected. Thus, the features of the Sverdrup interior in the numerical result is expected to approach those in the analytical model constructed by Kamenkovich and Reznik (1972) only asymptotically.

Figure 2.2 shows the solutions for  $H = 10$ . The outcrop shrinks northward, whereas a sharp interior layer is seen further south in  $h_1$ ,  $\psi_1$  and  $\psi_2$ . The upper layer is remarkably thin between the outcrop and the front. This may be partly due to a numerical artifact, but physically this "skin layer" may also be regarded as an effective outcrop in which the interfacial friction nearly balances with the wind forcing.<sup>2</sup> This portion in the  $h_1$ -field can be distinguished in the  $q_2$ -field as the domain of the latitude circles (Fig. 2.2b). The front for  $h_1$  is strongly bent and turns northwestward with increasing  $y$ , consistent with the prediction in Chapter 1. We are thus successful in

<sup>2</sup>In this regard, Jarvis and Veronis (1994) gave similar solutions without outcropping.

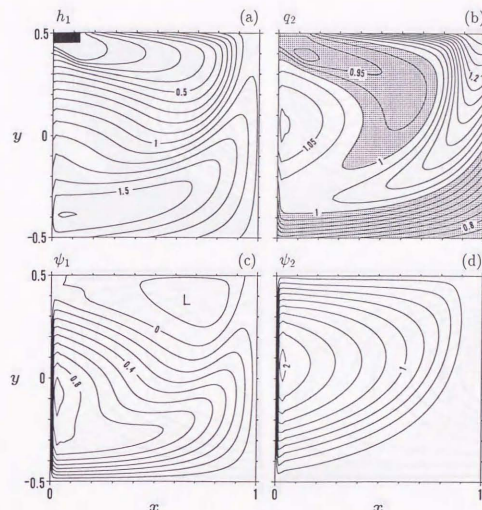


Figure 2.4. As in Fig. 2.1 but for Case 4. Contour intervals are (a) 0.1, (b) 0.025, (c) 0.1, (d) 0.2, respectively.

reproducing the finite-depth effect on Parsons' model numerically. It is also found that the interior layer of  $h_1$  is not sharp near the western coast. Presumably, this is due to the lower-layer motion rather than a numerical artifact, which will become clearer by comparing with the other cases presented later. Therefore, the analytical solutions obtained by Kamenkovich and Reznik (1972) capture the gross features of the frictional boundary layers, although the discrepancy associated with incomplete compensation is seen near the separation point.

#### 2.4.2 Intermediate regime

Figure 2.3 shows the solutions for  $H = 5$  while Fig. 2.4 shows the solutions for  $H = 4$ . The total depths of these cases may be comparable to the typical depths of the main thermocline associated with the major wind-driven gyre. The "bowl" of



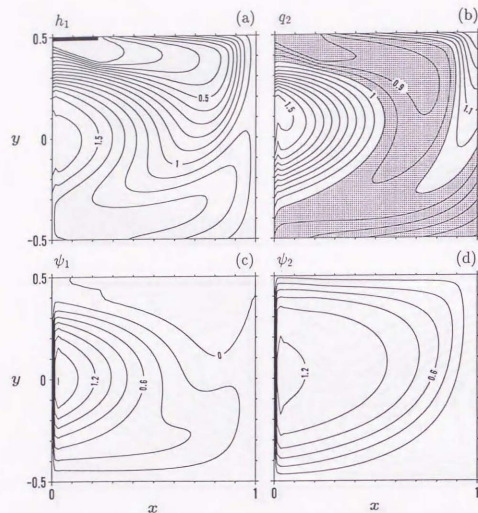


Figure 2.5. As in Fig. 2.1 but for Case 5. Contour intervals are (a) 0.1, (b) 0.05, (c) 0.2, (d) 0.2, respectively.

the subtropical gyre shifts southward, while the outcrop shrinks further northwestward (Figs. 2.3a and 2.4a). Accordingly, the meridional slope of  $h_1$  is greatly reduced and the  $h_1$ -contours are nearly parallel to the latitude circles in the western domain, although a front-like structure can still be noticed just south of the outcrop and along the northern boundary.<sup>3</sup>

The distribution of  $q_2$  (Figs. 2.3b and 2.4b) clearly shows the signature of ventilation. A tongue of low potential vorticity (the shaded area with the 0.95 contour in its center) emanates from the northwest outcrop, extends southeastward along the streamlines and ceases before the western coast is reached. It seems that this is a characteristic feature of the planetary geostrophic model regardless of the existence of outcropping [see Fig. 3.12; see also some interesting results of Jarvis and Veronis

<sup>3</sup>This is partly due to the slightly diffusive character of Yee's symmetric scheme (cf. Appendix to Chapter 2). See also the FCT result in Fig. 2.13.

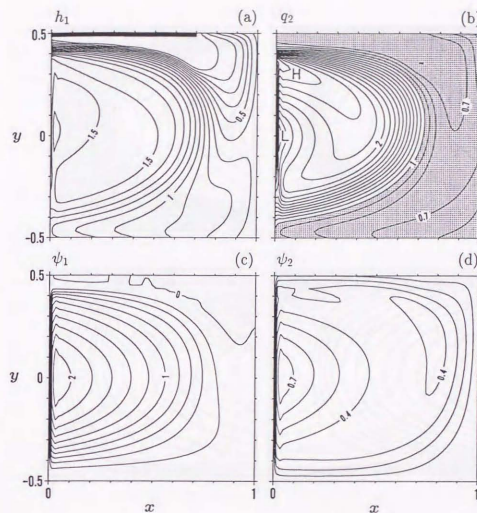


Figure 2.6. As in Fig. 2.1 but for Case 6. Contour intervals are (a) 0.1, (b) 0.1, (c) 0.2, (d) 0.1, respectively.

(1994)). We note, however, that an isolated minimum of  $q_2$  is not created with a corresponding quasigeostrophic model as will be shown in Chapter 3. It is also noticed from Figs. 2.3b and 2.4b that the ventilated region is embedded in the pool defined as a region which is not connected to the eastern boundary via any  $q_2$ -contour. The existence of the pool indicates an unventilated recirculation (Figs. 2.3d and 2.4d) which is not directly driven by the external forcing (Rhines and Young, 1982). The gradients of  $q_2$  appear to be very small in the pool for  $H = 5$  (Fig. 2.3b), whereas a new maximum is created west of the ventilated tongue for  $H = 4$  (Fig. 2.4b). We expect, therefore, that the former case satisfies the requirement for potential vorticity homogenization proposed in Chapter 3, i.e., vortex stretching is not very strong so that the zonal characteristic speed for  $q_2$  directs westward. The principal difference from the quasigeostrophic result given in Chapter 3 is that the uniform region is contaminated by the ventilated circulation.

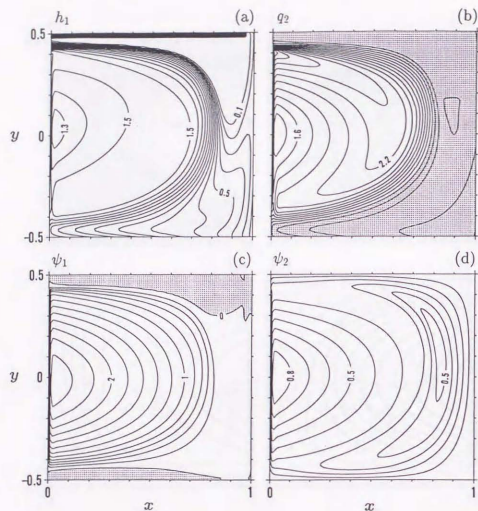


Figure 2.7. As in Fig. 2.1 but for Case 7. Contour intervals are (a) 0.1, (b) 0.15, (c) 0.2, (d) 0.1, respectively.

#### 2.4.3 Shallow-ocean regime

Figure 2.5 shows the solutions for  $H = 3$ . The subtropical bowl is located near the southern coast (Fig. 2.5a). The outcrop is compressed further northward but slightly extends eastward compared with the preceding cases. A new bowl-shaped structure of  $h_1$  is created adjacent to the western coast, which is reflected in the pool of high potential vorticity (Fig. 2.5b). A low- $q_2$  tongue emanating from the outcrop encircles this inner pool and almost reaches the western boundary layer. In contrast to the preceding intermediate cases, the ventilated region and the inner pool are clearly separated. In fact, Fig. 2.5d indicates that a substantial part of  $\psi_2$  is driven by ventilation, whereas the inner pool appears to be nearly compensated.

Figure 2.6 shows the solutions for  $H = 2$ . The pool expands further so that the outcrop is elongated zonally along the northern wall (Fig. 2.6a). A prominent feature

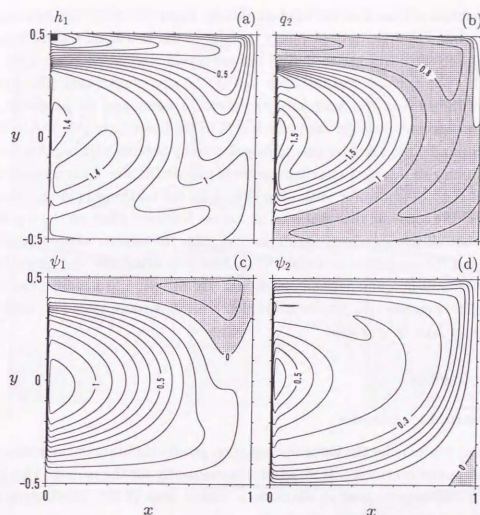


Figure 2.8. As in Fig. 2.1 but for Case 8. Contour intervals are (a) 0.1, (b) 0.1, (c) 0.1, (d) 0.05, respectively.

is a new sharp front between the pool and the outcrop. The  $q_2$ -field also reveals the following important dynamical properties (Fig. 2.6b). In the pool, a high- $q_2$  tongue encircles the centered minimum, indicating that the western boundary current acts as a source of high potential vorticity. On the other hand, a low- $q_2$  tongue from the outcrop travels outside the large pool until the southern edge of the western boundary layer is reached. There are large gradients in  $q_2$  between the pool and the ventilated region. In accordance with this thermocline structure, the  $\psi_2$ -field is separated into the ventilated and unventilated circulations unambiguously, and the front is not accompanied with a intense jet; we will return to this problem in the next section. We note that the ventilated circulation is inhibited at the southeast triangular region which is blocked by the  $q_2$ -contours emanating from the eastern boundary (cf. Luyten et al., 1983).

The above six cases concern the dependence of solutions on  $H$  for the realistic amplitude of the wind forcing. The following two cases examine the dependence of the



interesting solution of Case 6 on the wind amplitude. Figure 2.7 shows the solutions for  $\lambda = 0.7$ . It is found that the  $q_2$ -field is very uniform in the ventilated region, implying potential vorticity homogenization due to the ventilated circulation (Cox, 1985; Liu et al., 1993). The peculiar features seen in Fig. 2.6 are exaggerated; the outcrop now occupies the span of the basin near the northern boundary. In particular, the northward flow becomes stronger around  $x = 0.75$  in the lower layer (Fig. 2.6d). Since in the present model the vorticity sink is played only by bottom friction, this interior return current may be regarded as a consequence of *overventilation*. This interpretation is substantiated by the case of a weak wind (Fig. 2.8); the northward current vanishes in the interior. We conclude that this is an important frictional effect on the ventilated thermocline; not all the ventilated circulation can enter the viscous western boundary layer. Although the outcrop is very small (Fig. 2.8a), the ventilated and unventilated circulations can still be distinguished clearly and the former predominates the latter (Fig. 2.8d). This suggests that interfacial friction is an important agent for ventilation where the upper layer is very thin.

## 2.5 Discussion

### 2.5.1 Geostrophic contours

Geostrophic contours for the baroclinic equation greatly facilitate the interpretation of the present numerical results. If we assume conveniently for the moment that  $h_1 = O(1)$ , (2.32)–(2.35) may be used to eliminate  $u_1$  and  $v_1$  from (2.10). Eliminating then  $p_x$  and  $p_y$  using (2.36) and (2.37), we obtain

$$h_{1t} + J \left( \frac{\Psi}{H} - \frac{h_1 h_2}{f}, h_1 \right) = \lambda \left( \frac{h_2 \tau^x}{fH} \right)_y + \nu \nabla \cdot \left( \frac{1}{f^2} \nabla h_1 \right) + \delta \nabla \cdot \left( \frac{h_1^2}{f^2 H^2} \nabla h_1 \right) - \delta \nabla \cdot \left( \frac{h_1}{f H^2} \nabla \Psi \right) + \left( \frac{\nu}{h_1^2} - \frac{\delta}{H^2} \right) \frac{\lambda \tau^x}{f^2} h_{1x}. \quad (2.39)$$

This is the time-dependent baroclinic equation to the first approximation with respect to  $\nu$  and  $\delta$ . Thus, the isolines of

$$q \equiv \frac{\Psi}{H} - \frac{h_1 h_2}{f} = \text{const.} \quad (2.40)$$

give the geostrophic contours which are closely associated with the baroclinic motion.

Figure 2.9a shows the spin-up process of  $q$  for  $H = 2$  (cf. Fig. 2.6). When  $H$  (and also  $h_2$ ) is small, the evolution of  $q$  is strongly influenced by the barotropic flow [see (2.40)] which has been assumed to be established instantaneously in the present model. Accordingly, the broad pool region is created rapidly due to  $\Psi$ , while the ventilated region evolves gradually north of the pool. It is confirmed that the ventilated tongue

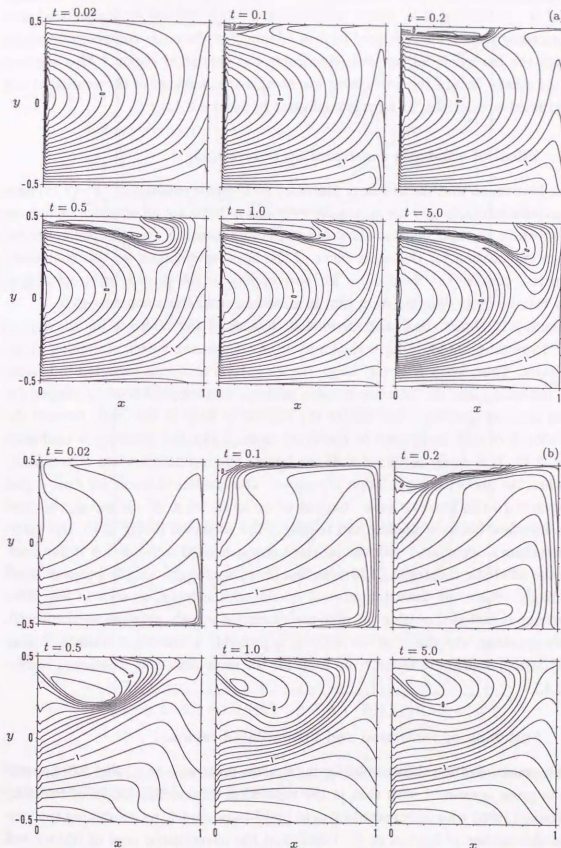


Figure 2.9. Evolution of the geostrophic contours represented by  $\Psi/H - h_1 h_2/f = \text{const.}$  for (a)  $H = 2$  (Case 6) and (b)  $H = 5$  (Case 3). Contour interval is 0.1.

does not penetrate into the pool throughout the spin-up process. Figure 2.9b shows the case of  $H = 5$  (cf. Fig. 2.3). When  $H$  increases,  $q$  is less affected by  $\Psi$  compared with the preceding case. Thus, the pool evolves as slowly as the outer compensated region through the baroclinic adjustment, containing the ventilated region. This suggests that the steady flow in the lower layer is a complicated mixture of the ventilated and unventilated circulations, as already confirmed in Section 2.4.2.

### 2.5.2 Effect of adiabatic constraint on outcropping

We have found that the two-layer planetary geostrophic equations (2.8)–(2.13) have two extreme solutions and the successive solutions in between, all of which include an outcrop whose size and shape are changed as the total depth  $H$  changes. Here, we give a rough explanation for the dependence of the layer outcropping on this controlling parameter, because the mechanism for outcropping in the present subtropical-gyre model may be quite different from that in a model containing a subpolar gyre.

Figure 2.10 shows zonal and meridional sections of the interface for the typical cases. Increasing the lower-layer thickness means decreasing vortex stretching in the lower layer. Thus, when  $H$  is very large, the lower-layer motion is expected to be very weak, indicating that the interface deepens to shape a subtropical bowl to compensate for the pressure gradient. The size of the outcrop is large in this case, because the total volume of each layer must be conserved from (2.16); this tendency is confirmed in Fig. 2.10. It is easily predicted that the largest outcrop occurs when  $H$  is infinity, i.e., when the perfect compensation is realized. Our numerical result for Case 1 just corresponds to this extreme case. On the other hand, when  $H$  decreases, the bowl of the interface becomes shallow and relatively flat as shown in Fig. 2.10; this interface structure is associated with the intense uncompensated recirculation in the pool. From the adiabatic constraint (2.16), the size of the northwest outcrop becomes small accordingly. Since the unventilated pool dominates the basin, as seen in Fig. 2.9a, the outcrop is excluded outside the pool and elongated zonally near the northern wall. Strictly speaking, the shape of the outcrop is probably a numerical artifact; it may extend further southward outside the front for the same reason as mentioned in Section 2.4.1.

### 2.5.3 Matching of ventilated and unventilated regions

The structure of the thermocline for the shallow-ocean case (e.g., Fig. 2.6) appears to be in gross agreement with that in the theoretical thermocline model of Pedlosky and Young (1983) who constructed inviscid multi-layer models by combining the ventilated thermocline of Luyten et al. (1983) and the unventilated pool of Rhines and Young (1982). Their analytical solutions are continuous everywhere but may not be

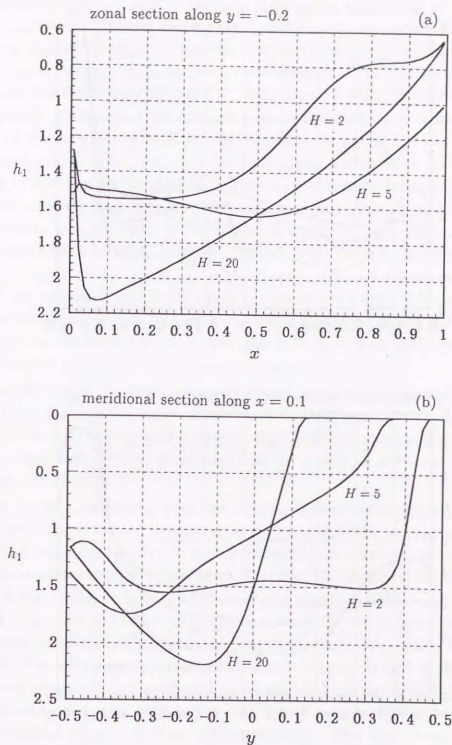


Figure 2.10. Interface displacement along (a)  $y = -0.2$  and (b)  $x = 0.1$  for three values of  $H$  corresponding to Cases 1, 3 and 6, respectively.



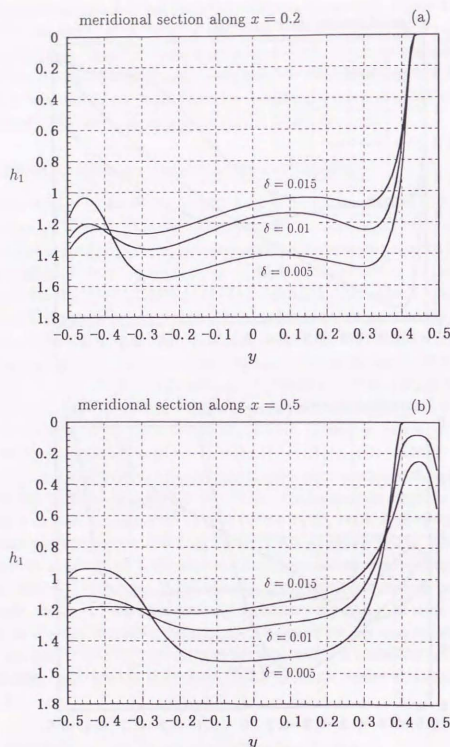


Figure 2.11. Interface displacement along (a)  $x = 0.2$  and (b)  $x = 0.5$  for Cases 9 to 11.

differentiable at the perimeter of the pool; a derivative layer might be formed at the rapid transition of the gradients of the interface if viscosity was included. However, our numerical solution contains the front-like structure between the ventilated and unventilated regions, strongly implying jump discontinuities in the thermocline and in the associated flow fields (see Figs. 2.6–2.8). Such discontinuities are possible because of the hyperbolic characters of the two-layer planetary geostrophic equations as shown in Chapter 1, and any discontinuity may be smoothed out by the frictions introduced in the present model. Figure 2.11 shows two meridional sections of  $h_1$  for Cases 9 to 11 in order to demonstrate the effect of  $\delta$  on the front ( $\nu$  is fixed at 0.005; see Table 2.1). As clearly seen, the jump between the outcrop and pool increases as  $\delta$  decreases. We note, however, that the width of the interior layer appears to be insensitive to  $\delta$ ; the same is true when  $\nu$  is varied with  $\delta$  fixed (not shown). Thus, the apparent front turns out to correspond to the narrow compensated region, which is consistent with the gap between the ventilated and unventilated circulations (Figs. 2.6d, 2.7d and 2.8d). The interface variation necessary for compensation can also be confirmed in Fig. 2.10a. Interestingly, an essentially similar configuration is fairly realized analytically (Fig. 1.9) despite the fact that the analytical case is oversimplified.

A similar frontal structure caused by strong nonlinearity is discussed by Dewar (1991) using a simple two-layer model in which a diffusion term is applied in the continuity equation as diapycnal density mixing. In our adiabatic model, on the other hand, the equivalent diffusion terms arise from the interfacial and bottom frictions via geostrophy [cf. (2.39)].

When vortex stretching is weak, the outcrop shrinks northwestward, but a weak front may be created around the outcrop as shown analytically in Chapter 1 (Figs. 1.6 and 1.7). A corresponding feature is still discernible just south of the outcrop in our numerical solutions (Figs. 2.3a and 2.4a). However, the analytical solutions miss the tongue of low potential vorticity which emanates from the outcrop and intrudes into the pool (Figs. 2.3b and 2.4b). In the present study, this important physical process in the purely wind-driven circulation has been verified only numerically. Finally, when  $D_2 \gg D_1$ , the lower layer is compensated almost completely and at the same time the outcrop expands further southward due to the adiabatic requirement (2.16). Thus, jump discontinuities occur between the outcrop and compensated region; an interior layer is required to connect these regions smoothly. This case corresponds to the Parsons (or Kamenkovich-Reznik) model which can be solved in closed form as shown in Chapter 1. The present numerical calculations (Figs. 2.1 and 2.2) reproduce such extreme cases reasonably well.

In this way, the major theoretical models may be linked within the framework of the present two-layer model. Between the Parsons-type model and ventilated thermocline model, there are successive states which may be obtained from each other by

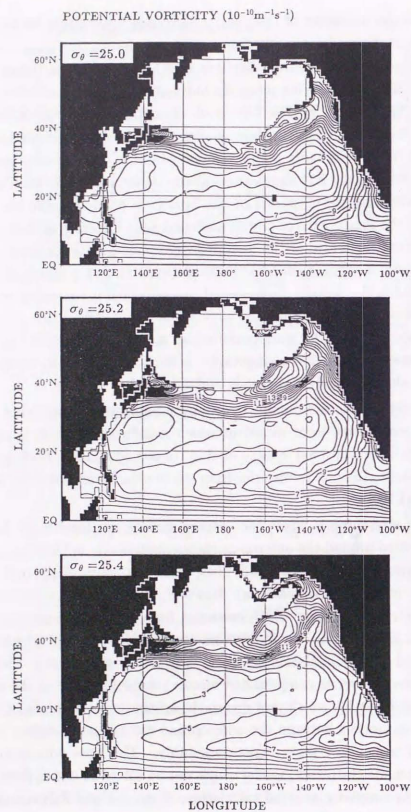


Figure 2.12. Annual-mean distribution of potential vorticity [ $10^{-10} \text{m}^{-1} \text{s}^{-1}$ ] and depth [m] on the isopycnal surfaces of  $\sigma_\theta = 25.0$  to  $26.0$  every  $0.2\sigma_\theta$ .

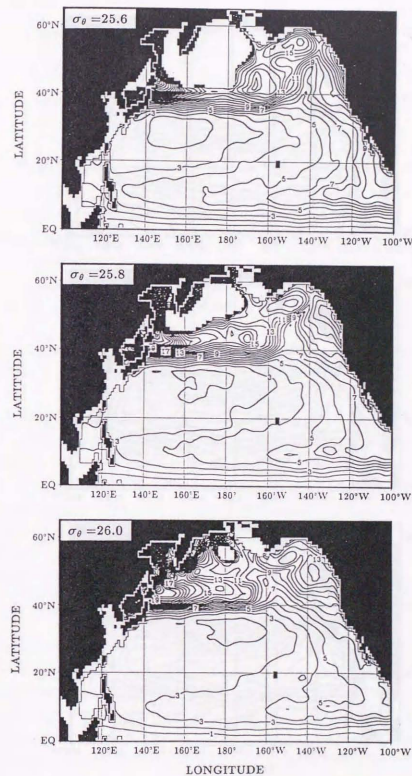


Figure 2.12. (Continued.)



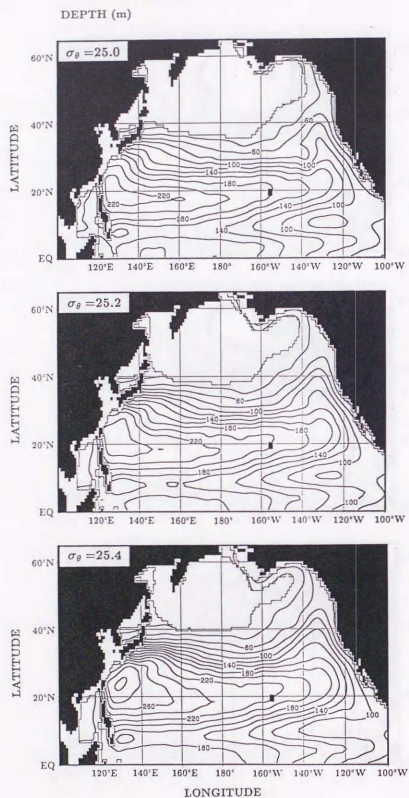


Figure 2.12. (Continued.)

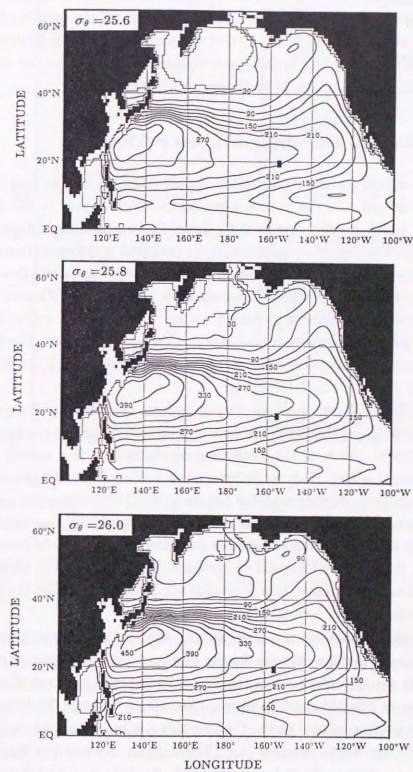


Figure 2.12. (Continued.)

continuously changing the degree of compensation. The existence of jump discontinuities implies that the solution for the pool cannot be determined from outside, i.e., cannot be determined by simple matching with the solution for the ventilated region. Thus, we return to the well-known difficulty that the pool solution must be determined internally, presumably taking into account the western boundary layer, as originally proposed by Rhines and Young (1982) and Ierley and Young (1983).

## 2.6 Application to the observational evidence

Our numerical results for the intermediate regime (Cases 3 and 4) may be used to gain a physical insight into the oceanic phenomena which appear in the updated field maps for the North Pacific. Figure 2.12 shows the annual-mean climatological depth distribution of the isopycnal surfaces and the potential vorticity distribution on each isopycnal surface. The hydrographic data used for these maps come from World Ocean Atlas 1994 compiled by National Oceanographic Data Center. These maps are drawn on various isopycnal surfaces ranging from  $\sigma_\theta = 25.0$  to  $27.8$  every  $0.2\sigma_\theta$  by quadratically interpolating the vertical profile of  $\sigma_\theta$  (Yamagata, personal communication). Potential vorticity is defined using standard notation as  $(f/\rho_0)(\partial\sigma_\theta/\partial z)$  with  $\rho_0 = 1000 \text{ kg m}^{-3}$ .

On the  $26.0\sigma_\theta$  isopycnal, potential vorticity is uniform over the broad region with a local minimum at  $32^\circ\text{N}$ ,  $177^\circ\text{E}$ . This minimum can be traced back to the uppermost isopycnal (e.g., at  $25^\circ\text{N}$ ,  $136^\circ\text{E}$  on the  $25.0\sigma_\theta$  isopycnal), so that it is usually related to the subtropical mode water. Such an isolated minimum would not be generated by winds in the ventilated thermocline model of Luyten et al. (1983) where the ventilated circulation just encircles the pool. However, we have already shown numerically that there are such cases that the ventilated region is contained in the pool. In fact, the  $q_2$ -distribution in Fig. 2.3 is in good qualitative agreement with the observed distribution on the  $26.0\sigma_\theta$  isopycnal. We suggest, therefore, that subductive ventilation is a possible mechanism for the mode-water formation (cf. Talley, 1988).

In the numerical solutions for the intermediate and shallow oceans (Figs. 2.3c, 2.4c and 2.5c), there are surface currents flowing eastward below the central latitude. A similar feature is actually observed in the North Pacific, which is called the subtropical countercurrent (Yoshida and Kidokoro, 1967; Hasunuma and Yoshida, 1978). The countercurrent is often related to the C-shape thermocline which is a well-known phenomenon also in the North Atlantic (e.g., Reid, 1981). Several mechanisms for the subtropical countercurrent have been suggested: Yoshida and Kidokoro (1967) explained that the countercurrent may be reproduced simply by changing the wind pattern. Holland (1978), using an eddy-resolving quasigeostrophic model, associated the westward return current with the inertial recirculation. Huang (1987), using a

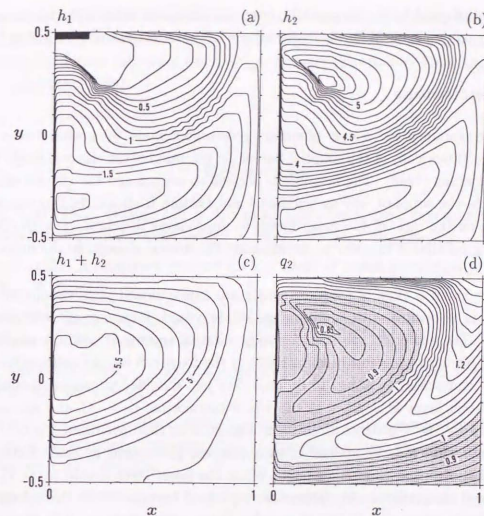


Figure 2.13. Steady-state solutions for the 2.5-layer model calculated using the FCT algorithm. The density difference between the upper and middle layers is twice as large as that between the middle and lower layers, and the other parameters are the same as used for Case 3. (a)  $h_1$ . (b)  $h_2$ . (c)  $h_1 + h_2$ . (d)  $q_2$ . Contour intervals are (a) 0.1, (b) 0.1, (c) 0.1, (d) 0.025, respectively. The black region of  $h_1$  indicates the outcrop. The values of  $q_2$  less than 1 are shaded.

2.5-layer model, found a C-shape structure which appears to be closely related to the shape of the surfacing line. Cushman-Roisin (1984) included thermodynamic effects and concluded that the subtropical countercurrent may be formed and maintained by the thermally driven flow. The present numerical results suggest that a countercurrent may be caused by the ventilated circulation, because the total transport is restricted by the Sverdrup relation. It is interesting to note that a similar countercurrent associated with pseudoventilation is produced also in the quasigeostrophic model (Hendershott, 1989).

One may pose the question about the utility of the present flat-bottom model for discussing the oceanic main thermocline, because the observational maps clearly show



the deep subtropical bowl. Fortunately, however, the gross features in the numerical solutions remain unchanged for the more realistic 2.5-layer model as shown in Fig. 2.13.

## 2.7 Conclusions

We have examined a two-layer planetary geostrophic model for a wind-driven subtropical gyre numerically as the simplest baroclinic extension of the classical single-layer model of Stommel (1948). The interface is allowed to surface and the viscous effect is introduced in the simplest way as interfacial and bottom frictions. In this study, we concentrate on the ratio of the mean lower- to upper-layer thickness,  $\alpha = D_2/D_1$ , as a controlling parameter in order to demonstrate the drastic changes in the numerical solutions.

We have found a class of solutions which are characterized by a viscous interior layer which is associated with outcropping. When  $\alpha \gg 1$ , Parsons-type solutions are reproduced. The numerical solutions are in qualitative agreement with the analytical solutions of Kamenkovich and Reznik (1972) in the Sverdrup interior, although, even for  $\alpha \sim 10$ , compensation seems to be imperfect just outside the western boundary. When the lower layer is as thick as the whole thermocline ( $\alpha \sim 4$ ), the solution is characterized by the ventilated circulation contained in the unventilated pool. This intermediate regime may be applied to such observed phenomena as mode water formation and subtropical countercurrents. When the lower layer is thin ( $\alpha \sim 1$ ), the ventilated and unventilated circulations are separated between which the submerged layer is perfectly compensated. It is shown that the interface displacement between the outcrop and the pool increases as the bottom friction coefficient decreases, implying a jump discontinuity in an inviscid limit. With sufficiently strong winds, a part of the ventilated circulation cannot enter the western boundary layer to close on itself in the eastern part of the interior. These types of solutions (the moderate and thin cases) cannot be covered by the so-called ventilated thermocline theory developed in the 1980s (e.g., Luyten et al., 1983; Pedlosky and Young, 1983). This is primarily because the latter "modern" theory assumes the tight thermal interaction between the ocean and the atmosphere implicitly; the gyre cannot be closed near the western coast. We also suggest that the inviscid models for the ventilated thermocline may be developed further by taking into account jump discontinuities.

Therefore, the two-layer Stommel problem has rich solutions which can be covered by neither quasigeostrophic nor reduced gravity models. Although many of the interesting features found here should be understood in the context of geophysical fluid dynamics, it should be emphasized that the above interesting phenomena have not been captured by the reduced-gravity-based, more "realistic" numerical models (cf. Chassignet and Bleck, 1993; Chassignet et al., 1995). We note also that the present

numerical model has the potential advantage of incorporating variable bottom topography. Discontinuous solutions for the wind-driven circulation over a bottom slope are an uncultivated issue except for the quasigeostrophic approach by Cessi and Pedlosky (1986) and Cessi (1989).

## References

- Bogue, N. M., R. X. Huang, and K. Bryan K. 1986. Verification experiments with an isopycnal coordinate ocean model. *J. Phys. Oceanogr.* **16**, 985-990.
- Bryan, K. 1969. A numerical method for the study of ocean circulation. *J. Comput. Phys.* **4**, 347-376.
- Cessi, P. 1989. On the role of topography in the ocean circulation: Diffusive and inertial effects. *J. Phys. Oceanogr.* **19**, 841-852.
- Cessi, P. and J. Pedlosky. 1986. On the role of topography in the ocean circulation. *J. Mar. Res.* **44**, 445-471.
- Chassignet, E. P. and R. Bleck. 1993. The influence of layer outcropping on the separation of boundary currents: Part I: The wind-driven experiments. *J. Phys. Oceanogr.* **23**, 1485-1507.
- Chassignet, E. P., R. Bleck, and C. G. H. Rooth. 1995. The influence of layer outcropping on the separation of boundary currents: Part II: The wind- and buoyancy-driven experiments. *J. Phys. Oceanogr.* **25**, 2404-2422.
- Cloke, P. and M. J. P. Cullen. 1994. A semi-geostrophic ocean model with outcropping. *Dyn. Atmos. Oceans* **21**, 23-48.
- Cox, M. D. 1985. An eddy resolving numerical model of the ventilated thermocline. *J. Phys. Oceanogr.* **15**, 1312-1324.
- Cushman-Roisin, B. 1984. On the maintenance of the subtropical front and its associated countercurrent. *J. Phys. Oceanogr.* **14**, 1179-1190.
- Dewar, W. K. 1991. Arrested fronts. *J. Mar. Res.* **49**, 21-55.
- Hasunuma, K. and K. Yoshida. 1978. Splitting of the subtropical gyre in the western North Pacific. *J. Oceanogr. Soc. Japan* **34**, 160-172.
- Hendershott, M. C. 1989. The ventilated thermocline in quasigeostrophic approximation. *J. Mar. Res.* **47**, 33-53.
- Holland, W. R. 1967. On the wind-driven circulation in an ocean with bottom topography. *Tellus* **19**, 582-600.

- Holland, W. R. 1978. The role of mesoscale eddies in the general circulation of the ocean—numerical experiments using a wind-driven quasi-geostrophic model. *J. Phys. Oceanogr.* **8**, 363–392.
- Holland, W. R. and L. B. Lin. 1975. On the generation of mesoscale eddies and their contribution to the oceanic general circulation. I. A preliminary numerical experiment. *J. Phys. Oceanogr.* **5**, 642–657.
- Huang, R. X. 1986. Numerical simulation of wind-driven circulation in a subtropical/subpolar basin. *J. Phys. Oceanogr.* **16**, 1635–1650.
- Huang, R. X. 1987. A three-layer model for wind-driven circulation in a subtropical-subpolar basin. Part II: The supercritical and hypercritical states. *J. Phys. Oceanogr.* **17**, 679–697.
- Ierley, G. R. and W. R. Young. 1983. Can the western boundary layer affect the potential vorticity distribution in the Sverdrup interior of a wind gyre? *J. Phys. Oceanogr.* **13**, 1753–1763.
- Jarvis, R. A. and G. Veronis. 1994. Strong deep recirculations in a two-layer wind-driven ocean. *J. Phys. Oceanogr.* **24**, 759–776.
- Kamenkovich, V. M. and G. M. Reznik. 1972. A contribution to the theory of stationary wind-driven currents in a two-layer liquid. *Izv. Acad. Sci. USSR Atmos. Oceanic Phys.* (English translation) **8**, 238–245.
- Liu, Z., J. Pedlosky, D. Marshall, and T. Warnke. 1993. On the feedback of the Rhines-Young pool on the ventilated thermocline. *J. Phys. Oceanogr.* **23**, 1592–1596.
- Luyten, J. R., J. Pedlosky, and H. Stommel. 1983. The ventilated thermocline. *J. Phys. Oceanogr.* **13**, 292–309.
- National Oceanographic Data Center. 1994. *World Ocean Atlas 1994* (CD-ROM Data Set Documentation), Washington, D.C.
- Parsons, A. T. 1969. A two-layer model of Gulf Stream separation. *J. Fluid Mech.* **39**, 511–528.
- Pedlosky, J. 1990. The dynamics of the oceanic subtropical gyres. *Science* **248**, 316–322.
- Pedlosky, J. and W. R. Young. 1983. Ventilation, potential-vorticity homogenization and the structure of the ocean circulation. *J. Phys. Oceanogr.* **13**, 2020–2037.
- Reid, J. L. 1981. On the mid-depth circulation of the world ocean. In: *Evolution of Physical Oceanography* (B. A. Warren and C. Wunsch, eds.), pp. 70–111. The MIT Press, Cambridge and London.

- Rhines, P. B. and W. R. Young. 1982. A theory of the wind-driven circulation I. Mid-ocean gyres. *J. Mar. Res.* **40** (Suppl.), 559–596.
- Sakamoto, T. and T. Yamagata. 1996. Seasonal transport variations of the wind-driven ocean circulation in a two-layer planetary geostrophic model with a continental slope. *J. Mar. Res.* **54**, 261–284.
- Stommel, H. 1948. The westward intensification of wind-driven ocean currents. *Trans. Am. Geophys. Union* **29**, 202–206.
- Sun S., R. Bleck, and E. P. Chassignet. 1993. Layer outcropping in numerical models of stratified flows. *J. Phys. Oceanogr.* **23**, 1877–1884.
- Talley, L. D. 1988. Potential vorticity distribution in the North Pacific. *J. Phys. Oceanogr.* **18**, 89–106.
- Veronis, G. 1966. Wind-driven ocean circulation—Part 1. Linear theory and perturbation analysis; Part 2. Numerical solutions of the non-linear problem. *Deep-Sea Res.* **13**, 17–55.
- Welander, P. 1966. A two-layer frictional model of wind-driven motion in a rectangular oceanic basin. *Tellus* **18**, 54–62.
- Welander, P. 1971. Some exact solutions to the equations describing an ideal-fluid thermocline. *J. Mar. Res.* **29**, 60–68.
- Yee, H. C. 1987. Construction of explicit and implicit symmetric TVD schemes and their applications. *J. Comput. Phys.* **68**, 151–179.
- Yoshida, K. and T. Kidokoro. 1967. A subtropical countercurrent (II)—A prediction of eastward flows at lower subtropical latitudes. *J. Oceanogr. Soc. Japan* **23**, 231–246.



## Appendix to Chapter 2

### Numerical solution to Parsons' Model using TVD schemes

#### A.1 Introduction

In the large-scale oceans, isopycnal surfaces vary in space considerably, and some of those isopycnals are uncovered to the ocean surface at certain middle or high latitudes (see Fig. 2.12). In Chapter 1, we have shown that such a surfacing line is related to a jump discontinuity which is inherent of the planetary geostrophic equations; a special treatment is needed to determine the location of the surfacing line. In general, an outcrop is accompanied with an interior layer when viscosity is taken into account, as shown numerically in Chapter 2. Such interior layers are characterized by strong nonlinearity due to  $O(1)$  interface displacement and hence are very different from the familiar western boundary layer.

An outcrop in layer models gives rise to numerical difficulties as well. With an ordinary numerical scheme of the second-order accuracy, unphysical oscillations are produced where the gradients of dependent variables are very large. To avoid such spurious oscillations, various high resolution schemes have been devised for solving an initial value problem for conservation equations [see the review in van Leer (1997)]. These schemes are successful in representing a jump discontinuity like a shock numerically within an acceptable level of artificial diffusivity. In physical oceanography, the FCT and related algorithms have been used to reproduce outcropping layers (Huang, 1986; Bogue et al., 1986; Sun et al., 1993; Cloke and Cullen, 1994). Now several new flux and slope limiter methods based on the Total Variation Diminishing (TVD) concept can be used to investigate oceanographic problems including front-like structures.

In this appended chapter, we apply TVD schemes to a 1.5-layer planetary geostrophic model which allows for an outcrop. In particular, an attempt is made to confirm the analytical solution for a subtropical gyre provided by Parsons (1969) using numerical solutions calculated with various TVD schemes as well as the FCT algorithm. It should be noted that the matching between the western boundary current and the interior jet is uncertain in Parsons' procedure [see also Kamenskovich and Reznik (1972)],

which reminds us that boundary layer separation is still one of the controversial issues in ocean dynamics (cf. Ierley, 1990; Myers et al., 1996). In fact, an overshooting of the western boundary current is often observed in the previous numerical results (e.g., Huang, 1986; Bogue et al., 1986). Such a recirculating boundary current is not a trivial phenomenon in the planetary geostrophic regime and must be distinguished from the inertial recirculations which appear in more complicated ocean models (cf. Cloke and Cullen, 1994; Chassignet, 1995). We verify the behavior of the interior layer near the separation point for Parsons' Model by performing the numerical experiment carefully.

## A.2 Model equations

Consider a rectangular basin on a  $\beta$ -plane whose characteristic width is  $L$ . For a square basin, for example, the domain is  $0 \leq x \leq L$ ,  $-L/2 \leq y \leq L/2$ , where  $x$  directs eastward and  $y$  directs northward. The Coriolis parameter is represented by  $f = f_0 + \beta_0 y$  with  $f_0$  and  $\beta_0$  constant. The upper layer has density  $\rho_1$  and thickness  $h$ , while the lower layer has density  $\rho_2$  and is motionless. We again assume the planetary geostrophic approximation as well as the rigid-lid, Boussinesq and hydrostatic approximations, all of which are appropriate to motion whose horizontal scale is much larger than the baroclinic deformation radius. Then, the governing equations are

$$-f h v = -g' h h_x - K u + \tau^x / \rho_0, \quad (\text{A.1})$$

$$f h u = -g' h h_y - K v, \quad (\text{A.2})$$

$$h_t + (h u)_x + (h v)_y = 0, \quad (\text{A.3})$$

where  $(u, v)$  is the horizontal velocity,  $g' = (\rho_2 - \rho_1) / \rho_0$  is the reduced gravity with a reference density  $\rho_0$ , and  $\tau^x$  is the zonal wind stress which is a function of  $y$  only. Momentum dissipation is introduced as interfacial friction parameterized as a simple drag with a coefficient  $K$ . For the system (A.1)–(A.3), the boundary condition is simply

$$\begin{aligned} u &= 0 \quad \text{at the meridional boundaries,} \\ v &= 0 \quad \text{at the zonal boundaries.} \end{aligned} \quad (\text{A.4})$$

For later convenience, we nondimensionalize these equations by scaling  $(x, y)$  by  $L$ ,  $h$  by the mean upper-layer thickness  $D$ ,  $f$  by  $f_0$ ,  $(u, v)$  by  $u_0 \equiv g' D / (f_0 L)$ ,  $t$  by  $L / u_0$  and  $\tau^x$  by  $\tau_0$ . The resulting dimensionless equations are

$$-f V = -h h_x - \epsilon U / h + \lambda \tau^x, \quad (\text{A.5})$$

$$f U = -h h_y - \epsilon V / h, \quad (\text{A.6})$$

$$h_t + U_x + V_y = 0, \quad (\text{A.7})$$

where the volume transport  $(U, V) = (h u, h v)$  has been introduced and the Coriolis parameter is now  $f = 1 + \beta y$  with  $\beta = \beta_0 L / f_0$ . The other nondimensional parameters

are defined as  $\epsilon = K / (f_0 D)$  and  $\lambda = \tau_0 L / (\rho_0 g' D^2)$ . We note that the nondimensional unit time corresponds to  $F_r / f_0$ , where  $F_r = f_0^2 L^2 / (g' D)$  is the baroclinic rotational Froude number. The domain of the experiment is now  $0 \leq x \leq 1$ ,  $-0.5 \leq y \leq 0.5$  for the square basin unless otherwise stated.

Integration of the continuity equation (A.7) over the whole basin yields the following constraint which is of crucial importance in the present adiabatic model:

$$\iint h \, dx \, dy = \text{constant}, \quad (\text{A.8})$$

i.e., the total volume is regarded as an external parameter (Parsons, 1969). On the other hand, the momentum equations can be solved for the velocity components as

$$\begin{aligned} U &= \left[ -\left(\frac{h}{\epsilon}\right)^2 f h h_y + \frac{h}{\epsilon} (-h h_x + \lambda \tau^x) \right] / \left[ 1 + \left(\frac{f h}{\epsilon}\right)^2 \right], \\ V &= \left[ -\left(\frac{h}{\epsilon}\right)^2 f (-h h_x + \lambda \tau^x) - \frac{h}{\epsilon} h h_y \right] / \left[ 1 + \left(\frac{f h}{\epsilon}\right)^2 \right]. \end{aligned} \quad (\text{A.9})$$

We note that both  $U$  and  $V$  become zero automatically when  $h = 0$ . Eq. (A.9) is actually used in the later numerical calculations.

## A.3 Numerical Method

We solve the initial value problem, (A.7) and (A.9) with (A.4), numerically subject to an initial condition stated at each experiment. Numerical calculation is conducted on a regularly spaced, staggered B-grid. In particular, the coastal boundaries coincide with the outermost cell boundaries. The arrangement of the dependent variables is shown in Fig. A.1. The Coriolis and wind forcing terms are located at the  $(u, v)$  points. In addition to the advantages in simulations of large-scale ocean circulations (cf. Bogue et al., 1986), the B-grid seems to be more suitable than any other grid system for the present model because the finite difference forms of the model equations become the most compact.

As mentioned in the first section, we cannot solve (A.7) using the ordinary, high-order accurate schemes when an outcrop ( $h = 0$ ) occurs. Various new flux and slope limiter methods have been developed to solve first-order partial differential equations based on the TVD concept proposed by Harten (1983). These schemes are so designed as to capture large gradients monotonically and at the same time to preserve the second-order accuracy in other smooth parts. The TVD approach has succeeded in circumventing the difficulty involved in Godunov's theorem concerning monotone schemes. Unfortunately, mathematically strict treatment has been made almost exclusively for scalar one-dimensional problems, and the extension to multidimensional



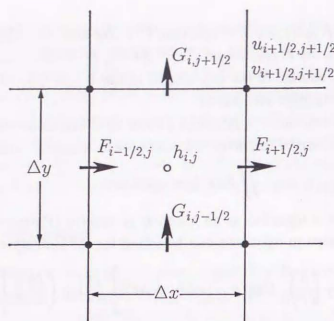


Figure A.1. Arrangement of variables and schematic fluxes on the B-grid used in the present experiment.

nonlinear systems is not straightforward in general (cf. Hirsch, 1990; Toro, 1997). However, we are greatly encouraged by the tremendously many successful computations accumulated in the last 15 years in numerous scientific and engineering fields.

Here, we apply this major achievement in computational fluid dynamics to an *incompressible* fluid to study oceanic fronts associated with layer outcropping. We concentrate on the explicit schemes, so we first rewrite (A.7) in spatial finite difference form at the  $n$ th time step as follows:

$$\left(\frac{d}{dt}h\right)_{i,j}^n = - \left( \frac{F_{i+1/2,j}^n - F_{i-1/2,j}^n}{\Delta x} + \frac{G_{i,j+1/2}^n - G_{i,j-1/2}^n}{\Delta y} \right). \quad (\text{A.10})$$

The arrangement of the numerical fluxes  $F$  and  $G$  is shown in Fig. A.1. Then, the zonal numerical flux  $F_{i+1/2,j}$  for each scheme can be written as listed in Table A.1. The meridional numerical flux  $G$  can be represented in a similar way. Among these schemes, TVD MUSCL scheme<sup>1</sup> is categorized in slope limiter methods, while the other schemes belong to flux limiter methods. As the flux limiter,<sup>2</sup> we adopt the standard minmod function given by

$$\text{minmod}(x, y) = \text{sgn}(x) \cdot \max\{0, \min[|x|, |y| \cdot \text{sgn}(x)]\}. \quad (\text{A.11})$$

<sup>1</sup>MUSCL stands for Monotone Upstream-centered Scheme for Conservation Laws (van Leer, 1979). We have chosen the parameter  $\omega$  so that the scheme is third-order accurate in space and time (Toro, 1997).

<sup>2</sup>The so-called "superbee" limiter cannot be used with the symmetric scheme (Yee, personal communication).

Table A.1. Finite difference form of various high resolution schemes

**TVD Lax-Wendroff:**

$$F_{i+1/2} = U_{i+1/2} - \frac{1}{2} \left\{ cu_{i+1/2}^2 Q(\Delta_{i-1/2}h, \Delta_{i+1/2}h, \Delta_{i+3/2}h) + |u_{i+1/2}| [\Delta_{i+1/2}h - Q(\Delta_{i-1/2}h, \Delta_{i+1/2}h, \Delta_{i+3/2}h)] \right\}$$

$$c = \frac{u_{i+1/2}\Delta t}{\Delta x}$$

$$\Delta_{i+1/2}h = h_{i+1,j} - h_{i,j}$$

$$U_{i+1/2} = \frac{(u_{i+1/2,j+1/2} + u_{i+1/2,j-1/2})(h_{i+1,j} + h_{i,j})}{4}$$

$$Q(x, y, z) = \text{minmod}(y, x) + \text{minmod}(y, z) - y$$

**Yee's symmetric scheme:**

$$F_{i+1/2} = U_{i+1/2} - \frac{1}{2} |u_{i+1/2}| [\Delta_{i+1/2}h - Q(\Delta_{i-1/2}h, \Delta_{i+1/2}h, \Delta_{i+3/2}h)]$$

**Yee's upwind scheme:**

$$F_{i+1/2} = U_{i+1/2} + |u_{i+1/2}\Delta_{i+1/2}h + \gamma_{i+1/2}| - \frac{1}{2} |u_{i+1/2}| (R_{i+1} + R_i)$$

$$R_i = \text{minmod}(\Delta_{i-1/2}h, \Delta_{i+1/2}h)$$

**Chakravarthy-Osher:**

$$F_{i+1/2} = \frac{1}{2}(h_i + h_{i+1}) - \frac{1}{2} |u_{i+1/2}| \Delta_{i+1/2}h$$

$$- \frac{1-k}{4} \text{minmod}(\Delta F_{i+3/2}^-, b\Delta F_{i+1/2}^-) - \frac{1+k}{4} \text{minmod}(\Delta F_{i+1/2}^-, b\Delta F_{i+3/2}^-)$$

$$+ \frac{1+k}{4} \text{minmod}(\Delta F_{i+1/2}^+, b\Delta F_{i+1/2}^+) + \frac{1-k}{4} \text{minmod}(\Delta F_{i-1/2}^+, b\Delta F_{i+1/2}^+)$$

$$\Delta F^\pm = u^\pm \Delta h, \quad u^\pm = \frac{1}{2}(u \pm |u|)$$

$$1 \leq b \leq \frac{3-k}{1-k}$$

**TVD MUSCL:**

$$F_{i+1/2} = \frac{1}{2} [1 + \text{sgn}(c)] F(\tilde{h}_i^R) + \frac{1}{2} [1 - \text{sgn}(c)] F(\tilde{h}_{i+1}^L)$$

$$F(\tilde{h}_i^R) = u_{i+1/2} \left[ h_i + \frac{1}{2}(1-c)\tilde{\Delta}_i \right], \quad F(\tilde{h}_{i+1}^L) = u_{i+1/2} \left[ h_{i+1} - \frac{1}{2}(1+c)\tilde{\Delta}_{i+1} \right]$$

$$\tilde{\Delta}_i = \xi_i \Delta \quad \xi_i : \text{slope limiter}$$

$$= \text{sgn}(\Delta_{i+1/2}) \cdot \max \left\{ 0, \min \left[ \frac{2}{1+c} \Delta_{i-1/2} \text{sgn}(\Delta_{i+1/2}), \frac{2}{1-c} \Delta_{i+1/2} \right] \right\}$$

$$\Delta_i = \frac{1}{2}(1+\omega)\Delta_{i-1/2}h + \frac{1}{2}(1-\omega)\Delta_{i+1/2}h$$

$$\omega = \frac{1}{3}[2c - \text{sgn}(c)]$$

**Phoenical SHASTA:**

$$h_i^* = h_i^* - \frac{1}{8} [(h_{i+1} - h_i)_{\text{lim}} - (h_i - h_{i-1})_{\text{lim}}]$$

$$\begin{cases} h_i \text{ is the updated solution obtained with a high accuracy method} \\ h_i^* = h_i + \frac{1}{8} (h_{i+1} - 2h_i + h_{i-1}) \\ h_i^* \text{ is the final solution} \end{cases}$$

$$(h_{i+1} - h_i)_{\text{lim}} = \begin{cases} \min[8|h_i - h_{i-1}|, |h_{i+1} - h_i|, 8|h_{i+2} - h_{i+1}|] \text{sgn}(h_{i+1} - h_i) \\ \text{if } \text{sgn}(h_i - h_{i-1}) = \text{sgn}(h_{i+1} - h_i) = \text{sgn}(h_{i+2} - h_{i+1}) \\ 0 \text{ otherwise} \end{cases}$$

We follow Yee's (1987) special treatment in order to take into account the case that  $h_{i,j} = 0$ . The boundary values are computed as follows. To obtain  $F_{-1/2,j}$ , for example, we take  $h_{0,j}$  and  $h_{-1,j}$  outside the western boundary which are set to be zero and apply them to the numerical flux in Table A.1 without any change. For the calculation of  $v_{1/2,j}$  using (A.9), on the other hand,  $h_{0,j}$  is linearly interpolated.

For comparison, we also use the Lax-Wendroff-based Phenical SHASTA<sup>3</sup> of the simplest form (van Albada et al., 1982) as an example of the FCT algorithm. The TVD schemes of the present form are conservative, so that they satisfy the crucial constraint (A.8) exactly, whereas the FCT algorithm does not.

For solving the ordinary differential equation (A.10), the simple first-order Euler method usually gives a satisfactory result. In some cases, however, an impractically small value of the time step  $\Delta t$  is needed to avoid small-scale disturbances along the southern boundary probably due to coastal Kelvin waves. When this happens, we use the two-stage Runge-Kutta method to improve the time accuracy. Provided the updated values of  $h_{i,j}$  are obtained, the corresponding velocity components are computed diagnostically from (A.9). The finite difference form of (A.9) is not special and hence is not shown here.

#### A.4 Wave propagation

Before proceeding to the main subject, two preliminary experiments are conducted to demonstrate the propagation of baroclinic long Rossby waves which play a primary role in transients in the present simple ocean model.

##### A.4.1 Propagation of a planetary eddy

The initial field is an isolated Gaussian eddy of the form

$$h(x, y) = \begin{cases} 2 \exp\{-64[(x-1.2)^2 + y^2]\} & r \leq 1/64 \\ 0 & r > 1/64, \end{cases} \quad (\text{A.12})$$

where  $[r = (x-1.2)^2 + y^2]^{1/2}$  (Fig. A.2). We note that the edge of the eddy has been cut off artificially. Computation is made in the rectangular domain  $0 \leq x \leq 1.6$ ,  $-0.4 \leq y \leq 0.4$  ( $L = 2000$  km) using Yee's symmetric or upwind scheme. The spatial resolution is  $\Delta x = \Delta y = 0.005$  and the time step is taken to be  $\Delta t = 2 \times 10^{-5}$  corresponding to about 49 minutes.

Figure A.3 shows the evolution of the eddy field for  $\beta = 0.55$ ,  $\epsilon = 0.004$  and  $\lambda = 0$ . We can confirm such physical properties as the westward propagation of the warm

<sup>3</sup>SHASTA stands for Sharp and Smooth Transport Algorithm (Boris and Book, 1973). Phenical SHASTA is a refinement of SHASTA (Book et al., 1975).

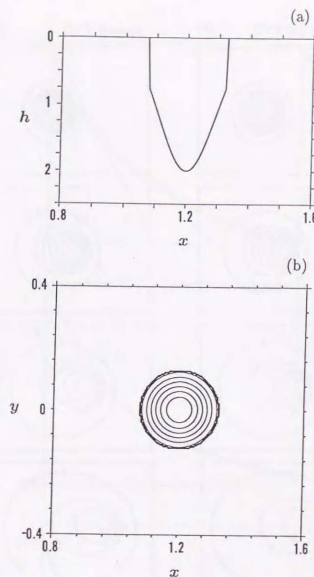


Figure A.2. Gaussian eddy of the form  $h = 2 \exp\{-64[(x-1.2)^2 + y^2]\}$  ( $r \leq 1/64$ );  $h = 0$  ( $r > 1/64$ ), where  $r = [(x-1.2)^2 + y^2]^{1/2}$ . (a) Side view at  $y = 0$ . (b) Plan view; contour interval is 0.2.

eddy, nonlinear steepening and meridional asymmetry, all of which are consistent with planetary geostrophic dynamics. Although the circumference of the eddy is smeared rapidly by the interfacial friction, no numerical oscillations are produced there and the eddy front is preserved quite well throughout the time stepping.

Figure A.4a shows the zonal position of the maximum interface displacement as a function of time, which traces the traveling eddy. For comparison, we also show other two trajectories for the linear waves of different phase speeds. The reference phase speed is  $\beta_0 g' / f_0^2$  in dimensional form and  $\beta$  in nondimensional unit. It is clearly seen that the movement of the eddy at the initial stage is in good agreement with that of the linear wave having a phase speed  $2\beta$  (recall that the initial amplitude of the eddy is



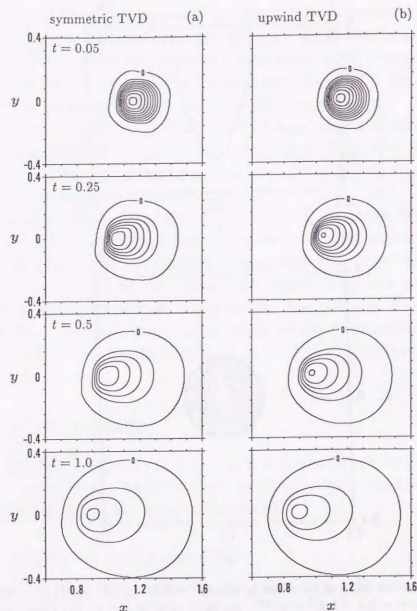


Figure A.3. Evolution of the isolated warm eddy of Fig. A.2 for  $\beta = 0.55$ ,  $\epsilon = 0.004$  and  $\lambda = 0$  calculated using (a) Yee's symmetric TVD scheme and (b) Yee's upwind TVD scheme. Contour interval is 0.2.

2). After  $t = 0.1$ , the propagation speed of the eddy decreases rapidly and eventually becomes less than the linear wave speed  $\beta$ .

The decay of the eddy field is important both physically and numerically. Figures A.4b and A.4c show the variation in the eddy amplitude and the variation in the total potential energy, respectively. It is found that the decay time estimated from the numerical result is much longer than the effective decay time  $\epsilon F_r \sim 0.047$  (39 days). This is because the physical dissipation is imposed only on the momentum equations (Sakamoto and Yamagata, 1997; Chapter 5). In other words, both TVD schemes

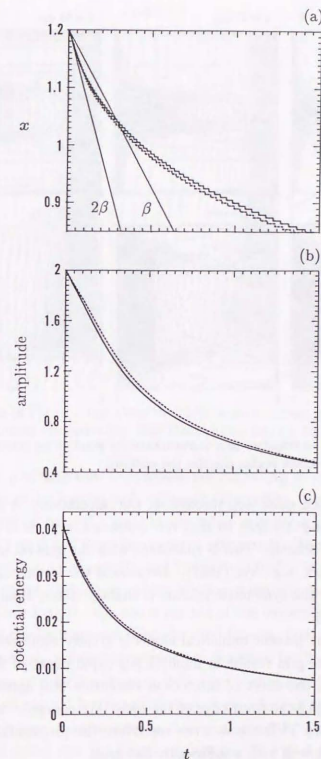


Figure A.4. Comparison between the symmetric TVD scheme (solid lines) and the upwind TVD scheme (dotted lines) corresponding to Fig. A.3. (a) Zonal position of the maximum interface displacement. Also shown are the cases of the linear waves of phase speeds  $\beta$  and  $2\beta$ , respectively. (b) Amplitude. (c) Potential energy.

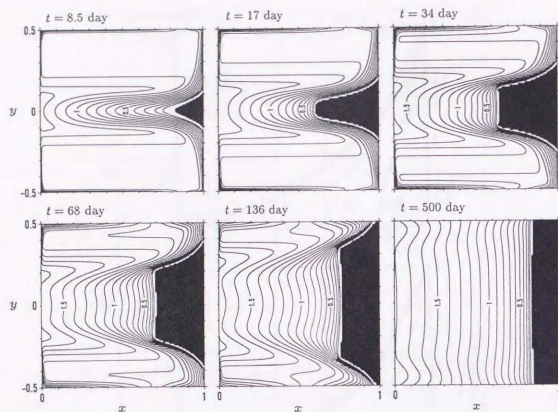


Figure A.5. Evolution of  $h$  in response to a uniform easterly wind on an equatorial  $\beta$ -plane. Contour interval is 0.1. The black region denotes the outcrop.

control numerical dissipation quite well throughout the calculations. A more detailed observation of Figs. A.3 and A.4 tells us that the symmetric scheme is slightly more diffusive than the upwind scheme. This is consistent with the general understanding about the TVD schemes [see, e.g., Yee (1987)]. Because of the latter numerical property, the eddy motion for the symmetric scheme is slightly slower than that for the upwind scheme (Fig. A.4a).

Spatial resolution of the present numerical model is greatly significant; a complementary run with a coarser grid results in unphysically rapid decay of the eddy field (not shown). In Fig. A.3, the effect of insufficient resolution still appears as a tendency toward the squaring of the front edge of the eddy. We conclude, however, that both symmetric and upwind TVD schemes can reproduce the propagation of a large-amplitude wave reasonably well with a sufficiently fine grid.

#### A.4.2 Spin-up of an equatorial ocean

The second verification experiment concerns the equatorial  $\beta$ -plane ( $L = 4000$  km) bounded by solid walls. The Coriolis parameter is now  $f = y$  in the nondimensional equations and the definition of the nondimensional parameters must be changed ac-

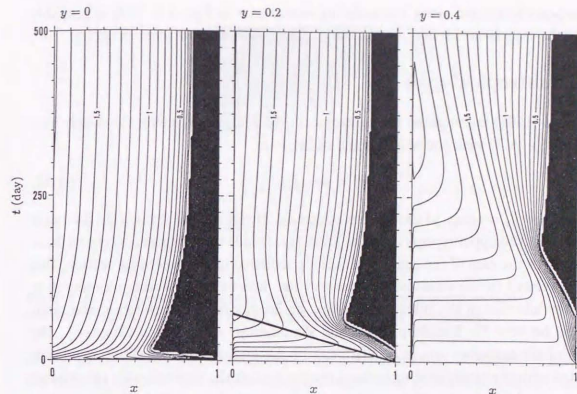


Figure A.6. As in Fig. A.5 but along the three zonal sections,  $y = 0$ ,  $y = 0.2$  and  $y = 0.4$ , respectively. Contour interval is 0.1. The black region denotes the outcrop.

cordingly. The grid and time resolutions are  $\Delta x = \Delta y = 0.01$  and  $\Delta t = 1 \times 10^{-7}$ , respectively; the latter corresponds to about 40 seconds. We examine the spin-up of the equatorial ocean from the state at rest when a uniform easterly wind is abruptly switched on at  $t = 0$  and remains constant afterwards. The response of such a system is well-known (e.g., Yamagata and Philander, 1985): Without diapycnal density mixing, the transient Yoshida jet, which is induced initially, fades away into no motion after the baroclinic long Rossby waves excited at the eastern boundary establish zonal pressure gradients which balance with the wind forcing. (Some interesting phenomena associated with diapycnal density mixing are discussed in Chapter 4.)

The evolution of  $h$  for  $\lambda = 2$ ,  $\epsilon = 6.29 \times 10^{-3}$  is shown in Fig. A.5 (plan view) and Fig. A.6 (zonal sections). At the initial stage, a signature of the westward propagation of the baroclinic long Rossby wave is clearly discernible. At  $y = 0.2$ , for example, the propagation speed (see the heavy straight line in Fig. A.6) is  $0.65 \text{ ms}^{-1}$  which is in good agreement with the phase speed of the linear equatorial nondispersive wave,  $0.67 \text{ ms}^{-1}$ . We can confirm that sharp fronts associated with the outcrop also move westward. These interior layers are transient, and the final steady state is the same as that just mentioned above. As predicted theoretically in Chapter 1, the surfacing line in the vicinity of the equator is associated with a *spontaneous* outcrop, i.e., simply a consequence of the eastward shoaling of the interface. (Strictly speaking, a thin viscous



layer appears to remain along the surfacing line as seen in Fig. A.6. This is probably because the interfacial friction may balance with the zonal wind where  $h \ll 1$ .)

### A.5 Subtropical gyre

Parsons (1969) investigated the subtropical gyre analytically using the steady version of (A.5)–(A.7) with the wind forcing of the form

$$\tau^x = \sin \pi y, \quad (\text{A.13})$$

subject to  $h = h_e = \text{const.}$  at the eastern boundary. He found that if the wind forcing is strong and/or the upper layer is thin, the lower layer tends to be exposed to the surface. In contrast to the case of the equatorial ocean considered in the preceding section, this is closely related to the total volume conservation, because the Ekman pumping may deepen the interface in the subtropics. Hence, an interior layer is required at the rapid transition between the Sverdrup region and the outcrop. As shown in Chapter 1, the position of the surfacing line,  $x = X(y)$ , can be determined from the jump condition associated with the corresponding inviscid system, so that the expression for the interior layer may be derived using the singular perturbation method with local coordinates  $(r, s)$  regarding the surfacing line ( $r = 0$ ) as a "western" boundary. Figure A.7 shows an example of Parsons' solution for  $h$  including the Sverdrup interior  $h_s$ , western boundary layer  $h_w$  and interior layer  $h_i$  as follows:

$$h_s = \left[ h_e^2 + \frac{2f}{\beta} \lambda (1-x) \frac{d\tau^x}{dy} - 2\lambda (1-x) \tau^x \right]^{1/2}, \quad (\text{A.14})$$

$$h_w = D_1 \frac{1 - B e^{-D_1 \beta x / \epsilon}}{1 + B e^{-D_1 \beta x / \epsilon}}, \quad (\text{A.15})$$

$$h_i = D_2 \frac{1 - e^{-D_1 f_s \tau / \epsilon}}{1 + e^{-D_1 f_s \tau / \epsilon}}, \quad (\text{A.16})$$

where

$$\begin{aligned} f_s &= \partial f / \partial s, \\ B &= \frac{D_1 - D_0}{D_1 + D_0}, \\ D_0^2 &= h_e^2 - 2\lambda \tau^x, \\ D_1^2 &= h_e^2 + \frac{2f}{\beta} \lambda \frac{d\tau^x}{dy} - 2\lambda \tau^x, \\ D_2^2 &= h_e^2 + \frac{2f}{\beta} \lambda (1-X) \frac{d\tau^x}{dy} - 2\lambda (1-X) \tau^x. \end{aligned}$$

As pointed out by Kamenkovich and Reznik (1972), however, this simple composite expansion might be invalid near the separation latitude. Huang (1986) suggested from

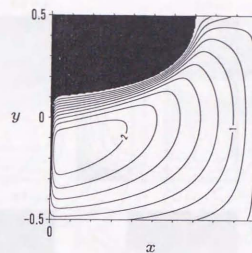


Figure A.7. Example of Parsons' analytical solution for  $h$  for  $\beta = 0.55$ ,  $\lambda = 0.53$  and  $\epsilon = 0.01$ . Contour interval is 0.2. The black region denotes the outcrop.

his numerical results that the western boundary current may overshoot to assure the net vorticity balance. The present numerical experiment allows us to make a convincing argument on the boundary layer separation for Parsons' model.

Numerical calculation is performed on a 2000 km  $\times$  2000 km basin in which the central latitude is located at 30°N. The spatial and time resolutions are varied; for instance,  $\Delta t$  is taken to be  $4 \times 10^{-5}$  corresponding to 97 minutes for a  $64 \times 64$  grid. The nondimensional parameters are chosen as  $\beta = 0.55$ ,  $\lambda = 0.53$  and  $\epsilon = 0.01$ , corresponding to, e.g.,  $D = 200$  m,  $g' = 0.01$  m s $^{-2}$  and  $\tau_0 = 0.106$  Nm $^{-2}$ . Figure A.8 illustrates the spin-up process from the state at rest. At the early stage, the southeast outcrop is created in addition to the well-known northwest outcrop. The former appears to be broader than the latter at  $t = 0.2$  because both zonal and Ekman drifts are inversely proportional to the Coriolis parameter. The northwest outcrop is elongated zonally at the early stage and compressed afterwards due to the Rossby wave propagation which depends on latitude. On the other hand, it enlarges monotonically in the meridional direction. We note that when the wind forcing is extremely strong, the southeast outcrop remains even in a steady state to conserve the total volume (cf. Bogue et al., 1986).

Figure A.9 shows the steady numerical solutions for  $h$  on a  $64 \times 64$  grid with the various flux or slope limiter methods listed in Table A.1. All schemes adopted here capture the interior layer successfully.<sup>4</sup> However, we can observe an overshooting of the western boundary current for (b), (d) and (e) of Fig. A.9 but not for the others.

<sup>4</sup>Yee's symmetric scheme is constructed by simplifying the TVD Lax-Wendroff method (see Table A.1). This is the reason why the numerical results for both schemes, Figs. A.9a and A.9c, are almost indistinguishable.

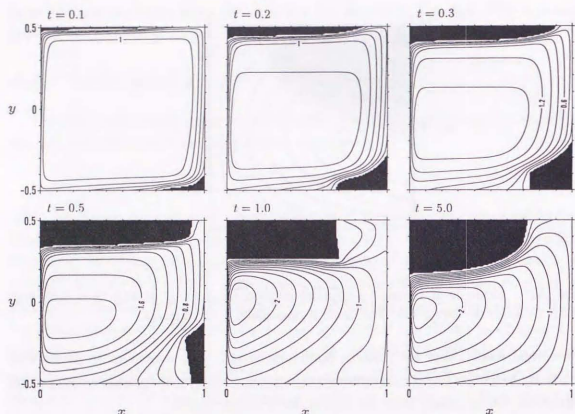


Figure A.8. Spin-up process for  $h$  calculated using Yee's symmetric TVD scheme on a  $128 \times 128$  grid. The nondimensional unit time corresponds to 4.6 yr. Contour interval is 0.2. The black region denotes the outcrop.

This nontrivial phenomenon is also reported by the previous workers using the FCT algorithm (e.g., Bogue et al., 1986), although our result for Pheonical SHASTA does not reveal any such signature.

In order to demonstrate whether such an overshooting is a physical property or not, Fig. A.10 compares the numerical solutions computed using Yee's upwind scheme but with various grid resolutions. A similar comparison is made for Pheonical SHASTA in Fig. A.11. Clearly, the overshooting shrinks as the resolution increases, and the gross features for the finest grid (Fig. A.10d) are in good qualitative agreement with those for Yee's symmetric scheme (Fig. A.9a). Thus, it is natural to consider that the overshooting is a numerical property due to the effect of artificial steepening possibly inherent of Yee's upwind scheme. We find from Fig. A.10 that Yee's upwind scheme requires a higher grid resolution than expected from the friction coefficient  $\epsilon$ ; this is also true for Chakravarthy-Osher and TVD MUSCL methods (not shown). This numerical property must be kept in mind when the inertial effects are taken into account with a coarse grid (cf. Cloke and Cullen, 1994). Obviously, Yee's symmetric scheme is more suitable than Yee's upwind scheme to reproduce the overall qualitative features of a

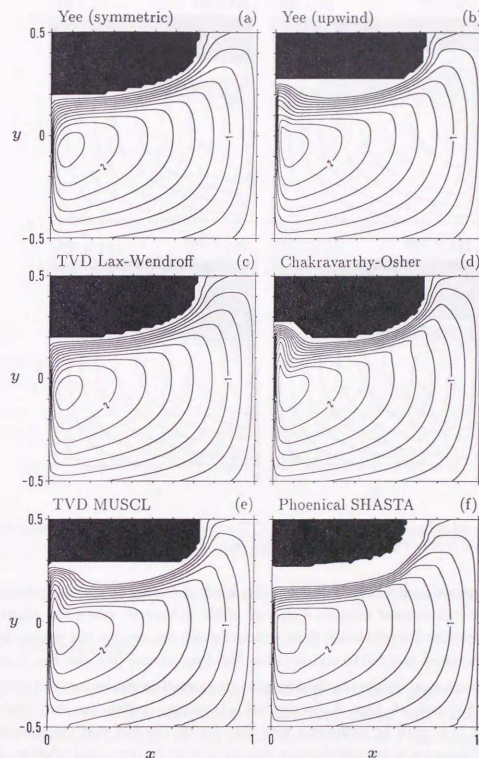


Figure A.9. Numerical solutions for  $h$  for  $\beta = 0.55$ ,  $\lambda = 0.53$  and  $\epsilon = 0.01$  on a  $64 \times 64$  grid calculated using the various schemes listed in Table A.1. Contour interval is 0.2. The black region denotes the outcrop.



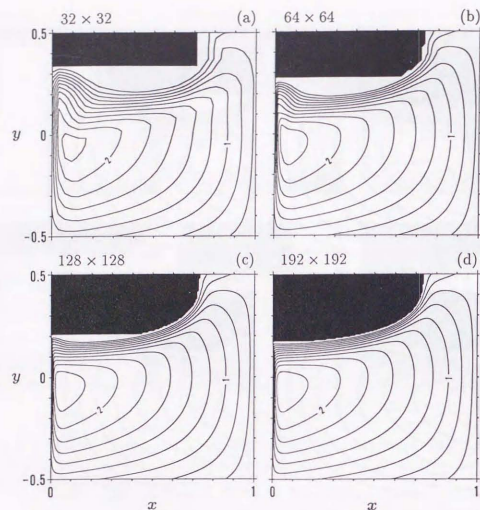


Figure A.10. As in Fig. A.9 for Yee's upwind TVD scheme but with various grid resolutions. Contour interval is 0.2. The black region denotes the outcrop.

solution in Parsons' model when a coarse grid is used. This may be associated to some extent with the unpleasant diffusive character of the symmetric scheme as shown in the previous section. Paradoxically, those schemes which can capture the interior layer sharply with a coarse grid fail to represent the Sverdrup interior (see also Fig. A.11a).

Since our numerical results are considered to give a good approximate solution with a sufficiently fine grid (cf. Figs. A.10d and A.11d), we may confirm the analytical solution (Fig. A.7) in turn by comparing with Fig. A.10d. We find that the composite expansion of Parsons is in good qualitative agreement with the numerical solution. The most discernible discrepancy, however, is the separation latitude as expected. Generally, the interior layer of the numerical solution emanates from a higher latitude than that of the analytical solution. This suggests that the simple composite expansion which consists of (A.14)–(A.16) does not describe the separation of the western boundary layer correctly. We may include, for instance, a corner layer around the separation

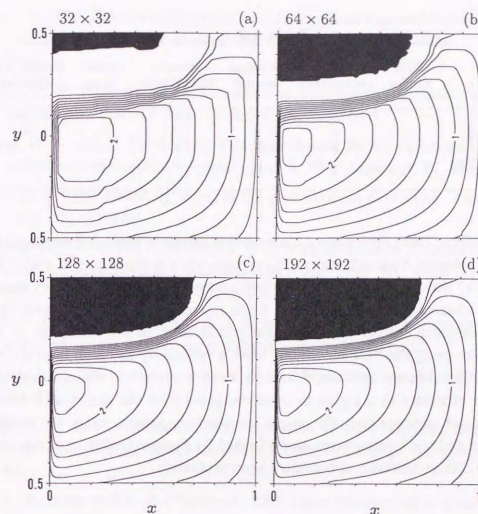


Figure A.11. As in Fig. A.9 for Phocional SHASTA but with various grid resolutions. Contour interval is 0.2. The black region denotes the outcrop.

point to improve the analytical solution (cf. Kamenkovich and Reznik, 1972).

## A.6 Conclusions

Various TVD schemes in Table A.1 are applied to a 1.5-layer planetary geostrophic model and are successful in representing the outcropping lower layer numerically.

Two preliminary experiments concerning the evolution of a conceptual planetary eddy and the spin-up of an equatorial ocean confirm that Yee's (both symmetric and upwind) schemes capture the propagation of the baroclinic long Rossby wave reasonably well. It is also verified that the symmetric scheme is slightly more diffusive than the upwind scheme.

These TVD schemes can reproduce a subtropical gyre with narrow interior jets. The numerical solutions are in good qualitative agreement with the analytical solution

Table A.2

Scheme	CFL number	Volume conservation	Sverdrup interior	Western bound. layer	Interior layer	Bound. layer separation
Yee (symmetric)	+	+	+	-	-	+
Yee (upwind)	+	+	+	+	+	-
Phoenical SHASTA	-	-	-	+	+	+

derived by Parsons (1969) even when a coarse grid is adopted. Table A.2 compares the three selected schemes from different points of view when a coarse grid is used. The scheme with (+) has an advantage over the scheme with (-) in regard to each aspect. As for Yee's schemes, the upwind scheme tends to create a spurious overshooting of the western boundary current when a coarse grid is used, as has been met by the previous workers using the FCT algorithm. With a sufficiently fine grid, however, the numerical solutions become indistinguishable from each other; the western boundary layer generally separates at a higher latitude compared with the analytical solution. This disagreement suggests that the simple composite expansion using the western boundary layer and the interior layer, as performed by Parsons (1969), does not seem to provide the correct behavior of boundary layer separation.

## References

- Bogue, N. M., R. X. Huang, and K. Bryan. 1986. Verification experiments with an isopycnal coordinate ocean model. *J. Phys. Oceanogr.* **16**, 985-990.
- Book, D. L., J. P. Boris, and K. Hain. 1975. Flux-corrected transport II: Generalizations of the method. *J. Comput. Phys.* **18**, 248-283.
- Boris, J. P. and D. L. Book. 1973. Flux-corrected transport I: SHASTA, a fluid-transport algorithm that works. *J. Comput. Phys.* **11**, 38-69.
- Chassignet, E. P. 1995. Vorticity dissipation by western boundary currents in the presence of outcropping layers. *J. Phys. Oceanogr.* **25**, 242-255.
- Cloke, P. and M. J. P. Cullen. 1994. A semi-geostrophic ocean model with outcropping. *Dyn. Atmos. Oceans* **21**, 23-48.
- Harten, A. 1983. A high resolution scheme for the computation of weak solutions of hyperbolic conservation laws. *J. Comput. Phys.* **49**, 357-393.
- Hirsch, C. 1990. *Numerical Computation of Internal and External Flows, Vol. II: Computational Methods for Inviscid and Viscous Flows*. John Wiley & Sons, Chichester.
- Huang, R. X. 1986. Numerical simulation of wind-driven circulation in a subtropical/subpolar basin. *J. Phys. Oceanogr.* **16**, 1635-1650.
- Huang, R. X. and G. Flierl. 1987. Two-layer models for the thermocline and current structure in subtropical/subpolar gyres. *J. Phys. Oceanogr.* **17**, 872-884.
- Ierley, G. R. 1990. Boundary layers in the general ocean circulation. *Ann. Rev. Fluid. Mech.* **22**, 111-142.
- Kamenkovich, V. M. and G. M. Reznik. 1972. A contribution to the theory of stationary wind-driven currents in a two-layer liquid. *Izv. Acad. Sci. USSR Atmos. Oceanic Phys.* (English translation) **8**, 238-245.
- Myers, P. G., A. F. Fanning, and A. J. Weaver. 1996. JEBAR, bottom pressure torque and Gulf Stream separation. *J. Phys. Oceanogr.* **26**, 671-683.
- Parsons, A. T. 1969. A two-layer model of Gulf Stream separation. *J. Fluid Mech.* **39**, 511-528.
- Sakamoto, T. and T. Yamagata. 1997. Evolution of baroclinic planetary eddies over localized bottom topography in terms of JEBAR. *Geophys. Astrophys. Fluid Dyn.* **84**, 1-27.
- Sun S., R. Bleck, and E. P. Chassignet. 1993. Layer outcropping in numerical models of stratified flows. *J. Phys. Oceanogr.* **23**, 1877-1884.
- Toro, E. F. 1997. *Riemann Solvers and Numerical Methods for Fluid Dynamics*. Springer, Berlin Heidelberg.
- van Albada, G. D., B. van Leer, and W. W. Roberts, Jr. 1982. A comparative study of computational methods in cosmic gas dynamics. *Astron. Astrophys.* **108**, 76-84.
- van Leer, B. 1979. Towards the ultimate conservative difference scheme, V. A second order sequel to Godunov's method. *J. Comput. Phys.* **32**, 101-136.
- van Leer, B. 1997. ICASE and the history of high-resolution schemes. In: *Upwind and High-Resolution Schemes* (M. Y. Hussaini, B. van Leer and J. V. Rosendale, eds.), pp. 1-7. Springer, Berlin Heidelberg.
- Yee, H. C. 1987. Construction of explicit and implicit symmetric TVD schemes and their applications. *J. Comput. Phys.* **68**, 151-179.



## PART II

### OTHER PROBLEMS

The first problem is the question of the validity of the results of the experiments. It is well known that the results of the experiments are only valid if the conditions of the experiment are the same as the conditions of the real world. In the case of the experiments on the effect of the environment on the development of the child, the conditions of the experiment are not the same as the conditions of the real world. The child is in a laboratory, and the environment is controlled. This is not the same as the child in the real world, where the environment is not controlled. Therefore, the results of the experiments are only valid if the conditions of the experiment are the same as the conditions of the real world.

The second problem is the question of the validity of the results of the experiments. It is well known that the results of the experiments are only valid if the conditions of the experiment are the same as the conditions of the real world. In the case of the experiments on the effect of the environment on the development of the child, the conditions of the experiment are not the same as the conditions of the real world. The child is in a laboratory, and the environment is controlled. This is not the same as the child in the real world, where the environment is not controlled. Therefore, the results of the experiments are only valid if the conditions of the experiment are the same as the conditions of the real world.

The third problem is the question of the validity of the results of the experiments. It is well known that the results of the experiments are only valid if the conditions of the experiment are the same as the conditions of the real world. In the case of the experiments on the effect of the environment on the development of the child, the conditions of the experiment are not the same as the conditions of the real world. The child is in a laboratory, and the environment is controlled. This is not the same as the child in the real world, where the environment is not controlled. Therefore, the results of the experiments are only valid if the conditions of the experiment are the same as the conditions of the real world.

## Chapter 3

### Potential vorticity homogenization in a two-layer wind-driven gyre

#### 3.1 Introduction

A series of theoretical works on the wind-driven ocean circulation has been devoted so far to demonstrate various mechanisms which produce flows in the Sverdrup interior of a submerged (or unventilated) lower layer. It is known that a region of closed geostrophic contours appears in the lower layer when external wind forcing is so strong that vertical vortex stretching is comparable to the planetary  $\beta$ -effect. A similar situation is also realized when bottom topography is of sufficient magnitude. Since those contours correspond also to the characteristics of wave propagation, the closed region is not influenced by baroclinic Rossby waves excited at the eastern boundary; the flow in the region cannot be compensated. The motion in this region may be determined internally, so that an unexpected transport may be allowed, for example, by vertical momentum transfer (Welander, 1968).

The first quantitative theory of Rhines and Young (1982) (hereafter referred to as RY) and most of the succeeding works are based on the quasigeostrophic dynamics (Rhines, 1986; Young, 1987). RY adopted two-layer quasigeostrophic potential vorticity equations with weak interfacial and bottom frictions. The interior was assumed to be inviscid at the leading order approximation, so that details of the lower-layer flow was determined globally using the Prandtl-Batchelor theorem within closed geostrophic contours. It turned out that the lower-layer streamfunction and the potential vorticity are related by a linear functional. One of the important consequences of their theory is homogenization of the lower-layer potential vorticity in the closed region. Vertical eddy viscosity parameterized as the interfacial and bottom frictions was considered first to be a candidate for smearing the gradient of potential vorticity; the effective viscosity is, however, increased by shearing motions (Rhines and Young, 1983; Dewar et al., 1984).

The seminal theory of potential vorticity homogenization developed by RY was tested in the North Pacific (e.g., Talley, 1988), in the North Atlantic (e.g., McDowell



et al., 1982) and in the world ocean (Keffer, 1985) for a relatively thin layer between layers influenced by strong ventilation and subduction. The updated observational maps for the North Pacific are presented in Appendix 2 of Part I. We note also that chemical tracer concentrations are governed by an advection-diffusion equation similar to the potential vorticity equation. It is found, using a single-layer model closed by a frictional western boundary current, that the tracer distribution tends to be uniform in the interior for high Péclet numbers (e.g., Musgrave, 1985; 1990). Salmon (1994) recently constructed an elaborate thermocline model based on the *a priori* assumption that potential vorticity is uniform on each isopycnal surface; his model retains many advantages of two-layer planetary geostrophic dynamics.

Ierley and Young (1983) (hereafter referred to IY) gave a quasigeostrophic theory which discussed the case in which a closed streamline passes the frictional western boundary layer. In particular, the interior solution for the lower layer in the out-flow region is not determined other than one-way matching with an assumed Stommel layer due to the overdetermined nature of the intermediate region. Thus, the interior is entirely controlled by the western boundary layer, and potential vorticity homogenization is not realized. Their argument appears to be reasonable because the Sverdrup interior in the lower layer is always exposed to the frictional boundary layer to which the Prandtl-Batchelor theorem cannot be applied. Furthermore, Jarvis and Veronis (1994) have recently confirmed numerically, using steady, two-layer planetary geostrophic equations, that the lower-layer potential vorticity cannot be uniform in the steady state. However, Huang (1987) discussed potential vorticity homogenization in a double-gyre basin using a 2.5-layer planetary geostrophic model and showed a tendency toward homogenization in the eastern submerged interior, straddling both subtropical and subpolar gyres. Surprisingly, we have shown in Chapter 2 that for the limited parameter regime a region of uniform potential vorticity may still be established in the western pool region which may be ventilated to the north. The latter two works strongly stimulate the present study.

The simple theory of IY was followed by more complicated models to focus on the role of relative vorticity, including the full quasigeostrophic models (e.g., Holland et al., 1984; Dewar et al., 1984; Dewar, 1989) and the primitive models (e.g., Cox and Bryan, 1984; Cox, 1985). In those model results, a broad region of uniform potential vorticity, though in varying degrees of uniformity, is realized due to vigorous eddy activities. Although many previous workers are concerned with the Sverdrup interior, Lozier and Riser (1989) and Rhines and Schopp (1991) investigated the effect of the western boundary current on the homogenization processes using a full quasigeostrophic model. However, those highly inertial models do not provide a convincing proof for the basic theories of RY and IY [see also Bryan (1987)].

Therefore, the problem of potential vorticity homogenization is still controversial

due to the existence of the western boundary layer. This is in fact one of the inherent difficulties met in both ventilated and unventilated thermocline theories (see Pedlosky, 1990). In this chapter, we will suggest a possible closure of this question by searching for such a mechanism that the western boundary layer is relatively ineffective in the evolution of potential vorticity in the interior. For this purpose, two-layer quasigeostrophic equations are adopted due to mathematical tractability. Moreover, the nonlinear advection terms are omitted to give direct arguments in the framework of RY and IY. Numerical solutions for steady states are presented first in Section 3.3. Then, we discuss the homogenization mechanism for this simplified system in terms of the initial-value problem, with a particular attention to the interior in Section 3.4. The structure of the viscous western boundary layer is examined as the steady problem in Section 3.5. In Section 3.6, a more realistic, planetary geostrophic model is treated numerically to show the utility of the present quasigeostrophic model.

### 3.2 Model equations and numerical method

Consider a two-layer fluid in a square basin on a  $\beta$ -plane ranging  $0 \leq x \leq 1$  and  $-0.5 \leq y \leq 0.5$  in nondimensional unit (see below for the scaling). The central latitude of this plane is taken to be a reference latitude, so the Coriolis parameter is  $f = f_0 + \beta_0 y$  in dimensional form. The governing equations without the nonlinear advection terms are, in dimensionless form,

$$[\omega \nabla^2 \psi_1 + F(\psi_2 - \psi_1)]_1 + J(\psi_1, q_1) = \nu \nabla^2(\psi_2 - \psi_1) - \tau_y^x, \quad (3.1)$$

$$[\omega \nabla^2 \psi_2 + \frac{F}{\alpha}(\psi_1 - \psi_2)]_1 + J(\psi_2, q_2) = \frac{\nu}{\alpha} \nabla^2(\psi_1 - \psi_2) - \frac{\delta}{\alpha} \nabla^2 \psi_2, \quad (3.2)$$

$$q_1 = y + F(\psi_2 - \psi_1), \quad (3.3)$$

$$q_2 = y + \frac{F}{\alpha}(\psi_1 - \psi_2), \quad (3.4)$$

with the boundary condition

$$\psi_n = 0 \quad \text{at all solid boundaries}, \quad (3.5)$$

where  $\psi_n$  is the  $n$ th-layer streamfunction,  $q_n$  is the potential vorticity, and

$$\tau^x = \sin \pi y \quad (3.6)$$

is the steady zonal wind forcing, modeling the subtropical winds. In the above equations, the following scaling parameters have been kept in mind: the basin width  $L$ , the layer thickness at rest  $D_n$ , the baroclinic radius of deformation  $L_D$ , and the Sverdrup speed  $u_S$ . The latter two quantities are represented by

$$L_D = \frac{f_0 L}{g' D_1}, \quad u_S = \frac{\tau_0}{\rho_0 \beta_0 L D_1}, \quad (3.7)$$

respectively. The interfacial and bottom frictions are parameterized as a simple drag with dimensional coefficients  $R$  and  $K$ . The nondimensional parameters are defined as follows:

$$\begin{aligned} F &= \frac{f_0^2 \tau_0}{\rho_0 g' \beta_0^2 L D_1^2} = O(1), \\ \alpha &= \frac{D_2}{D_1}, \\ \omega &= F \left( \frac{L_D}{L} \right)^2 = \frac{\tau_0}{\rho_0 \beta_0^2 L^3 D_1} \ll 1, \\ \nu &= \frac{R}{\beta_0 L D_1}, \\ \delta &= \frac{K}{\beta_0 L D_1}. \end{aligned} \quad (3.8)$$

The controlling parameters are  $F$  and  $\alpha$ , each of which measures the nonlinearity due to vertical vortex stretching associated with the wind strength and the lower-layer thickness, respectively, and  $\omega$  is considered to be dependent on  $F$ . The friction coefficients are chosen to be  $\nu = 0.01$  and  $\delta = 0.01$  except for Fig. 3.10, but the dissipation rate may be varied by changing  $\alpha$ . The nonlinear advection terms have been neglected in (3.1)–(3.2) as already mentioned, whereas the linear acceleration terms multiplied by  $\omega$  are retained just for the convenience of time integration. The main effect of the linear acceleration terms is the existence of short Rossby waves generated at the western boundary, but these waves decay rapidly due to damping.

To calculate a steady solution numerically, we actually solve barotropic and baroclinic equations in place of (3.1)–(3.2). Introducing barotropic and baroclinic streamfunctions as

$$\Psi = \psi_1 + \alpha \psi_2, \quad (3.9)$$

$$\eta = \psi_2 - \psi_1, \quad (3.10)$$

respectively, and rewriting (3.1)–(3.2) in terms of  $\Psi$  and  $\eta$ , we have

$$\omega \nabla^2 \Psi_t + \Psi_x = -\tau_y^x - \frac{\delta}{H} \nabla^2 (\Psi + \eta), \quad (3.11)$$

$$\left( \omega \nabla^2 - \frac{H}{\alpha} F \right) \eta_t + \eta_x = \frac{H}{\alpha} F J(\Psi, \eta) + \tau_y^x - \frac{H}{\alpha} \nu \nabla^2 \eta - \frac{\delta}{\alpha H} \nabla^2 (\Psi + \eta), \quad (3.12)$$

where  $H = 1 + \alpha$  is the constant total depth. Eqs. (3.11)–(3.12) are integrated on a regular grid by the leapfrog time stepping until a steady state is reached. The grid resolution is  $128 \times 128$  unless otherwise stated. The Poisson and Helmholtz equations which arise in the calculation procedure are solved by the Fourier sine transform method with the FFT algorithm. No artificial viscosity is adopted in the present experiment.

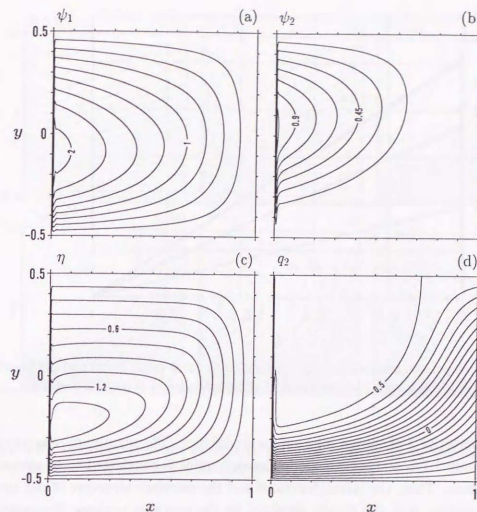


Figure 3.1. Steady-state solutions of the two-layer quasigeostrophic equations for  $F = 0.5$ ,  $\alpha = 1$  in the steady state: (a)  $\psi_1$ , (b)  $\psi_2$ , (c)  $\eta$ , (d)  $q_2$ . Contour intervals are (a) 0.25, (b) 0.15, (c) 0.15, (d) 0.05, respectively.

### 3.3 Numerical results

We first present a remarkable case of  $F = 0.5$ ,  $\alpha = 1$ . Figure 3.1 shows the steady solutions for the streamfunctions  $\psi_1$ ,  $\psi_2$ , the interface displacement  $\eta$  and the lower-layer potential vorticity  $q_2$ . A pool region (or closed region) defined as an area surrounded by such geostrophic contours [see (3.14)] that do not emanate from the eastern boundary occupies the major part of the basin; the lower layer is in motion over this subdomain. Figure 3.2 compares the numerical result for the total streamfunction with the Sverdrup transport given by

$$\Psi^I = (1-x)\pi \cos \pi y, \quad (3.13)$$



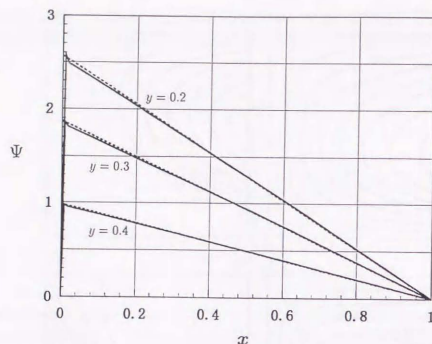


Figure 3.2. Comparison between the numerical solution for  $\Psi$  (solid lines) and the Sverdrup transport  $\Psi = (1-x)\pi \cos \pi y$  (dashed lines) at three latitudes,  $y = 0.2, 0.3$  and  $0.4$ .

where the superscript  $I$  denotes a solution for the interior. The maximum relative error at  $y = 0.2$  is only 1.7%, so that our model ocean interior is considered to be almost in Sverdrup balance. Thus, the streamfunctions and the interface structure of our model result are consistent with the results obtained by the previous workers. Surprisingly, however, the distribution of  $q_2$  appears to be very uniform even in the presence of the frictional western boundary current. This particular case corresponds, for instance, to the following ambient parameters:  $L = 2500$  km,  $f_0 = 7.3 \times 10^{-5} \text{ s}^{-1}$ ,  $\beta_0 = 2 \times 10^{-11} \text{ m}^{-1} \text{ s}^{-1}$ ,  $\rho_0 = 1000 \text{ kg m}^{-3}$ ,  $g' = 0.01 \text{ m s}^{-2}$ ,  $\tau_0 = 0.1 \text{ Nm}^{-2}$ , and  $D_1 = 326$  m. We can say that this set of parameters is by no means unrealistic.

For comparison, Fig. 3.3 shows the distribution of  $q_2$  but for various values of  $F$  ( $\alpha$  is fixed at 1), while Fig. 3.4 shows similar maps for three values of  $\alpha$  ( $F$  is fixed at 1). It is immediately found that  $q_2$  is very sensitive to these parameters. For the case of weak vortex stretching (Figs. 3.3a and 3.4c), no closed region is formed, and the lower layer is motionless except in the thin western boundary layer (not shown); these cases approximately belong to Welander's regime (Welander, 1966). When vortex stretching is moderate (Figs. 3.3b, 3.3c and 3.4b), the isolines are strongly bent to create a region of small gradients in the northern part of the basin. When vortex stretching is strong (Figs. 3.3c and 3.3f), however, a new maximum of  $q_2$  appears in the western part of the pool, and the distribution is no longer uniform there. At this stage, we suggest from the numerical solutions that a region of uniform potential vorticity is realized

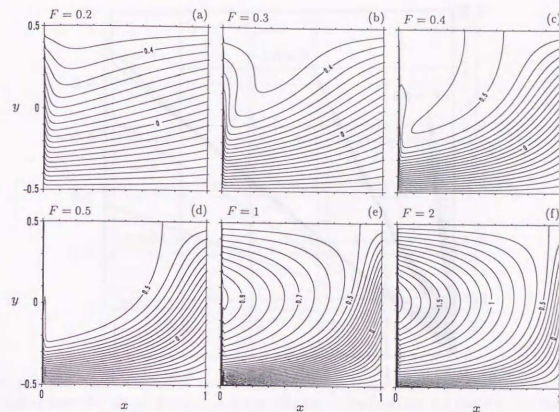


Figure 3.3. Distribution of the lower-layer potential vorticity  $q_2$  for various values of  $F$  ( $\alpha = 1$ ). Contour intervals are (a)–(c) 0.05, (f) 0.1, respectively.

when  $F/\alpha < 1$ , i.e., vortex stretching is not very strong. We will clarify more distinct physical meanings of this inequality in the next two sections.

Before proceeding, a comparison is made between our numerical solution and IY's analytical solution which is assumed to be of the form  $\psi_2^I = G(q^I)$  within the closed

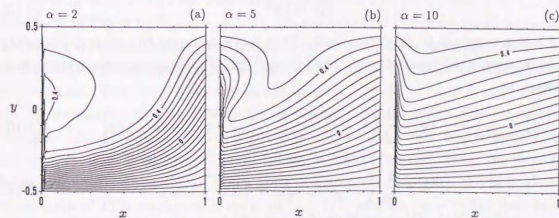


Figure 3.4. As in Fig. 3.3 but for different values of  $\alpha$  ( $F = 1$ ). Contour interval is 0.05.

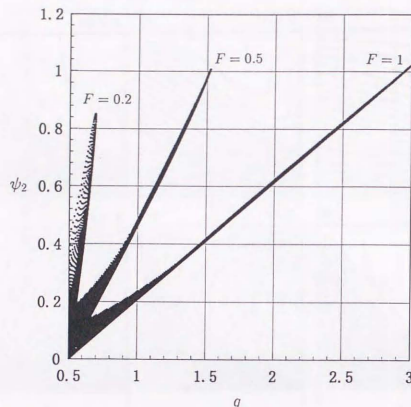


Figure 3.5. Scatter diagram between  $q$  (abscissa) and  $\psi_2$  (ordinate) in the pool region for  $\alpha = 1$  with  $F$  varied.

geostrophic contours, where

$$q = y + \frac{F}{\alpha} \Psi \quad (3.14)$$

whose isolines are geostrophic contours. To determine the function  $G$ , they matched this interior solution with the western boundary layer solution  $\psi_2^B$  (where the superscript  $B$  denotes a solution for the western boundary layer) under the crucial assumption that

$$\psi_2^B = \lambda \Psi^B, \quad (3.15)$$

where  $\lambda$  is a constant to be determined. That is, IY assumed the western boundary layer to be simply of Stommel type. The leading term of their asymptotic solution may be written as

$$\psi_2^I = \frac{\pi^2 \lambda}{\pi^2 F - \alpha} \left( q^I - \frac{1}{2} \right) = \frac{\pi^2 \lambda}{\pi^2 F - \alpha} \left[ y - \frac{1}{2} + \frac{F}{\alpha} (1-x) \pi \cos \pi y \right], \quad (3.16)$$

where

$$\lambda = \frac{1}{2\alpha} \left( 1 + \gamma H - \sqrt{(1 + \gamma H)^2 - 4\gamma\alpha} \right) \quad (3.17)$$

with  $\gamma = \nu/\delta = O(1)$ . IY claim that (3.16) should be applied in the outflow region where the flow leaves the western boundary layer. Following IY, the condition for

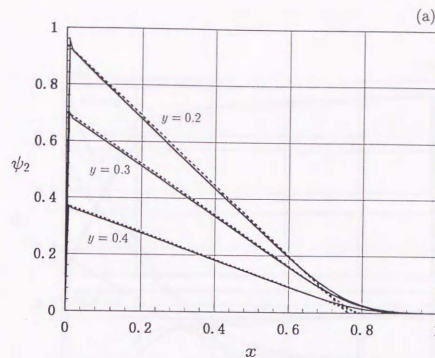


Figure 3.6. (a) Comparison between the numerical (solid lines) and analytical solution (dashed lines) for  $\psi_2$  for  $F = 0.5$ ,  $\alpha = 1$  at three latitudes,  $y = 0.2, 0.3$  and  $0.4$ . (b) Similar comparison for  $q_2$ .

which a geostrophic contour is closed is given by

$$\frac{F}{\alpha} > \frac{1}{\pi^2} \approx 0.1013, \quad (3.18)$$

which indicates that the denominator of the coefficient of (3.16) is always positive. It turns out from (3.16) that IY's solution asymptotically gives a linear relationship between  $q^I$  and  $\psi_2^I$ , which is in good qualitative agreement with our numerical results (Fig. 3.5).

Figure 3.6 compares (3.16) with our numerical solutions for  $\psi_2$  and  $q_2$  for the interesting case of Fig. 3.1 ( $F = 0.5$ ,  $\alpha = 1$ ). We note that all the three zonal sections are located in the outflow region. Both solutions are in remarkably good agreement except for the derivative layer seen in the numerical solution for  $q_2$ , although this agreement is exceptional. Two more comparisons are made in Fig. 3.7 ( $F = 0.2$ ,  $\alpha = 1$ ;  $F = 2$ ,  $\alpha = 1$ ); we can see a noticeable disagreement between the analytical and numerical solutions. The maximum relative error of  $\psi_2^I$  at  $y = 0.2$  is now 13.3% for Fig. 3.7a, and 9.4% for Fig. 3.7b, respectively. Thus, in the latter two cases, the first term of the asymptotic expansion is not a good approximate solution. We note that the second term of IY's expansion is cubic in  $(q - 1/2)$  and its ratio to the first term is  $[3\pi(\pi^2 F - \alpha)^2]^{-1}$  which decreases rapidly as  $F$  increases (e.g.,  $1.6 \times 10^{-5}$  for  $F = 2$ ,  $\alpha = 1$ ); the analytical solution would not be greatly improved by adding higher order



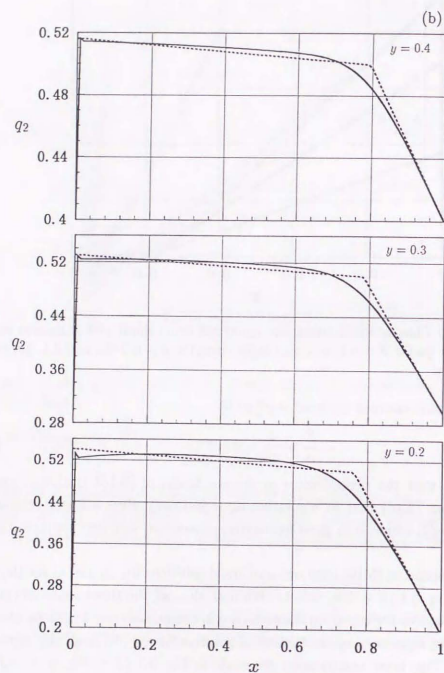
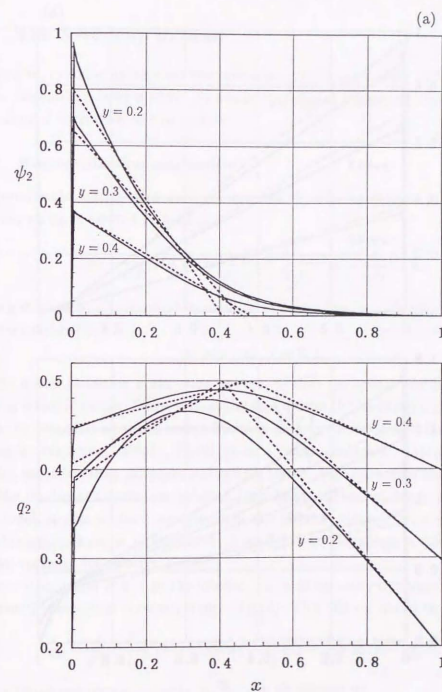


Figure 3.6. (Continued.)

Figure 3.7. (a) As in Fig. 3.6 but for  $F = 0.2$ ,  $\alpha = 1$ . (b) As in Fig. 3.6 but for  $F = 2$ ,  $\alpha = 1$ .

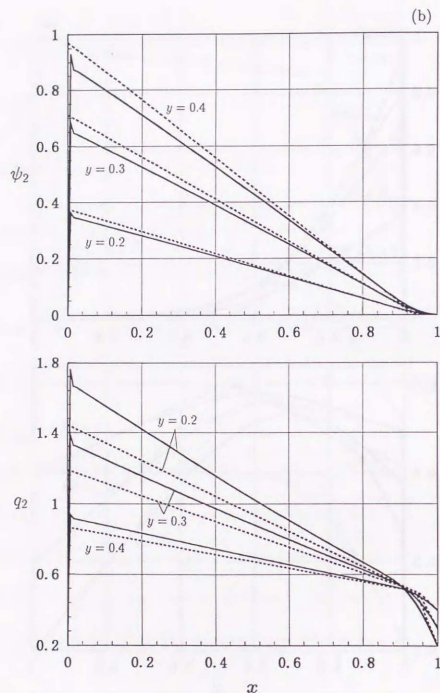


Figure 3.7. (Continued.)

terms. Therefore, it appears that the discrepancy seen in Fig. 3.7 originates in the *a priori* assumption of (3.15). We will return to this problem in Section 3.5.

### 3.4 The Sverdrup interior

Here, we examine under what circumstances potential vorticity will be homogenized in the present two-layer system. Attention is focused mainly on the interior, so the superscript *I* is omitted in this section.

#### 3.4.1 Homogenization mechanism

Consider the initial-value problem governed by the lower-layer potential vorticity equation which is derived from (3.2):

$$q_{2t} + \frac{\alpha}{FH} J(q, q_2) = \frac{1}{F} \left( \nu + \frac{\delta}{H} \right) \nabla^2 q_2 - \frac{\delta}{\alpha H} \nabla^2 \Psi, \quad (3.19)$$

where  $q$  is given by (3.14) and the small term multiplied by  $\omega$  has been omitted. The boundary condition is

$$q_2 = y \quad \text{at } x = 0, 1, \quad (3.20)$$

and the initial condition is the state at rest, so that the initial profile of  $q_2$  coincides with the latitude circles. Since  $\Psi$  is established during the barotropic adjustment time, it may be regarded as a prescribed function as long as the entire baroclinic spin-up process is concerned. Hence, (3.19) gives a linear evolution equation for  $q_2$  which includes the advection, diffusion and source terms. The advection term is associated with the nonlinear interaction between both layers. The last term of (3.19), on the other hand, inputs positive vorticity over the interior, since  $\nabla^2 \Psi = -\pi^2 \Psi$ . We note that this source term is multiplied by  $\delta$  as if the bottom plays a role of a source of positive vorticity (cf. Huang, 1988).

Since  $\nu \ll 1$  and  $\delta \ll 1$  in the interior, the leading order dynamics is governed by the advection equation corresponding to (3.19). This can be rewritten as

$$q_{2t} + \frac{\alpha}{FH} \left[ \frac{F}{\alpha} \pi^2 (1-x) \sin \pi y - 1 \right] q_{2x} - \frac{1}{H} \pi \cos \pi y \cdot q_{2y} = 0, \quad (3.21)$$

whence the characteristic velocity  $(u_c, v_c)$  can be defined by

$$u_c = \frac{\alpha}{FH} \left[ \frac{F}{\alpha} \pi^2 (1-x) \sin \pi y - 1 \right], \quad (3.22)$$

$$v_c = -\frac{1}{H} \pi \cos \pi y. \quad (3.23)$$

Obviously,  $u_c$  represents the competition between the zonal Sverdrup flow and the baroclinic long Rossby wave, while  $v_c$  denotes the advection due to the southward Sverdrup



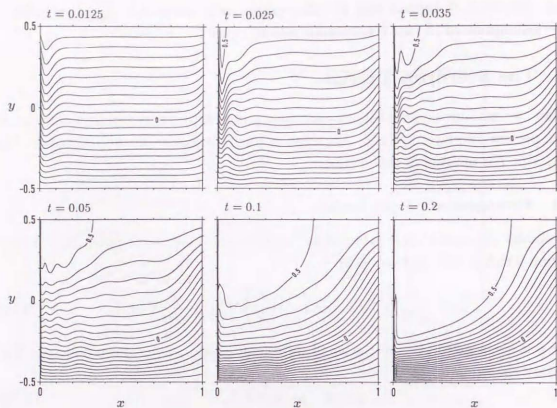


Figure 3.8. Evolution of  $q_2$  for  $F = 0.5$ ,  $\alpha = 1$ . The nondimensional unit time corresponds to 5.4 yr. Contour interval is 0.05.

flow. Therefore, the "flow" associated with this characteristic velocity just advects  $q_2$ -contours southward, so that a gap will be left north of the northernmost  $q_2$ -contour. This opening should be filled with the uniform potential vorticity provided that any new maxima or minima in  $q_2$  are not created. Since the western boundary layer, which is only implicit here, may enhance the value of  $q_2$  in the interior, this condition is satisfied if the wave drag is sufficiently strong that the zonal characteristic speed  $u_c$  is westward; i.e., if

$$\frac{F}{\alpha} \pi^2 (1-x) \sin \pi y - 1 \leq 0 \quad (3.24)$$

at a point, then information on  $q_2$  cannot propagate east of this point. Obviously, (3.24) becomes more restrictive as the western or northern wall is approached. For convenience, on averaging (3.24) at  $x = 0$  over the northern half basin, we have the following inequality:

$$\frac{F}{\alpha} \leq \frac{2}{\pi} \approx 0.637. \quad (3.25)$$

Figure 3.8 shows the evolution of  $q_2$  for the case of  $F = 0.5$ ,  $\alpha = 1$  (cf. Fig. 3.1) which satisfies (3.25) as expected. The pool region appears to be unaffected by the western boundary layer because no new extrema in  $q_2$  are created in the pool. This is in clear

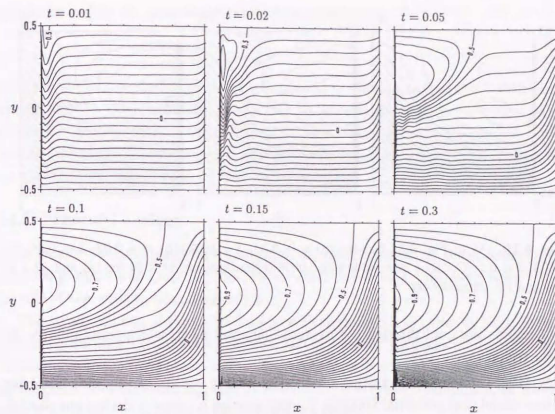


Figure 3.9. As in Fig. 3.8 but for  $F = 1$ ,  $\alpha = 1$ . The nondimensional unit time corresponds to 8.3 yr. Contour interval is 0.05.

contrast to the  $F = 1$  case (Fig. 3.9), in which a maximum is immediately produced near the western boundary and its influence rapidly spreads eastward.

It is confirmed from both cases (Figs. 3.8 and 3.9) that the pool region reaches a stationary state as quickly as the outer compensated region does, although the former does not belong to the Sverdrup regime. The evolution of the latter region is well characterized by the baroclinic spin-up time  $T_s$  defined using (3.21) by

$$T_s = \frac{1}{c} = \frac{FH}{\alpha}, \quad (3.26)$$

where  $c$  is the speed of the linear baroclinic long Rossby wave. If we define the advection time  $T_a$  similarly from (3.21) by

$$T_a = \frac{2}{\pi} H_i, \quad (3.27)$$

where the factor  $2/\pi$  is multiplied only for convenience, then (3.25) reads

$$T_s < T_a. \quad (3.28)$$

This inequality may be interpreted in relation to homogenization as follows. Unless a stationary state is achieved within  $T_a$ , a  $q_2$ -contour frozen to particles with the velocity

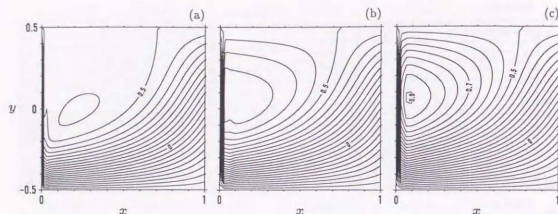


Figure 3.10. As in Fig. 3.3d but for (a)  $\nu = 0.02$ ,  $\delta = 0.02$ , (b)  $\nu = 0.03$ ,  $\delta = 0.05$ , (c)  $\nu = 0.03$ ,  $\delta = 0.1$ . Contour interval is 0.05. Grid resolutions are  $64 \times 64$  for (a) and  $32 \times 32$  for (b) and (c), respectively.

$(u_e, v_e)$  rounds the pool through the western boundary layer, which contaminates the uniform region.

Cox (1985) made an interesting observation in the results of the eddy resolving primitive model that potential vorticity homogenization is completed after one particle circuit of the gyre, so that the time scale of homogenization is much shorter than diffusion time. From the above argument based on the simple model, we suggest that the large-scale wave drag plays an important role in such more realistic ocean models; retardation of advective motions by the baroclinic Rossby repeller may greatly enhance the effective eddy mixing (cf. Rhines and Young, 1983).

To complete the discussion of the initial-value problem, we must take into account the source and sink terms on the right-hand side in (3.19) which have been neglected so far. The sink term is of the form of simple diffusion and hence plays a role in smearing the gradients of  $q_2$  in a trivial manner. Since  $\nu \ll 1$  and  $\delta \ll 1$ , this process is expected to be very weak outside the western boundary layer in the present numerical results. The effect of the source term in (3.19), on the other hand, is accumulated in the course of equilibration. The vorticity input piled up during  $T_s$  may be evaluated as  $\pi^2(F/\alpha)(\delta/\alpha)$ . Hence, we obtain another constraint on  $F/\alpha$  for the source term not to erode the uniformity of  $q_2$ :

$$\frac{F}{\alpha} \ll \frac{\alpha}{\pi^2 \delta}, \quad (3.29)$$

which is satisfied in the present experiment. Conversely, when  $\delta$  is large of the order of 0.1, the system reaches a different steady state without homogenization as clearly shown in Fig. 3.10.

In summary, the two inequalities (3.25) and (3.29) may be combined into a possible

parameter regime for potential vorticity homogenization:

$$\frac{F}{\alpha} \leq \frac{2}{\pi}, \quad \frac{F\delta}{\alpha^2} \ll \frac{1}{\pi^2}. \quad (3.30)$$

We have already confirmed that this theoretical prediction is consistent with our numerical results. The inequality (3.18) may be appended as the lower bound of  $F/\alpha$ , although it merely denotes the requirement for a closed geostrophic contour. In Section 3.5, we propose an alternative view of the right inequality in (3.30) in relation to the western boundary layers.

### 3.4.2 Thermal analogy

In this preliminary subsection, intuitive arguments based on thermal analogy are provided to understand not only the interior distribution of potential vorticity but also the role of the western boundary layers.

The steady version of the potential vorticity equation (3.19) may be regarded as an equation governing a temperature distribution in a steady fluid flow represented by the "streamfunction"  $q$  (Welander, 1968). The temperature is fixed at a constant value at the northern boundary and increases linearly along the western boundary. In addition, there is an internal heat source which is always positive.

The temperature distribution in the interior is determined by the relative importance between convection and diffusion. If the heat source is small and convection is not so intense that (3.30) is the case, the north part of the interior is filled with the highest temperature at the northern boundary due to conduction however weak it may be, whereas the weak southward flow may intrude the region of lower temperature. Because of the predominance of the diffusive character, the western boundary layer for the temperature, which is needed to compensate for the western boundary condition, may be much wider than the flow boundary layer (cf. Figs. 3.3a–3.3d). Therefore, the temperature is allowed to increase gradually along the flow boundary layer from the value at the southern extreme of the flow to the higher homogenized value; the homogenized temperature can be maintained in the interior. If the convection is very strong, however, the temperature distribution in the interior is likely to follow the distribution of  $q$  (cf. Figs. 3.3c and 3.3f), whence, the temperature boundary layer must be formed inside the flow boundary layer. It is thus easily expected that the whole distribution of the temperature is strongly affected by the boundary current. The latter extreme case will be discussed in more detail in the next section.

### 3.5 The western boundary layer

To understand the requirement for potential vorticity homogenization, (3.25), in the context of the steady problem, we must shed light on the structure of the fric-



tional western boundary layer to utilize the notion of matching. As mentioned earlier, IY's assumption (3.15) leads to a Stommel problem for both  $\Psi$  and  $\psi_2$ . However, the apparent disagreement between their analytical solutions and our numerical solutions (Section 3.3) implies that the western boundary layer must be treated more carefully. Although we do not intend to solve the boundary layer equations in closed form, helpful information in this regard is obtained by discussing some special cases which are mathematically tractable.

Introducing a boundary layer coordinate  $X = x/\delta$  and then taking the limit  $\nu, \delta \rightarrow 0$  with  $X$  fixed, (3.11) and (3.2) lead to

$$\Psi_X^B = -\psi_{2XX}^B, \quad (3.31)$$

$$\psi_{2X}^B q_2^B - \psi_{2y}^B q_X^B = \frac{\gamma}{\alpha} \Psi_{XX}^B - \frac{1}{\alpha} (1 + \gamma H) \psi_{2XX}^B, \quad (3.32)$$

respectively. The boundary and matching conditions are

$$\Psi^B(X=0) = 0, \quad \psi_2^B(X=0) = 0, \quad (3.33)$$

$$\Psi^B(X \rightarrow \infty) = \Psi^I, \quad \psi_2^B(X \rightarrow \infty) = \psi_2^I, \quad (3.34)$$

where  $\Psi^I$  is given by (3.13) and  $\psi_2^I$  may be assumed to be of the form  $G(q^I)$  using an arbitrary function  $G$ . As for the potential vorticity dynamics, we should rewrite the boundary layer equations (3.31)–(3.32) in terms of  $\Psi$  and  $q_2$ ; rescaling  $x$  by  $\bar{x} = Hx/\delta$ , we have

$$\Psi_{\bar{x}}^B = -\Psi_{\bar{x}\bar{x}}^B - \frac{1}{F_2} q_{2\bar{x}\bar{x}}^B, \quad (3.35)$$

$$\frac{\alpha}{H} \frac{1}{F_2} (q_{2y}^B q_{2y}^B - q_y^B q_{2x}^B) = \frac{1}{F_2} (1 + \gamma) q_{2\bar{x}\bar{x}}^B - \Psi_{\bar{x}\bar{x}}^B, \quad (3.36)$$

where  $F_2$  stands for  $F/\alpha$ , corresponding to the baroclinic rotational Froude number for the lower layer. The boundary and matching conditions on  $q_2$  are

$$q_2^B(\bar{x}=0) = y, \quad q_2^B(\bar{x} \rightarrow \infty) = q_2^I. \quad (3.37)$$

Recall the relations

$$q = y + F_2 \Psi, \quad (3.38)$$

$$\psi_2 = \frac{\alpha}{H} \left[ \Psi + \frac{1}{F_2} (y - q_2) \right], \quad (3.39)$$

for later use.

We examine below two extreme cases: For  $F_2 \ll 1$ , the problem must be reduced to the case discussed by Welander (1966). In fact, (3.35) and (3.36) are reduced, as  $F_2 \rightarrow 0$ , to

$$q_{2\bar{x}}^B = 0, \quad (3.40)$$

which is solved by

$$q_2^B = y. \quad (3.41)$$

Of course, this is easily obtained also from (3.39). Substituting (3.41) back to (3.35), we confirm that  $\Psi^B$  is represented by a Stommel layer of width  $O(\delta)$ , and so is  $\psi_2^B$  from (3.31) or (3.39). On the other hand,  $q_2^B$  may be regarded as a boundary layer with an infinite width.

For the other extreme case,  $F_2 \gg 1$ , (3.39) is reduced to

$$\psi_2^B = \frac{\alpha}{H} \Psi^B, \quad (3.42)$$

which, with (3.9), simply means that the flow in the western boundary layer is barotropic (see also IY). Then, (3.31) gives a Stommel problem which is solved by

$$\Psi^B(\bar{x}, y) = (1 - e^{-\bar{x}}) \pi \cos \pi y. \quad (3.43)$$

However, more precise treatment is required for  $q_2^B$ , because (3.36) leads to another singular perturbation problem

$$\Psi_y^B q_{2x}^B - \Psi_x^B q_{2y}^B = \frac{H}{\alpha} \Psi_{\bar{x}\bar{x}}^B \quad (3.44)$$

in the limit  $F_2^{-1} \rightarrow 0$ . We find from (3.36) that  $\xi = F_2^{1/2} \bar{x} = F_2^{1/2} Hx/\delta$  is a suitable choice of boundary layer coordinate for this particular case. Then, in the limit  $F_2^{-1/2} \rightarrow 0$  with  $\xi$  fixed, (3.36) gives an appropriate inner problem for  $q_2^B$  instead of (3.44):

$$q_{2y}^B = \frac{(1 + \gamma)H}{\alpha \pi \cos \pi y} q_{2\xi}^B. \quad (3.45)$$

Interestingly, this is a heat equation with  $y$  a time-like variable and with the thermal diffusivity being dependent on  $y$ . It turns out, therefore, that when vortex stretching is very strong, a  $q_2$ -layer of width  $O(F_2^{-1/2} \delta)$  is formed *inside* the flow boundary layer of width  $O(\delta)$ . This substantiates the earlier intuitive argument provided in Section 3.4.2, i.e., the structure of  $q_2$  resembles the western boundary current on the  $\delta$ -scale, but a sublayer is required to satisfy the western boundary condition (3.37). In fact, we may present the behavior of  $q_2$  on the  $\delta$ -scale. This intermediate case (denoted by the superscript  $M$ ) is governed by (3.44) which is equivalent to the following system of ordinary differential equations:

$$\frac{d\bar{x}}{ds} = \Psi_y^B, \quad (3.46)$$

$$\frac{dy}{ds} = -\Psi_x^B, \quad (3.47)$$

$$\frac{dq_2^M}{ds} = \frac{H}{\alpha} \Psi_{\bar{x}\bar{x}}^B, \quad (3.48)$$

where  $s$  is a parameter and  $\Psi^B$  is given explicitly by (3.43). They are formally solved by

$$e^{\frac{x}{\alpha}} = 1 + x_0 e^{-(\pi^2 \sin \pi y)s}, \quad (3.49)$$

$$\frac{1}{2\pi} \log \frac{1 + \sin \pi y}{1 - \sin \pi y} = -\pi e^{-\frac{x}{\alpha}} s + y_0, \quad (3.50)$$

$$q_2^M = -\frac{H}{\alpha} e^{-\frac{x}{\alpha}} \pi \cos \pi y \cdot s + q_0, \quad (3.51)$$

where  $(x_0, y_0, q_0)$  are integration constants. We find that  $q_2^M$  reveals the exponential behavior similar to  $\Psi^B$  as expected. This is the reason why  $q_2^M$  also is strongly controlled by the flow boundary layer when vortex stretching is extremely strong.

Taking into account the above two extreme cases and also the numerical solutions presented in Figs. 3.3 and 3.4, we can expect that there is an intermediate value of  $F_2$ , say  $F_m$ , such that for  $F_2 < F_m$  the  $q_2$ -layer is wider than the  $\Psi$ -layer. When this is the case, the matching of the uniform distribution of  $q_2^M$  with the boundary values may not be contaminated by the boundary current which is narrower than the  $q_2$ -layer. Actually, as seen in Figs. 3.3 and 3.7,  $q_2^M$  has a minimum near the western boundary for  $F_2$  smaller than 0.5, whereas it has a maximum for  $F_2$  larger than 0.5, implying the existence of a transition regime around  $F_m \approx 0.5$ . We note that the condition  $F_2 < F_m$  is consistent with the right inequality in (3.30).

Here, we return to the problem for  $\psi_2^B$  for general values of  $F_2$ . Differentiating (3.31) with respect to  $X$  and substituting the result into (3.32) yields

$$\psi_{2X}^B q_y^B - \psi_{2y}^B q_X^B = -\frac{\gamma}{\alpha} \psi_{2XXX}^B - \frac{1}{\alpha} (1 + \gamma H) \psi_{2XX}^B. \quad (3.52)$$

Hence, only the second term on the right-hand side of (3.52) contributes to the exponential decay of  $\psi_2^B$ . In general, the characteristic lines for (3.52) are not the latitude circles, so that (3.52) is not always reducible to a Stommel problem. We may estimate the slope of the characteristic lines near the western boundary, using (3.14) with  $\Psi_X^B = O(1)$ , as

$$\left| \frac{q_X^B}{q_y^B} \right| \sim O\left(\frac{F_2}{1 + F_2}\right). \quad (3.53)$$

For the values of  $F_2$  used in the present experiment, this slope is not small, so that the western boundary layer for  $\psi_2$  is no longer simply of Stommel type. That is, the boundary layer solution  $\psi_2^B$  not only has a property characterized by an elliptic equation

$$\psi_{2X}^B \sim -A(X, y) \psi_{2XX}^B, \quad (3.54)$$

but also has a property characterized by a parabolic equation

$$\psi_{2y}^B \sim B(X, y) \psi_{2XX}^B. \quad (3.55)$$

In the latter case, the boundary layer structure is quite different from that of a simple  $O(\delta)$ -layer, so that the functional relationship  $\psi_2^B = G(q')$  would take a different form from that obtained by IY. This gives a qualitative explanation for the discrepancy between IY's analytical solutions and our numerical solutions (Fig. 3.7).

### 3.6 Observation and realistic dynamical regime

#### 3.6.1 Levitus'94 maps

Observational studies have been conducted in connection with the development of the theoretical studies since the 1980s as cited in Section 3.1. The previous field maps in the world ocean reveal vast areas of uniform potential vorticity in the confined range of isopycnal surfaces. The updated maps for the North Pacific plotted using the latest data set also strongly point out the homogenization. Figures 3.12a-c show the annual mean distributions of potential temperature, salinity and potential vorticity on the isopycnal surface  $\sigma_\theta = 26.2$ , based on the newly compiled Levitus'94 climatology (NODC, 1994). These maps have been drawn on various isopycnal surfaces ranging from  $\sigma_\theta = 25.0$  to  $27.8$  every  $0.2\sigma_\theta$  by quadratically interpolating the vertical profile of  $\sigma_\theta$  (Yamagata, personal communication). Potential vorticity in those maps is defined using standard notation as  $(f/\rho_0)(\partial\sigma_\theta/\partial z)$  with  $\rho_0 = 1000 \text{ kg m}^{-3}$ .

Broad homogenized areas of these quantities up to near the western boundary are clearly seen in the subtropics, which is essentially the same as Talley (1988). We have already seen in Chapter 2 that the depth range of the homogenized isopycnals is small compared with the whole thermocline depth (see also Rhines, 1986). This suggests that an appropriate expression for the thermocline using a two-layer model is such that the lower layer is not very thick, even comparable to the upper layer as shown in Fig. 3.3. It is, therefore, encouraged greatly that the observed feature is likely to be explained even by the simple two-layer frictional model. It should be noted that the same effect as the interfacial friction may be produced by an explicit mass exchange between the layers, which is more likely mechanism particularly in the Pacific.

#### 3.6.2 Solution of planetary geostrophic equations

The planetary geostrophic equations that allow  $O(1)$  depth variations are known to be more suitable for discussing the large-scale ocean circulation than the quasigeostrophic equations (Charney and Flierl, 1981; Yamagata, 1982). In reality, Fig. 3.11d, showing the depth of the homogenized isopycnal surface, indicates the validity of the planetary geostrophic dynamics rather than the traditional quasigeostrophic dynamics.

Here, we conduct a similar numerical experiment but using the planetary geostrophic approximation to confirm the generality of the argument developed in the



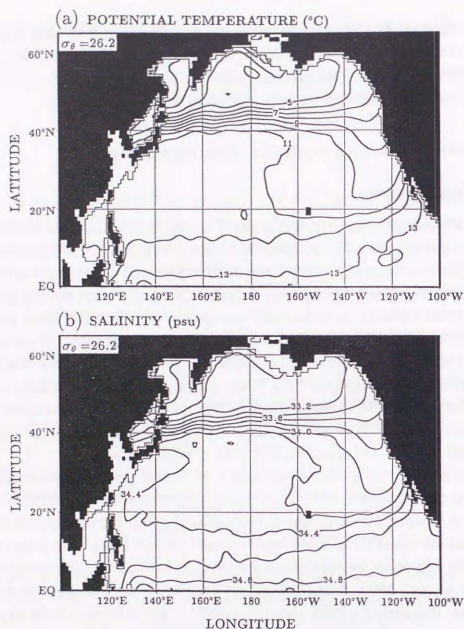


Figure 3.11. Annual mean climatological distribution of (a) potential temperature [ $^{\circ}\text{C}$ ], (b) salinity [psu], (c) potential vorticity [ $10^{-10}\text{m}^{-1}\text{s}^{-1}$ ], (d) depth [m] on the isopycnal surface  $\sigma_\theta = 26.2$  in the North Pacific. The hydrographic data used for the present maps come from World Ocean Atlas 1994 compiled by National Oceanographic Data Center.

previous sections. The two-layer planetary geostrophic equations can be written in dimensional form as

$$u_{1t} + f\mathbf{k} \times \mathbf{u}_1 = -\frac{1}{\rho_0}\nabla p + \frac{\tau}{\rho_0 h_1} - \frac{R}{h_1}(\mathbf{u}_1 - \mathbf{u}_2), \quad (3.56)$$

$$u_{2t} + f\mathbf{k} \times \mathbf{u}_2 = -\frac{1}{\rho_0}\nabla p + g'\nabla h_1 + \frac{R}{h_2}(\mathbf{u}_1 - \mathbf{u}_2) - \frac{K}{h_2}\mathbf{u}_2, \quad (3.57)$$

$$h_{1t} + (h_n \mathbf{u}_n) = 0, \quad (3.58)$$

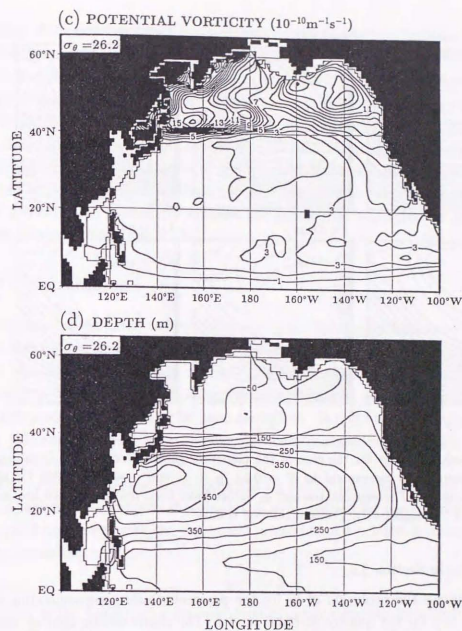
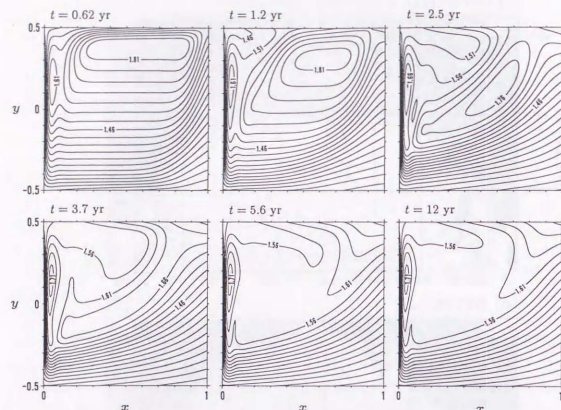


Figure 3.11. (Continued.)

where,  $(u_n, v_n)$  is the velocity of the  $n$ th layer,  $h_n$  is the  $n$ th-layer thickness,  $p$  is the depth-independent pressure,  $\tau = (\tau_0 \sin \pi y/L, 0)$  is the zonal wind stress introduced as a body force, and the notation of the other parameters is the same as the quasi-geostrophic equations in Section 3.2. The lower-layer potential vorticity is given by  $q_2 = f/h_2$ . As in Section 3.2, the linear acceleration terms are retained in the momentum equations just for the convenience of time integration. Eqs. (3.56)–(3.58) are integrated numerically on a staggered C-grid with the spacings of  $\Delta x = \Delta y = 19.53$  km. The numerical procedure is based on Holland and Lin (1975); in particular, the Poisson equation is solved using the same algorithm as used in solving the quasigeo-



**Figure 3.12.** Evolution of  $q_2$  for the case of the planetary geostrophic model. Parameter values are so chosen as to correspond to  $F = 0.33$ ,  $\alpha = 1$ , and  $\nu = \delta = 0.008$  for the quasigeostrophic model. The coordinates and  $q_2$  values have been scaled by 2500 km and  $1.825 \times 10^{-10} \text{ m}^{-1} \text{ s}^{-1}$ , respectively. Contour interval is 0.05.

strophic equations in Section 3.2.

Figure 3.12 shows the evolution of  $q_2$  for the parameter values corresponding to  $F = 0.33$  and  $\alpha = 1$  for the quasigeostrophic model. The characteristic spin-up time estimated using the speed of the linear baroclinic long Rossby wave is 5.28 yr. A distinguishable feature peculiar to the planetary geostrophic case is that the  $q_2$  contours can be closed by themselves so that their evolution appears to be more complicated than the simple advection (cf. Fig. 3.8). In fact, it seems that the constraint for homogenization is more restrictive than (3.30); the tongue of low potential vorticity (see the 1.56 contour) is indicative of the influence of the western boundary layer. These differences from the quasigeostrophic results are due to the nonlinearity associated with the interface displacements just mentioned. It is confirmed, however, that the homogenization is almost completed during the baroclinic spin-up time and that other essential features which are seen in the quasigeostrophic cases are also reproduced in the planetary geostrophic case. Therefore, the observed feature is likely to be explained even by the simple two-layer quasigeostrophic model in spite of the apparent inap-

ability of the quasigeostrophic approximation; the similarities between Figs. 1, 12 and 11 are so remarkable.

In the planetary geostrophic regime, the subpolar gyre is also of interest because it is not simply a mirror image of the subtropical gyre on the planetary scale. Since  $h_1$  itself may become very small by the Ekman suction in the subpolar gyre, the Rossby repeller, corresponding to the second term of (3.22) in the quasigeostrophic case, can be negligible. Thus, retardation by the wave is insufficient and the  $q_2$ -field is advected mainly by the Sverdrup flow; the profile of  $q_2$  is similar to that of  $\Psi$  in the steady state (not shown). The asymmetry between the subtropical and subpolar gyres is obvious in the observed map (Fig. 3.11c).

### 3.7 Conclusions

We have investigated the two-layer quasigeostrophic equations aimed for the large-scale subtropical ocean in which advection of relative vorticity is considered unimportant. An attempt is made to answer the question whether the lower-layer potential vorticity  $q_2$  is homogenized in this simplified system and, when it happens, what physical processes are responsible to homogenization. Despite the relatively simple situation, this issue has been controversial, particularly regarding of the frictional western boundary layer.

The present numerical experiment solving the initial-value problem has confirmed that a region of the uniform distribution of  $q_2$  is realized for the restricted cases. This is in good agreement with the theoretical prediction of a possible parameter regime for homogenization:

$$\frac{1}{\pi^2} < F_2 \leq \frac{2}{\pi}, \quad (3.59)$$

where  $F_2$  is the baroclinic rotational Froude number for the lower layer. The lower limit in (3.59), following IY, is appended to stand for the condition that a geostrophic contour is closed. The upper limit in (3.59) has been averaged for definiteness, arising from the condition that the zonal characteristic speed for the  $q_2$ -equation (3.19) is not positive so that information on  $q_2$  does not come from the western boundary layer. If the source and diffusion terms are negligible [cf. (3.29)],  $q_2$ -contours may then be advected southward to leave a gap north of them which is filled with the uniform potential vorticity.

The upper limit in (3.59) may be rewritten as

$$T_s < T_a, \quad (3.60)$$

where  $T_s$  and  $T_a$  are the baroclinic spin-up time and the advection time, respectively. It has also been shown experimentally that the pool region reaches a stationary state well



within  $T_1$ . This indicates, therefore, that the spin-up process must be accomplished before a particle makes a circuit of the pool through the western boundary layer; otherwise new extrema in  $q_2$  will be produced in the uniform region.

We have also examined the structure of the viscous western boundary layer for  $q_2$  to interpret the requirement (3.59). When  $F_2 \gg 1$ , the boundary layer for  $q_2$  is associated with the heat equation and has the width  $O(F_2^{-1/2}\delta)$ , where  $\delta$  is the bottom friction coefficient. This is narrower than the "flow" boundary layer of the Stommel type, having the width  $O(\delta)$ . This is the reason why the interior distribution of  $q_2$  is controlled by the western boundary current when vortex stretching is extremely strong. When  $F_2$  takes such a moderate value that satisfies (3.59), however, the boundary layer for  $q_2$  becomes wider than the flow boundary layer, so that the  $q_2$ -layer may match the homogenized value in the interior to the boundary values at the western boundary even in the presence of the western boundary current.

### References

- Bryan, K. 1987. Potential vorticity in models of the ocean circulation. *Q. J. R. Meteorol. Soc.* **113**, 713–734.
- Cox, M. D. and K. Bryan. 1984. A numerical model of the ventilated thermocline. *J. Phys. Oceanogr.* **14**, 674–687.
- Cox, M. D. 1985. An eddy resolving numerical model of the ventilated thermocline. *J. Phys. Oceanogr.* **15**, 1312–1224.
- Dewar, W. K. 1989. A nonlinear, time-dependent thermocline theory. *J. Mar. Res.* **47**, 1–31.
- Dewar, W. K., P. B. Rhines, and W. R. Holland. 1984. The nonlinear spin-up of a stratified ocean. *Geophys. Astrophys. Fluid Dyn.* **30**, 169–197.
- Holland, W. R., T. Keffer, and P. B. Rhines. 1984. Dynamics of the oceanic general circulation: the potential vorticity field. *Nature* **308**, 698–705.
- Huang, R. X. 1987. A three-layer model for wind-driven circulation in a subtropical-subpolar basin. Part I: Model formulation and the subcritical state. *J. Phys. Oceanogr.* **17**, 664–678.
- Huang, R. X. 1988. A three-layer model for wind-driven circulation in a subtropical-subpolar basin. Part III: Potential vorticity analysis. *J. Phys. Oceanogr.* **18**, 739–752.
- Ierley, G. R. and W. R. Young. 1983. Can the western boundary layer affect the potential vorticity distribution in the Sverdrup interior of a wind gyre? *J. Phys. Oceanogr.* **13**, 1753–1763.
- Jarvis, R. A. and G. Veronis. 1994. Strong deep recirculations in a two-layer wind-driven ocean. *J. Phys. Oceanogr.* **24**, 759–776.
- Keffer, T. 1985. The ventilation of the world's oceans: maps of the potential vorticity field. *J. Phys. Oceanogr.* **15**, 509–523.
- Lozier, M. S. and S. C. Riser. 1989. Potential vorticity dynamics of boundary currents in a quasi-geostrophic ocean. *J. Phys. Oceanogr.* **19**, 1373–1396.
- McDowell, S., P. B. Rhines, and T. Keffer. 1982. North Atlantic potential vorticity and its relation to the general circulation. *J. Phys. Oceanogr.* **12**, 1417–1436.
- Musgrave, D. L. 1985. A numerical study of the roles of subgyre-scale mixing and the western boundary current on homogenization of a passive tracer. *J. Geophys. Res.* **90**, 7037–7043.
- Musgrave, D. L. 1990. Numerical studies of tritium and helium-3 in the thermocline. *J. Phys. Oceanogr.* **20**, 344–373.
- National Oceanographic Data Center. 1994. *World Ocean Atlas 1994* (CD-ROM Data Set Documentation), Washington, D.C.
- Pedlosky, J. 1990. The dynamics of the oceanic subtropical gyres. *Science* **248**, 316–322.
- Pedlosky, J. 1996. *Ocean Circulation Theory*. Springer-Verlag, Berlin Heidelberg.
- Rhines, P. B. 1986. Vorticity dynamics of the oceanic general circulation. *Ann. Rev. Fluid Mech.* **18**, 433–497.
- Rhines, P. B. and R. Schopp. 1991. The wind-driven circulation: Quasi-geostrophic simulations and theory for nonsymmetric winds. *J. Phys. Oceanogr.* **21**, 1438–1469.
- Rhines, P. B. and W. R. Young. 1982. A theory of the wind-driven circulation I. Mid-ocean gyres. *J. Mar. Res.* **40** (Suppl.), 559–596.
- Rhines, P. B. and W. R. Young. 1983. How rapidly is a passive scalar mixed within closed streamlines? *J. Fluid Mech.* **133**, 133–145.
- Salmon, R. 1994. Generalized two-layer models of ocean circulation. *J. Mar. Res.* **52**, 865–908.
- Talley, L. D. 1988. Potential vorticity distribution in the North Pacific. *J. Phys. Oceanogr.* **18**, 89–106.

- Welander, P. 1966. A two-layer frictional model of wind-driven motion in a rectangular basin. *Tellus* **18**, 54–62.
- Welander, P. 1968. Wind-driven circulation in one- and two-layer oceans of variable depth. *Tellus* **20**, 1–16.
- Young, W. R. 1987. Baroclinic theories of the wind driven circulation, In: *General Circulation of the Ocean* (H. D. I. Abarbanel and W. R. Young, eds.), pp. 134–201 Springer-Verlag, New York.

## Chapter 4

### Gyres induced by curl-free winds in the tropics

#### 4.1 Introduction

Some curious features are often observed along and near the equator in the results of ocean general circulation models (OGCMs). For example, zonal stacked jets and small-scale meridional cells of remarkable amplitude are found by several researchers in their thermohaline circulations (cf. Weaver and Sarachik, 1990). They claim that those nontrivial phenomena are attributable to insufficient vertical resolution, i.e., to the numerical schemes for vertical density flux. Actually, those features can be removed with higher vertical resolutions. However, it is known that unexpected features similar to those mentioned above but (usually) of negligible magnitude may still appear in the equatorial regions due to diapycnal density mixing. Such physical processes should, of course, be distinguished from computational errors (cf. McCreary, 1981).

A much more striking example concerns steady, vertically integrated circulations. The standard linear inviscid theory for the wind-driven ocean circulation tells us that without wind stress curl a homogeneous ocean bounded by meridional solid walls ends up with no motion; the external wind forcing balances with the pressure gradient in the steady state (e.g., Rooth et al., 1978; Greatbatch and Yamagata, 1985). Despite this principle, a pair of cyclonic barotropic gyres straddling the equator is sometimes found in the OGCM results even when the zonal wind is uniform; their volume transport is of considerable amount. Figure 4.1 shows such examples (Semtner and Holland, 1980; Philander and Pacanowski, 1980; Liu et al., 1994). Each gyre extends zonally across the whole model basin (typically 4000 km) and is confined meridionally to  $5^\circ$  on each side of the equator. In addition, both gyres are cyclonic irrespective of the zonal wind direction (cf. Figs. 4.1a and b). Semtner and Holland (1980), who obtained a time-mean mass transport of more than 10 Sv, explained that the closed barotropic gyres are intrinsically nonlinear in character. Philander and Pacanowski (1980), whose volume transport is 5 to 6 Sv, suggested that the gyres are produced either in the nonlinear case or in the transient case. Both papers pointed out the importance of meridional circulations which may enhance eastward momentum flux just below the equatorial



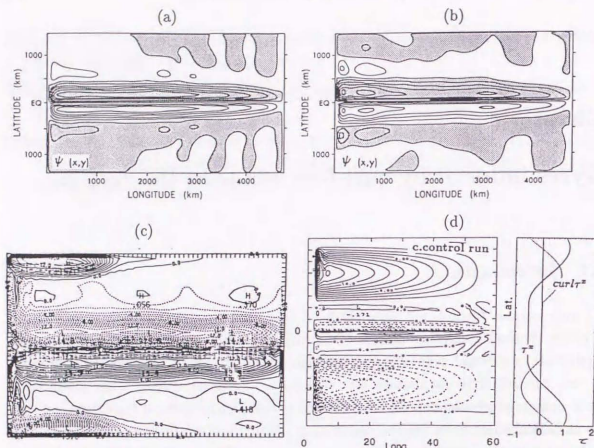


**Figure 4.1.** Time-mean barotropic streamfunction [Sv] when a uniform zonal wind is applied to the tropics. (a) Philander and Pacanowski (1980), easterly wind. (b) Philander and Pacanowski (1980), westerly wind. (c) Sautner and Holland (1980), easterly wind. (d) Liu et al. (1994), easterly wind.

surface jets (cf. Fofonoff and Montgomery, 1955).

Similar barotropic gyres are also obtained with simpler layer models. Cane (1979a) carefully designed such a 2.5-layer model that includes the mixed layer of uniform thickness. He was successful in reproducing the steady equatorial undercurrent and rotational barotropic circulations driven by uniform winds. From the subsequent numerical experiments using nonlinear equations, Cane (1979b) did obtain cyclonic gyres for a uniform easterly wind, although the vertically integrated transport is only implicit. On the other hand, Greatbatch and Yamagata (1985), using a shallow water model, suggested that a steady motion generated by a uniform westerly wind may be interpreted as a free inertial mode of the Fofonoff type.

The key mechanism suggested so far is associated with the inertial effects, which may avoid the no-motion principle mentioned above. We nonetheless try to seek for another possible explanation of the steady rotational flows without appealing to the nonlinearity. This is because we are greatly stimulated by McCreary (1981) and Yamagata and Philander (1985) who demonstrated the importance of diapycnal density mixing

in generating steady equatorial motions. The mixing process can prevent baroclinic long Rossby waves from propagating throughout the basin and establishing zonal pressure gradients which may balance with wind stresses. Furthermore, Philander and Pacanowski (1980) pointed out that those barotropic circulations resemble the Sverdrup flow in the sense that the gyres consist of western boundary currents and wakes due to the baroclinic long Rossby waves. These qualitative properties suggest that the gyres may be explained within the framework of the linear theory (e.g., Anderson and Gill, 1975). In this chapter, we focus on diapycnal density mixing to explain the above surprising features observed in the OGCMs.

## 4.2 Basic mechanism of rotational flows

Consider a 2.5-layer model on an equatorial  $\beta$ -plane  $(x, y)$  where  $x, y$  are the Cartesian coordinates in the eastward and northward directions, respectively. The  $i$ th ( $i = 1, 2$ ) layer contains fluid of variable thickness  $h_i$  and of uniform density  $\rho_i$ . The third layer has density  $\rho_3$  ( $> \rho_2 > \rho_1$ ) and infinite depth, so that it is assumed to be at rest. The time-dependent governing equations under the rigid-lid, Boussinesq and hydrostatic approximations are written in dimensional form as

$$\mathbf{v}_{1t} + f\mathbf{k} \times \mathbf{v}_1 = -g'_1 \nabla h_1 - g'_2 \nabla (h_1 + h_2) - \epsilon \mathbf{v}_1 + \frac{\boldsymbol{\tau}}{\rho_0 h_1}, \quad (4.1)$$

$$h_{1t} + \nabla \cdot (\mathbf{v}_1 h_1) = -\gamma_1 (h_1 - H_1), \quad (4.2)$$

$$\mathbf{v}_{2t} + f\mathbf{k} \times \mathbf{v}_2 = -g'_2 \nabla (h_1 + h_2) - \epsilon \mathbf{v}_2, \quad (4.3)$$

$$h_{2t} + \nabla \cdot (\mathbf{v}_2 h_2) = -\gamma_2 (h_2 - H_2), \quad (4.4)$$

where the Coriolis parameter is represented as  $f = \beta y$  with  $\beta$  constant and  $g'_1 = g(\rho_2 - \rho_1)/\rho_0$  and  $g'_2 = g(\rho_3 - \rho_2)/\rho_0$  are the reduced gravities with the acceleration due to gravity  $g$  and a constant reference density  $\rho_0$ ,  $\nabla$  denotes the horizontal gradient operator,  $\mathbf{k}$  is the upward vertical unit vector, and  $\boldsymbol{\tau} = (\tau^x, 0)$  is the zonal wind stress introduced as a body force. The nonlinear advection terms have been omitted in the momentum equations, (4.1) and (4.3), for the reason mentioned previously, whereas the continuity equations, (4.2) and (4.4), include the fully nonlinear effect. Rayleigh friction with a coefficient  $\epsilon$  is used as a momentum dissipation mechanism, and its value is assumed to be the same for both moving layers. Diapycnal density mixing is represented in the continuity equations in the simplest form of Newtonian cooling whose coefficients,  $\gamma_1$  and  $\gamma_2$ , may have different values. The mixing stops in each layer when the  $i$ th layer becomes equal to the constant mean depth  $H_i$ . The magnitude of  $\epsilon$  should be larger than that of  $\gamma_i$  if the momentum exchange associated with the density mixing decelerates the motion of the surface layer (see Gent, 1993). However, we do not stick to this constraint as usual in the later numerical calculations.

We provide a possible driving mechanism of steady barotropic circulations by considering the vorticity balance. Since diapycnal density mixing causes divergent flows in connection with strong Ekman divergence/convergence along the equator, we can relate the density mixing to vortex stretching which is required to induce barotropic flows. The following argument may be compared with Fofonoff and Montgomery (1955) who discussed relative vorticity of *nondivergent* meridional flows.

We decompose the velocity vector of each layer into the rotational (nondivergent) part  $\mathbf{v}_i^R$  and the divergent part  $\mathbf{v}_i^D$  ( $i = 1, 2$ ) such that

$$\mathbf{v}_i = \mathbf{v}_i^R + \mathbf{v}_i^D. \quad (4.5)$$

Then, we introduce the streamfunction  $\psi_i$  and the velocity potential  $\phi_i$  as follows:

$$\mathbf{v}_i^R h_i = \mathbf{k} \times \nabla \psi_i, \quad (4.6)$$

$$\mathbf{v}_i^D h_i = \nabla \phi_i. \quad (4.7)$$

From (4.2) and (4.4), the velocity potential satisfies

$$\nabla^2 \phi_i = -h_{ii} - \gamma_i(h_i - H_i). \quad (4.8)$$

In particular, in a steady state, we have

$$\nabla^2 \phi_i = -\gamma_i(h_i - H_i). \quad (4.9)$$

From (4.1) and (4.3) and using (4.6)–(4.9), we obtain the steady-state vorticity equations:

$$J(\psi_1, f) = -\nabla \cdot (f \nabla \phi_1) - g_2' J(h_1, h_2) - \epsilon \nabla^2 \psi_1 + \frac{1}{\rho_1} \text{curl } \tau, \quad (4.10)$$

$$J(\psi_2, f) = -\nabla \cdot (f \nabla \phi_2) + g_2' J(h_1, h_2) - \epsilon \nabla^2 \psi_2, \quad (4.11)$$

where  $J$  denotes the Jacobian operator,  $\text{curl } \tau$  denotes the vertical component of  $\nabla \times \tau$ . On summing up both vorticity equations to eliminate the interaction terms, we have the barotropic vorticity equation:

$$J(\Psi, f) + \epsilon \nabla^2 \Psi - \frac{1}{\rho_0} \text{curl } \tau = -\nabla \cdot (f \nabla \Phi), \quad (4.12)$$

where  $\Psi = \psi_1 + \psi_2$  and  $\Phi = \phi_1 + \phi_2$ .

The three terms on the left-hand side of (4.12) constitute the familiar Stommel problem. In addition, vorticity may be created by the potential flows whose contributions are represented by the terms of the form  $-\nabla \cdot (f \nabla \phi_i)$  on the right-hand side of (4.10)–(4.12). These terms are interpreted as the planetary divergence due to the potential flows, which induce the planetary advection  $J(\psi_i, f)$ . Thus, the net rotational transport may occur by the diapycnal density mixing even when the wind has no curl. It is expected that this mechanism strongly depends on the mixing coefficients  $\gamma_i$ . The sensitivity of the vertical flow structure to these coefficients will be confirmed by the numerical experiment.

### 4.3 Numerical results

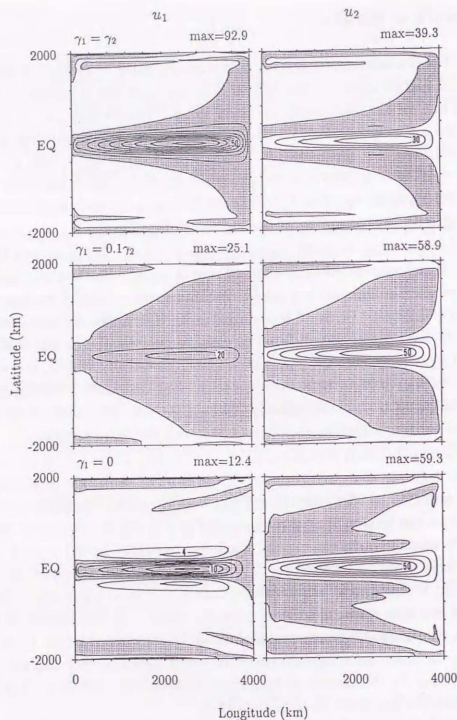
We present here some numerical results for a square basin of width  $L = 4000$  km. The upper and middle layers are initially at rest and have the thickness of 100 m. The damping and mixing coefficients are taken to be  $\epsilon^{-1} = 40$  days,  $\gamma_2^{-1} = 10$  days, while three values of  $\gamma_1$  are chosen ( $\gamma_1 = \gamma_2, 0.1\gamma_2$  and 0) to demonstrate typical cases. The other parameters are chosen as  $\rho_0 = 1000 \text{ kg m}^{-3}$ ,  $g_1' = g_2' = 0.02 \text{ ms}^{-2}$  and  $\beta = 2.3 \times 10^{-11} \text{ m}^{-1} \text{ s}^{-1}$ . A uniform easterly wind is assumed whose magnitude is  $0.05 \text{ Nm}^{-2}$ ; for a westerly wind, the direction of the resulting gyres are just reversed without any other qualitative change and hence are not shown here.

Numerical computation is carried out on a staggered C-grid. The system (4.1)–(4.4) is solved as an initial value problem by leapfrog time stepping with the Euler backward scheme until an equilibrium state is reached. We impose the boundary condition that there is no normal flow on the solid boundaries. Although a steady state is reached after around 100 days of integration for most cases, we present the results of day 400 to day 1200 in accordance with the values of  $\gamma_1$ . Using the steady  $h_i$ -field, the velocity potential  $\phi_i$  is calculated from the Poisson equation (4.9). Using the resulting  $\phi_i$ -field, then, the streamfunction  $\psi_i$  is immediately obtained by the direct integration of the linear potential vorticity equation, (4.10) or (4.11), with the SOR method.

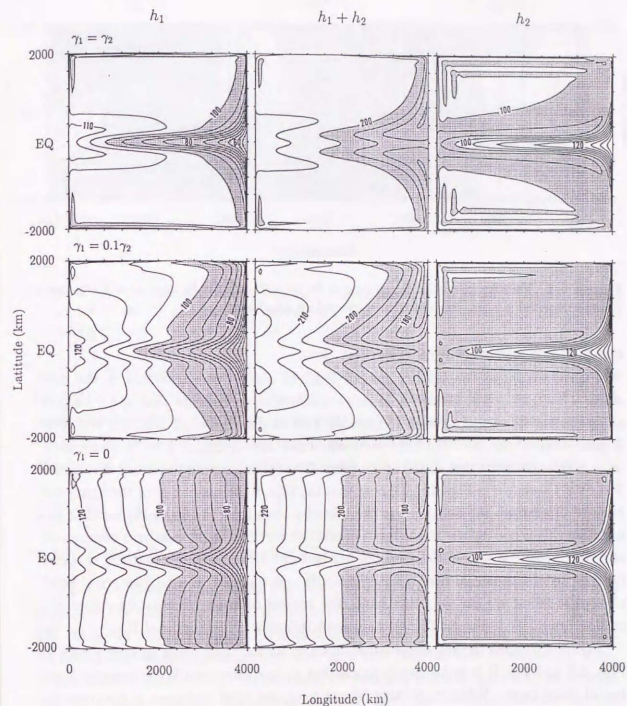
Figure 4.2 shows the zonal velocity  $u_i$  for  $\gamma_1 = \gamma_2$  (upper row),  $\gamma_1 = 0.1\gamma_2$  (middle row) and  $\gamma_1 = 0$  (lower row), respectively. These velocity fields are essentially the same as those obtained by McCreary (1981) and Yamagata and Philander (1985). A steady Yoshida jet can be seen in all three cases in Fig. 4.2, but its magnitude strongly depends on the mixing coefficient  $\gamma_1$ ; the maximum westward speed is  $92.9 \text{ cm s}^{-1}$  for  $\gamma_1^{-1} = 10$  days while  $25.1 \text{ cm s}^{-1}$  for  $\gamma_1^{-1} = 100$  days. The horizontal structure of the surface jet is also greatly sensitive to  $\gamma_1$ . For  $\gamma_1 = 0$ , in particular, eastward countercurrents are seen whose maximum speed is  $5 \text{ cm s}^{-1}$ . In the middle layer, on the other hand, an eastward-flowing equatorial undercurrent is reproduced. Even when  $\gamma_1$  decreases by an order, its maximum eastward speed increases only by 50% (from  $40 \text{ cm s}^{-1}$  to  $60 \text{ cm s}^{-1}$ ); the increase in  $u_2$  is much smaller than that in  $u_1$ . Thus, the model undercurrent is less sensitive to  $\gamma_1$  than to  $\gamma_2$ .

Figure 4.3 shows the distribution of  $h_1$  (left column),  $h_1 + h_2$  (middle column) and  $h_2$  (right column), respectively. We find from the maps of the upper-layer thickness  $h_1$  that large meridional gradients, which are associated with the surface jet, are concentrated about the equator, whereas for  $\gamma_1 = 0$  zonal pressure gradients are established over the whole off-equatorial domain. This simply confirms that the larger  $\gamma_1$  is, the more effectively the baroclinic long Rossby waves are damped. Similar properties are seen in the  $h_1 + h_2$  maps which show the total thickness of the moving layers; the meridional gradients are now linked to the undercurrent. However, the middle-layer thickness  $h_2$





**Figure 4.2.** Zonal velocity of the upper layer,  $u_1$ , (left column) and of the lower layer,  $u_2$ , (right column) in the steady state for the easterly wind ( $\tau^x = -0.05 \text{ Nm}^{-2}$ ). The Newtonian cooling coefficient for the lower layer is  $\gamma_2^{-1} = 10$  days for all three cases, while the cooling coefficient for the upper layer is  $\gamma_1 = \gamma_2$  (upper row),  $\gamma_1 = 0.1\gamma_2$  (middle row) and  $\gamma_1 = 0$  (lower row), respectively. Contour interval is  $10 \text{ cm s}^{-1}$  except for the lower left panel for which it is  $2 \text{ cm s}^{-1}$ . Regions of negative values are shaded.



**Figure 4.3.** Changes in the upper-layer thickness  $h_1$  (left column), in the total depth  $h_1 + h_2$  (middle column) and in the lower-layer thickness  $h_2$  (right column) in meters corresponding to Fig. 4.2. The left column corresponds to the displacement of the upper interface and the middle column corresponds to the displacement of the lower interface. Contour interval is 5 m. Shaded areas indicate that the layer thickness is less than the initial value.

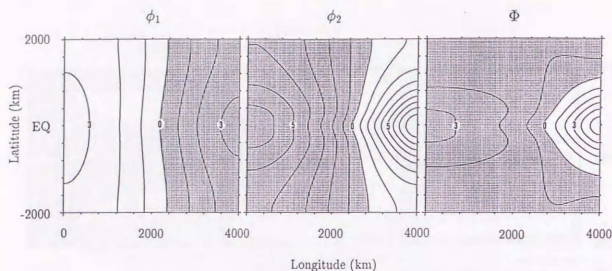


Figure 4.4. Velocity potential  $\phi_1$ ,  $\phi_2$  and  $\Phi$  in Sv ( $10^6 \text{ m}^3 \text{ s}^{-1}$ ) for the  $\gamma_1 = 0.1\gamma_2$  case. Contour interval is 1 Sv. Regions of negative values are shaded.

appears to be insensitive to  $\gamma_1$  in contrast to  $h_1$ .

Figure 4.4 shows the velocity potential  $\phi_1$ ,  $\phi_2$  and  $\Phi$ , corresponding to the case when  $\gamma_1 = 0.1\gamma_2$ . The overall qualitative features of  $\phi_1$  indicate that the divergent zonal current flows simply from the upwind side to the downwind side; the situation is just reversed for  $\phi_2$ . For this particular case, the divergent flow in the middle layer is stronger than that in the upper layer. The corresponding planetary divergence  $\nabla \cdot (f \nabla \phi_i)$  is shown in Fig. 4.5. We note that the sign of the quantities in the figure has been reversed from the definition in the vorticity equations, (4.10)–(4.12), so that the negative values correspond to the input of positive vorticity in the northern hemisphere and the opposite is true in the southern hemisphere. We can observe that the vorticity induced by the potential flow is antisymmetric and confined to a narrow zonal band about the equator. On the other hand, the regions of large vorticity seen near the eastern boundary in the middle layer are again indicative of the damped Rossby waves.

Figure 4.6 shows the transport streamfunction for the three cases corresponding to Figs. 4.2 and 4.3. It is immediately found that  $\psi_1$  is cyclonic while  $\psi_2$  is anticyclonic for all three cases. When  $\gamma_1$  is large (upper row), the total transport is governed by  $\psi_1$ , and hence  $\Psi$  shows a pair of anticyclonic gyres. [The distribution of the planetary divergence  $\nabla(f \nabla \Phi)$  in this case is similar to that in the right panel of Fig. 4.4 except for the sign.] As  $\gamma_1$  decreases,  $\psi_2$  becomes larger than  $\psi_1$  so that the barotropic gyres become cyclonic. When  $\gamma_1 = 0$ ,  $\psi_1$  is negligible so that a major part of the contributions to  $\Psi$  comes from  $\psi_2$ . Here, we compare the values of  $u_1^p$  and  $u_1^R$  at the equator calculated using the corresponding scalar fields  $\phi_i$  and  $\psi_i$ . For  $\gamma_1 = 0.1\gamma_2$  (cf. middle row of Fig. 4.2), the maximum zonal speeds are  $(u_1, u_2) = (-25.1, 59.3)$

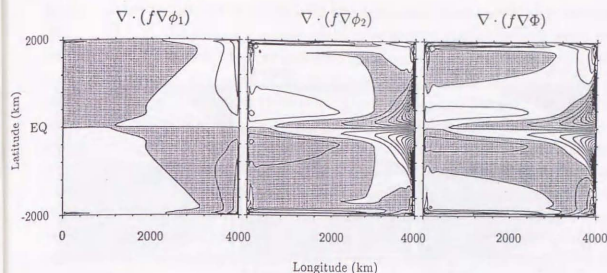


Figure 4.5. Planetary divergence in  $\text{ms}^{-2}$  corresponding to Fig. 4.4. Contour interval is  $5 \times 10^{-11} \text{ ms}^{-2}$ . Shaded areas indicate the input of positive vorticity in the northern hemisphere.

$\text{cm s}^{-1}$  at  $x = 2680 \text{ km}$ . At the same point,  $(u_1^p, u_2^p) = (-3.0, 4.9) \text{ cm s}^{-1}$ , while  $(u_1^R, u_2^R) = (-22.1, 54.4) \text{ cm s}^{-1}$ . Therefore, the small divergent flows induce the much larger rotational flows, which is reminiscent of the subtropical gyre (cf. Sverdrup, 1947). We note that the western intensification appears to be weak because of the special zonal distribution of the planetary divergence at each latitude (cf. Goldsbrogh, 1933).

## 4.4 Discussion

### 4.4.1 Comparison with the OGCM results

The net eastward transport for the case  $\gamma_1 = 0.1\gamma_2$  is 12 Sv (see Fig. 4.6). This is in good agreement with the OGCM results as mentioned in the first section (see Fig. 4.1). The transport would increase if the nonlinear advection was taken into account and/or if the Rayleigh damping coefficient  $\epsilon$  decreased (cf. Fofonoff and Montgomery, 1955; Semtner and Holland, 1980). Furthermore, the barotropic double gyre may be trapped near the equator, because the currents in both layers may be canceled over the off-equatorial regions when vertically integrated. Thus, we may conclude that diapycnal density mixing is a possible mechanism for the generation of a pair of trapped barotropic gyres which appear in the OGCM results (Fig. 4.1).

As mentioned before, Philander and Pacanowski (1980) obtained cyclonic gyres regardless of the direction of zonal winds (Figs 4.1a and b). Generally, in our model ocean, cyclonic barotropic gyres may be realized even for the easterly wind if  $\gamma_2 \gg \gamma_1$  (cf. Fig. 4.6). The latter condition is consistent with another OGCM result that large



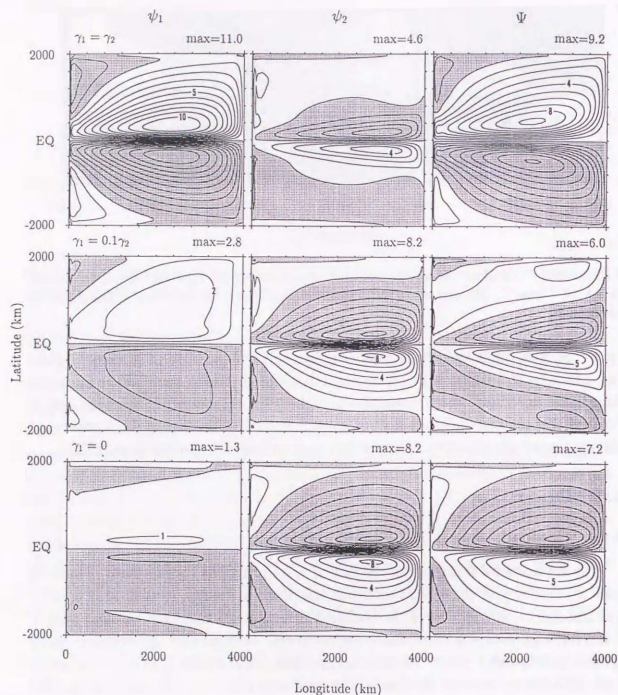


Figure 4.6. Transport streamfunction  $\psi_1$  (left column),  $\psi_2$  (middle column) and  $\Psi$  (right column) in Sv ( $10^6 \text{ m}^3 \text{ s}^{-1}$ ) corresponding to Fig. 4.2. Contour interval is 1 Sv. Regions of negative values are shaded.

density mixing occurs at the depths of the undercurrent (Pacanowski and Philander, 1981). Although the present 2.5-layer model does predict similar cyclonic gyres for a westerly wind when  $\gamma_1$  is large, we give another interpretation here in conformity with the OGCM results: For westerly winds, the equatorial downwelling compresses the isotherms, leading to a sharper thermocline about the equator [see Fig. 9 of Philander and Pacanowski (1980)]. For such a situation, a 1.5-layer model may be a better approximation for the upper equatorial ocean than the 2.5-layer model, and hence cyclonic gyres are easily predicted because the equatorial surface jet, which remains in a stationary state due to diapycnal density mixing, simply follows the wind direction. Therefore, we propose that the barotropic cyclonic circulations in the tropics are closely related to the rotation of the solid earth. The combined effect of the earth's rotation and zonal winds establishes a suitable vertical density structure in the tropics such that the total planetary divergence due to diapycnal density mixing always induces cyclonic vorticity which appears as the barotropic double gyres.

#### 4.4.2 Relation to the atmospheric phenomenon

The present mechanism that we have suggested is related to a well-known phenomenon in the tropical atmosphere. In the upper troposphere above the equatorial Pacific, a pair of anomalous anticyclones, which resembles the double gyres in Fig. 4.6, was found during the mature phase of the 1982–1983 El Niño (e.g., Arkin, 1982). This phenomenon has been explained successfully as stationary equatorial Kelvin and Rossby waves (the Matsuno-Gill pattern) in response to anomalous heating which is symmetric about the equator (Matsuno, 1966; Gill, 1980). In our model results, the upper layer suffers from heating in the regions where the thermocline is elevated. In other words, such regions provide mass source. The zonal alignment of the hypothetical mass source and sink (see Fig. 4.3), which are maintained by the wind in our model, is similar to the situation observed (Arkin, 1982) and assumed in the theoretical models (e.g., Matsuno, 1966). Thus, our steady-flow pattern can be regarded as an oceanic analogue of the forced stationary circulation pattern in the tropical atmosphere during the mature phase of ENSO events.

#### 4.5 Conclusions

Using a 2.5-layer model, we have provided a mechanism which can generate steady equatorial gyres without nonlinearity even if zonal winds have no curl.

Divergent flows directly driven by the zonal winds are maintained in the presence of diapycnal density mixing. These steady potential flows produce vortex stretching, which appears as an external forcing in a vorticity equation, so that rotational barotropic flows are induced in each layer. This process strongly depends on the

strength of the density mixing but always leads to rotational stacked gyres however small the mixing coefficients may be. Therefore, this may explain several nontrivial features sometimes observed in the thermohaline circulations computed by the OGCMs (Weaver and Sarachik, 1990).

The above mechanism can be applied to possible barotropic circulations in the tropics. For easterly winds, a 2.5-layer representation is a reasonable approximation for the equatorial ocean because of the equatorial upwelling. In this case, the vertically integrated transport may be cyclonic if the density mixing in the middle layer is sufficiently strong that the undercurrent overwhelms the surface jet. For westerly winds, on the other hand, the Ekman downwelling allows us to use a 1.5-layer model as a better simplification for the equatorial ocean, and hence the cyclonic gyres are naturally obtained. In this way, we expect a pair of cyclonic barotropic gyres straddling the equator regardless of the zonal wind direction. This surprising property is actually observed in the several OGCM results (Semtner and Holland, 1980; Philander and Pacanowski, 1980; Liu et al., 1994). We suggest, therefore, that diapycnal density mixing is one way to extract cyclonic vorticity from the rotating solid earth which establishes a suitable density stratification in accordance with the direction of zonal winds.

### References

- Anderson, D. L. T. and A. E. Gill. 1975. Spin up of a stratified ocean with applications to upwelling. *Deep-Sea Res.* **22**, 583-596.
- Arkin, P. A. 1982. The relationship between interannual variability in the 200 mb tropical wind field and the Southern Oscillation. *Mon. Wea. Rev.* **110**, 1393-1404.
- Cane, M. A. 1979a. The response of an equatorial ocean to simple wind stress patterns: I. Model formulation and analytic results. *J. Mar. Res.* **37**, 233-252.
- Cane, M. A. 1979b. The response of an equatorial ocean to simple wind stress patterns: II. Numerical results. *J. Mar. Res.* **37**, 253-299.
- Fofonoff, N. P. and R. B. Montgomery. 1955. The equatorial undercurrent in the light of the vorticity equation. *Tellus* **7**, 518-521.
- Gent, P. R. 1993. The energetically consistent shallow-water equations. *J. Atmos. Sci.* **50**, 1323-1325.
- Gill, A. E. 1980. Some simple solutions for heat-induced tropical circulation. *Q. J. R. Meteorol. Soc.* **106**, 447-462.
- Goldsbrough, G. R. 1933. Ocean currents produced by evaporation and precipitation. *Proc. Roy. Soc. London A* **141**, 512-517.
- Greatbatch, R. and T. Yamagata. 1985. Fofonoff-type, inertial-mode steady states in a model of the equatorial oceans. *J. Phys. Oceanogr.* **15**, 1349-1354.
- Liu, Z., S. G. H. Philander, and R. C. Pacanowski. 1994. A GCM study of tropical-subtropical upper-ocean water exchange. *J. Phys. Oceanogr.* **24**, 2606-2623.
- Matsuno, T. 1966. Quasi-geostrophic motions in the equatorial area. *J. Meteorol. Soc. Japan* **44**, 25-43.
- McCreary, J. P. 1981. A linear stratified ocean model of the equatorial undercurrent. *Phil. Trans. Roy. Soc. London A* **298**, 603-635.
- Pacanowski, R. C. and S. G. H. Philander. 1981. Parameterization of vertical mixing in numerical models of tropical oceans. *J. Phys. Oceanogr.* **11**, 1443-1451.
- Philander, S. G. H. and R. C. Pacanowski. 1980. The generation of equatorial currents. *J. Geophys. Res.* **85**, 1123-1136.
- Rooth, C., H. Stommel, and G. Veronis. 1978. On motion in steady layered geostrophic models. *J. Oceanogr. Soc. Japan* **34**, 265-267.
- Semtner, A. J. and W. R. Holland. 1980. Numerical simulation of equatorial ocean circulation. Part I: A basic case in turbulent equilibrium. *J. Phys. Oceanogr.* **10**, 667-693.
- Sverdrup, H. U. 1947. Wind-driven currents in baroclinic ocean: With applications to the equatorial currents of the eastern Pacific. *Proc. Nat. Acad. Sci.* **33**, 318-326.
- Weaver, A. J. and E. S. Sarachik. 1990. On the importance of vertical resolution in certain ocean general circulation models. *J. Phys. Oceanogr.* **20**, 600-609.
- Yamagata, T. and S. G. H. Philander. 1985. The role of damped equatorial waves in the oceanic response to winds. *J. Oceanogr. Soc. Japan* **41**, 345-357.